Thin-Film Flows Involving Deformable and Porous Interfaces

Haolin Yang

Submitted in fulfilment of the requirements for the
Degree of Doctor of Philosophy

School of Mathematics & Statistics
College of Science and Engineering
University of Glasgow

Sep 2025

Abstract

This thesis investigates thin-film flows involving deformable and porous interfaces, addressing both the fundamental fluid mechanics of free-surface flows prone to a novel class of instability and applications of related flows to biomedical transport.

The first part of this thesis focuses on viscous gravity currents spreading over lubricated substrates. Such a free-surface flow involves two immiscible viscous fluids, the interface between them being deformable, with the upper-most surface in contact with the atmosphere. A theoretical framework is developed for such flows using the principles of lubrication theory. We find similarity solutions and perform asymptotic analyses to characterise various flow regimes and a stress singularity near the intrusion front. Building upon this foundation, a linear stability analysis reveals that such flows are prone to a new class of viscous fingering instabilities, arising from hydrostatic interactions between the two viscous fluids. Despite fundamental differences in the type of flow, this new class of fluid-mechanical instabilities curiously resembles a number of features typical of its closest predecessor: the well-known Saffman-Taylor instability, or what simply became known as viscous fingering. This challenges the perception that viscous fingering is limited to porous media, or Hele-Shaw cells, as was popularised in the decades of research since Saffman and Taylor in the 1950s. This thesis highlights how free-surface flows of fluids of unequal viscosity can exhibit similar fingering to that seen in porous media, widening the definition of what the fluid mechanical community perceives to be viscous fingering. We explore how this new class of instabilities depends on contrasts in the viscosity, density, and source flux, and what determines wavelength selection. Extending the problem to inclined substrates demonstrates that the onset and mechanism of instability are robust and not tied to geometric configuration.

The second part of this thesis turns to biomedical transport in haemodialysis – a treatment option for patients affected by kidney failure. Such treatment, in itself, is a rich fluid-mechanical problem, involving the flow of two viscous fluids (blood and a sterile solution, known as dialysate) in an artificial kidney known as a dialyser. Dialysers involve thousands of long and thin hollow fibres that facilitate the removal of toxins and excess fluid from the blood. On the scale of a single fibre, the length scales involved are such that both blood and dialysate behave as thin films of viscous fluid, separated by a semipermeable fibre membrane. We use lubrication theory to develop a consistent mathematical framework modelling the fluid

flow and solute transport within a single fibre of a typical dialyser, characterising both diffusive and convective transport of toxins from the blood to the dialysate. By performing asymptotic analyses, we obtain analytical expressions for the clearance (characterising treatment efficiency) and recover classical results from the literature as special cases in various asymptotic limits. By incorporating fluid flow, our framework is faithful to the underlying hydrodynamics and provides a systematic foundation for improving dialyser design and exploring new treatment modalities.

Contents

List of Tables

List of Figures

Acknowledgements

I would like to express my deepest gratitude to my supervisor, Katarzyna Kowal, for her unwavering support, guidance, and encouragement over the past four years. Her wisdom, vision, and generosity have been invaluable to both my academic and personal development, and I am profoundly grateful for all that I have learned under her supervision.

I am also sincerely grateful to Nigel Mottram, who supervised me during the first two years of my PhD, for his kind support and guidance at the early stages of my research. His advice and encouragement laid the foundation for much of the work that followed.

My thanks also go to my parents, Jianbo Yang and Liping Wu, and to my grandmother, Xiuxiang Li, whose love, encouragement, and support have carried me through this journey. I would also like to remember my grandfathers, Peiyi Wu and Fengjun Yang, who sadly passed away this year. It is one of my greatest regrets that they cannot be here to witness the first "Dr. Yang" in our family.

Finally, I would like to thank my partner, Jingwei Fu, for her constant support. I am also grateful to the city of Glasgow, where we met, and which will always hold a special place in my heart.

Declaration

I hereby declare that, except where explicitly stated and properly referenced, the content of this dissertation is my own original work. It has not been submitted, either in whole or in part, for any other degree or qualification at this or any other university. This dissertation is solely the result of my own efforts, except where collaboration is acknowledged in the text or in the acknowledgements.

The content of Chapter 2 and 3 has been published in the *Journal of Fluid Mechanics* (Yang *et al.*, 2024; Yang & Kowal, 2025).

Chapter 1

Introduction

Thin film flows refer to the motion of fluid layers whose thickness is much smaller than their extent in the other spatial dimensions. When inertial effects are negligible (that is, when the Reynolds number, describing the relative importance of inertial effects to viscous effects, is small), the large disparity between the length scales inherent to thin film flows allows for a significant simplification of the full Navier–Stokes equations, describing the flow. Such an asymptotically consistent simplification leads to a reduced-order framework, which forms the basis of lubrication theory. First introduced by Reynolds (1886) in work on lubricated bearings, lubrication theory provides an asymptotic approximation for the dynamics of thin film flows, capturing the dominant physical effects with significantly reduced complexity.

This thesis investigates low-Reynolds-number thin-film flows involving deformable and porous interfaces. The thesis is split into two parts by theme. Part I (Chapters 2-4) of this thesis focuses on thin-film free-surface flows, in which the interfaces between the fluids involved are free and deformable. Chapter 2 examines a gravity-driven thin film of viscous fluid spreading over a rigid horizontal plate lubricated by another viscous fluid. Chapter 3 demonstrates that such flows are prone to a novel viscous fingering instability, with a linear stability analysis identifying conditions under which instability occurs, contrasting with its closest predecessor: the Saffman-Taylor instability. The analysis of Chapter 4, extending the problem to inclined substrates, demonstrates that the onset and mechanism of instability is not tied to geometric configuration alone.

Part II (Chapter 5) of this thesis addresses thin-film flows interacting with porous surfaces, motivated by biomedical applications. In particular, Chapter 5 develops a mathematical model of the fluid mechanics and solute transport in haemodialysis and haemodiafiltration – treatment options for patients with kidney failure. Blood is circulated through an artificial kidney, known as a dialyser, and purified by contact with a sterile solution, known as dialysate. A dialyser contains thousands of long, thin, hollow and semi-permeable fibres, through which toxins and excess water are removed from the blood. At the scale of a single fibre, both blood and dialysate behave as thin films of viscous fluid, separated by the fibre membrane. We use lubrication theory

to develop a mathematical framework describing the fluid dynamics and solute transport within a single fibre.

1.1 Thin films of viscous fluid spreading over lubricated substrates

Flows of thin films of viscous fluid spreading under the action of gravity are ubiquitous in the world around us, as seen in various industrial (Oron *et al.*, 1997), environmental (Simpson, 1982), and geophysical (Huppert, 2006) applications. These range from the spread of oil on the sea (Hoult, 1972) to the dynamics of lava flows (Griffiths, 2000), for example. Particularly striking is the range of possible behaviours when a thin film of viscous fluid spreads under gravity over a soft-bedded, or liquid-infused, substrate. Small-scale industrial applications of such lubricated flows include multi-layer thin-film coating processes, such as for electronics and medical devices (Ying *et al.*, 2015), and 3D printing or additive manufacturing applications (Mukherjee *et al.*, 2016; Sames *et al.*, 2016), for example. In the latter context, molten material (liquid) is continually added to soft, solidifying substrates that are partially solid and partially liquid, and hence, deformable (Khairallah *et al.*, 2016; Kowal *et al.*, 2018).

Other examples on the small scale include physiological applications such as that of nasal drug and vaccine delivery, in which an intranasally-delivered liquid drug solution or vaccine interacts with a viscous layer of mucus (Masiuk *et al.*, 2016). A poor understanding of drug-mucus interactions currently hinders the development of effective nasally-delivered vaccines, despite their potential to boost effectiveness by targeting respiratory viruses at the point of entry into the body (Madhavan *et al.*, 2022). A recent clinical trial prompted the need for research to help such vaccines remain in the nose and to reliably quantify the proportion of the drug or vaccine that is cleared away down the nasal passages towards the pharynx and gastrointestinal tract by mucocilliary clearance (Masiuk *et al.*, 2016; Madhavan *et al.*, 2022).

On much larger scales, flows of lubricated viscous fluids are relevant to a range of geophysical applications such as the flow of ice sheets (Schoof & Hewitt, 2013), which flow over a layer of unconsolidated, water-saturated subglacial sediment, or till. Till is known to act as a basal lubricant for the flow of the overlying ice. It has also been found to accelerate the flow of ice, noticeably flattening its upper surface (Kowal & Worster, 2015). Viscous coupling between ice and till has also been postulated as a possible cause of the formation of fast-flowing ice streams, as observed experimentally (Kumar *et al.*, 2021; Gyllenberg & Sayag, 2022). This complements other ice-stream formation mechanisms, including positive feedback between sliding and basal melt production (Fowler & Johnson, 1995; Sayag & Tziperman, 2008), a triple-valued sliding law (Sayag & Tziperman, 2009; Kyrke-Smith *et al.*, 2014) and thermoviscous fingering (Payne & Dongelmans, 1997; Hindmarsh, 2004, 2006). Subglacial till has also been found to accumulate in the grounding zones of ice sheets as observed seismically (Alley *et al.*, 1987; Batchelor

& Dowdeswell, 2015) and in fluid-mechanical experiments (Kowal & Worster, 2020).

Other geophysical applications of such two-layer flows include magma or lava flows in which a layer of molten material propagates over a solidifying solid-liquid substrate of higher viscosity (Griffiths, 2000), two-layer flows resulting from the interaction of dissimilar magmas (Snyder & Tait, 1995, 1998), ejecta flows of impact craters (Xiao & Komatsu, 2013), and flows in which molten material solidifies by cooling from above (Balmforth & Craster, 2000). Layered flows in porous media are another example (Woods & Mason, 2000), though notably, viscous coupling between the layers – of relevance to the present paper – is absent in the Darcy model of flow in a porous medium.

Theoretical and experimental investigations of viscous gravity currents to-date include single-layer (Smith, 1969; Huppert, 1982*a*,*b*) and two-layer (Kowal & Worster, 2015; Dauck *et al.*, 2019; Shah *et al.*, 2021) flows over horizontal and inclined substrates, intrusions at the interface between two dissimilar fluids (Lister & Kerr, 1989), flows over curved surfaces (Takagi & Huppert, 2010) and topological features (Hinton & Hogg, 2022), as well as thin-film flows of non-Newtonian viscous fluids (Hewitt & Balmforth, 2013; Hinton, 2022; Christy & Hinton, 2023), to name a few. Such flows are often modelled by applying the principles of lubrication theory, which is valid when the fluid layers are long and thin, and similarity solutions often exist in these situations. For example, the frontal position of a viscous gravity current spreading over a horizontal substrate, fed at constant source flux, propagates as $t^{4/5}$ and $t^{1/2}$ in two-dimensional and axisymmetric geometries, respectively (Huppert, 1982*b*). These scalings are also respected for two-layer viscous gravity currents (Kowal & Worster, 2015; Dauck *et al.*, 2019), including when modified by a power-law rheology (Leung & Kowal, 2022*a*). Frequently, such similarity solutions serve as global attractors, which other solutions approach at late times, despite the variety of possible initial conditions (Ball & Huppert, 2019). These similarity solutions have been proven to be stable to small perturbations for single-layer viscous gravity currents propagating over horizontal substrates and for gravity-driven flows in porous media (Mathunjwa & Hogg, 2006*a*,*b*), for example.

In Chapter 2, we examine the gravity-driven flow of a thin film of viscous fluid spreading over a rigid plate that is lubricated by another viscous fluid. We find, in Chapter 3, that flows over such a 'soft' substrate are prone to a viscous fingering instability. We examine the unperturbed base flow in Chapter 2 by applying the principles of lubrication theory, assuming that vertical shear provides the dominant resistance to the flow. We do so in axisymmetric and two-dimensional geometries in settings in which the flow is self-similar. A frontal stress singularity appears near the nose of the intruding layer, which we characterise using asymptotic techniques. Different flow regimes arise, depending on the values of four key dimensionless parameters, which we characterise across parameter space.

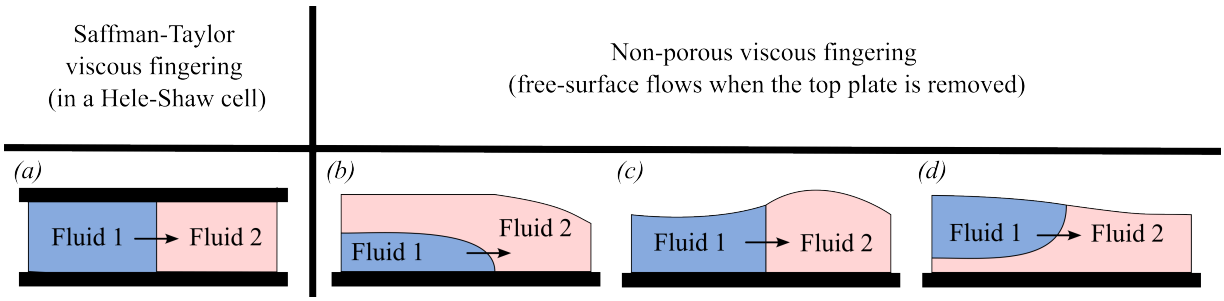

Figure 1.1: Vertical cross section of base flows susceptible to (*a*) classical viscous fingering instabilities (flows in a Hele-Shaw cell, or other porous medium) and (*b–d*) non-porous viscous fingering (free-surface flows). Fluid 1 is less viscous than Fluid 2.

1.2 Viscous fingering

Viscous fingering instabilities involve complex, finger-like patterning that emerges when a less viscous fluid invades a more viscous fluid in a porous medium or Hele-Shaw cell (Saffman & Taylor, 1958; Homsy, 1987). What has not been known until recently is that a similar type of viscous fingering instability also occurs in unconfined settings that do not involve porous media or Hele-Shaw cells. In particular, the interaction of the free-surface flows of two fluids of dissimilar viscosity manifests similar instabilities in various configurations depicted in Figure 1.1(*b–d*). A cross-sectional view of the viscous fingering of the last of these flows is depicted in Figure 1.2 in an idealised geometry, in which the fluids spread radially outwards. The configurations displayed in Figure 1.1(*b–d*) differ topologically from flows susceptible to classical viscous fingering instabilities, depicted in Figure 1.1(*a*), through the lack of an upper rigid boundary, which brings with it the need to depart from the use of Darcy's law for flow in porous media and the need to determine the upper free surface as part of the flow. Efforts to suppress this class of instabilities of free-surface flows whilst maintaining basal lubrication on the large scale led to the design of a structured substrate – a large-scale analogue of superhydrophobic substrates – which has been shown to give rise to a Navier-type slip macroscopically (Yan & Kowal, 2024).

The first examined configuration (Figure 1.1*b*) of flows susceptible to the novel instability involves the free-surface flow of a thin film of viscous fluid spreading beneath another viscous fluid, as seen in the experiments of Kowal & Worster (2015, 2019*a*,*b*) and Kumar *et al.* (2021). Such a flow becomes unstable to a novel cross-flow fingering instability when the intruding fluid is less viscous. Another configuration (Figure 1.1*c*), leading to similar instabilities, is one in which the intruding fluid fully displaces another viscous fluid (Kowal, 2021). The final configuration (Figure 1.1*d*) is one in which the intruding fluid spreads above a pre-existing thin film of viscous fluid, as seen in the experiments of Dauck (2020), which focused on the limit in which the two layers are of equal density. We examine flows in the final configuration in the thesis, completing the family of flows susceptible to the novel frontal instability.

Such free-surface flows are relevant to a range of phenomena involving the interaction of

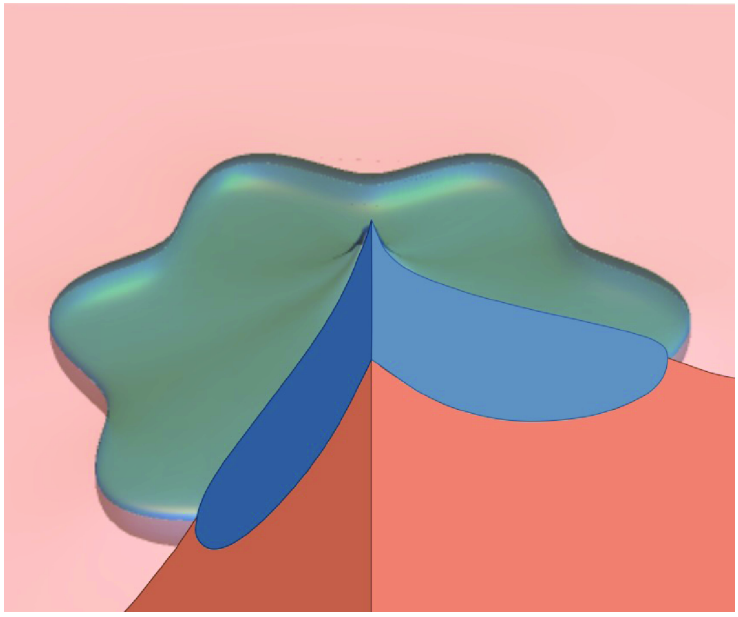

Figure 1.2: A schematic representation of a typical cross-sectional view of the viscous fingering of a thin film of fluid spreading over another, more viscous fluid in an idealised geometry in which the fluids spread radially outwards.

fluids of different viscosity. An example includes the nasal delivery of drugs and vaccines, which commonly results in what is referred to as *nasal dripping* in the medical community (Masiuk *et al.*, 2016). Nasal dripping, or fingering, observed in this context results from the interaction of a low-viscosity drug solution or vaccine with a more viscous mucus, as depicted in the schematic representation in the left-hand panel of Figure 1.3. Such fingering is more pronounced the higher the viscosity ratio between the mucus and drug solution or vaccine, as observed in experiments involving synthetic mucus and the drug Avicel, displayed in the middle and right-hand panels of Figure 1.3 (Masiuk *et al.*, 2016). Other examples include the interaction between liquid sulfide and silicate melt in a partially solidified (or mostly unsolidified) magmatic system or, more generally, the interaction of lava flows of different viscosity following cooling (Fink & Griffiths, 1990, 1998; Balmforth & Craster, 2000). Mention has also been made of a link to the flow of ice sheets over less viscous subglacial till, as explored theoretically and experimentally (Kumar *et al.*, 2021; Gyllenberg & Sayag, 2022).

The new class of instabilities of such free-surface flows have been termed *non-porous viscous fingering instabilities*, to reflect that they are not associated with porous media and that the mechanism of instability is similar to that of traditional viscous fingering instabilities, despite the lack of confinement (Kowal, 2021). Such instabilities can be thought of as an ultra-soft analogue of fingering in soft/deformable porous media. The latter type of instability is partially suppressed by the elastic deformation of the porous medium or Hele-Shaw cell (Pihler-Puzovic *et al.*, 2012, 2013). A simple representation of such a deformable porous medium involves a horizontal Hele-Shaw cell in which its upper wall is replaced by an elastic sheet that is free to

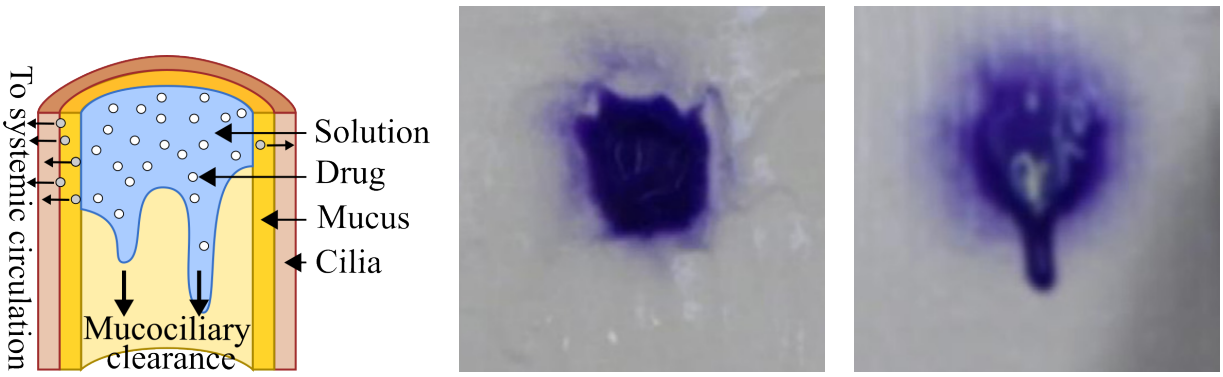

Figure 1.3: *Left-hand panel:* A schematic representation of a drug solution spreading over a layer of nasal mucus. *Middle and right-hand panels:* Photographs of experiments of a drug solution (3.5% Avicel formulation) flowing over a plate coated with (middle panel) low viscosity, healthy simulated mucus and (right-hand panel) high viscosity, diseased simulated mucus. A finger forms when the viscosity contrast between the drug solution and mucus is large. Photographs reproduced from Masiuk *et al.* (2016).

deform when a less viscous fluid is injected (Pihler-Puzovic *et al.*, 2012, 2013). Such instabilities are increasingly suppressed as the thickness of the sheet decreases. In this work, we remove the elastic sheet completely, falling into the realm of free-surface flows, rather than porous media flows. Alternatively, we remove the upper wall of a rigid horizontal Hele-Shaw cell depicted in Figure 1.1*a*. As a result, Darcy's law no longer applies.

Non-porous viscous fingering instabilities bring similarities to thermo-viscous fingering of free-surface flows, in which the viscosity contrast required for onset of instability is driven thermally (Hindmarsh, 2004, 2009; Algwauish & Naire, 2023). We also find it worthwhile to note the difference between non-porous viscous fingering instabilities and fingering of a driven spreading film (Huppert, 1982*a*; Troian *et al.*, 1989). Although both of these involve frontal instabilities of free-surface flows, the former requires a viscosity difference between two fluids and the latter does not, as it involves a single fluid only. The latter instability is, importantly, one in which surface tension is key. As such, non-porous viscous fingering is more closely comparable to viscous fingering in porous media, despite no presence of a porous medium itself.

Viscous fingering in porous media, including Hele-Shaw cells, received considerable attention throughout the last few decades following the seminal work of Saffman & Taylor (1958). This stemmed mainly from its broad range of applications, ranging from enhanced oil recovery (Orr & Taber, 1984) to coating applications (Taylor, 1963) and carbon sequestration (Cinar *et al.*, 2009). Similar instabilities are also frequently observed in nature, such as in crystal growth (Mullins & Sekerka, 1964), the spreading of bacterial colonies (Ben-Jacob, 1997), the dynamics of fractures (Hull, 1999), and the instability of flame fronts (Ben-Jacob *et al.*, 1992).

Interest has since emerged in the ability to either enhance or suppress these instabilities, and to manipulate the patterns that emerge, as desired, for industrial applications. Such control mechanisms have been found to depend upon a number of physical factors, including the injec-

tion rate of the less viscous fluid (Li *et al.*, 2009; Dias & Miranda, 2010), the miscibility of the two fluids involved (Perkins *et al.*, 1965) and their rheology (Kondic *et al.*, 1998; Fast *et al.*, 2001). Other effects that enhance or suppress these instabilities include changes in the viscosity ratio of the two fluids (Bischofberger *et al.*, 2014) and introducing particles (Luo *et al.*, 2018), for instance. Alterations in the geometry of the porous medium also influence the fingering patterns, when the alterations are both static (Nase *et al.*, 2011; Al-Housseiny *et al.*, 2012) and dynamic (Juel, 2012; Zheng *et al.*, 2015; Morrow *et al.*, 2019; Vaquero-Stainer *et al.*, 2019).

There are a number of similarities between traditional viscous fingering instabilities in porous media and the recently discovered non-porous viscous fingering instabilities. Stability analyses (in the configuration of Figure 1.1*b*) indicate that the latter instabilities emerge when the jump in *hydrostatic* pressure gradient across the intrusion front is negative (Kowal & Worster, 2019*a*,*b*; Kowal, 2021). This is similar to, yet contrasts with, traditional viscous fingering instabilities in porous media (Figure 1.1*a*), which are instead driven by a jump in *dynamic* pressure gradient (Homsy, 1987). Both types of instabilities occur when the intruding viscous fluid is less viscous than the layer into which it intrudes, as has been seen in experiments in which the injected fluid intrudes from below (Kowal & Worster, 2015, 2019*a*, Figure 1.1*b*) and from above (Dauck, 2020, Figure 1.1*d*). The latter experiments involved fluids of equal density. However, it has been found that non-zero density differences between the two layers of viscous fluid can suppress these instabilities when the injected fluid intrudes from below (Kowal & Worster, 2019*b*, Figure 1.1*b*). A similar observation has been found when the fluids are non-Newtonian (Leung & Kowal, 2022*b*, Figure 1.1*b*).

We demonstrate similar suppression when the intruding fluid spreads above a pre-existing thin film of viscous fluid, as depicted in Figure 1.1d. In particular, in Chapter 3, we examine the stability of a viscous gravity current intruding over a 'soft' lubricated substrate, the base flow of which is considered in Chapter 2. We do so by performing a linear stability analysis using the axisymmetric similarity solutions of Chapter 2 and characterise the parameter space over which these instabilities occur. We also compare this instability with other known fingering instabilities, including when the intruding layer is supplied from below, and contrast with Saffman-Taylor instabilities in a Hele-Shaw cell or other porous medium. We extend our stability analysis to analogous flows over an inclined substrate in Chapter 4. In particular, we demonstrate that such flows are similarly prone to the new class of viscous fingering instability, and, in fact, the additional component of gravity along an inclined plane promotes such instabilities further.

We note the additional relevance of non-porous viscous fingering down an inclined plane to breakouts of lava through levees around molten lava lakes (Orr *et al.*, 2023). In particular, when a molten lava lake solidifies, a levee forms around its edges, forming a more solid (or more viscous) barrier around the lava lake. It has been found that a breakout can form through the levee, resulting in subsequent 'single-finger' flow, especially along downwards sloping terrain.

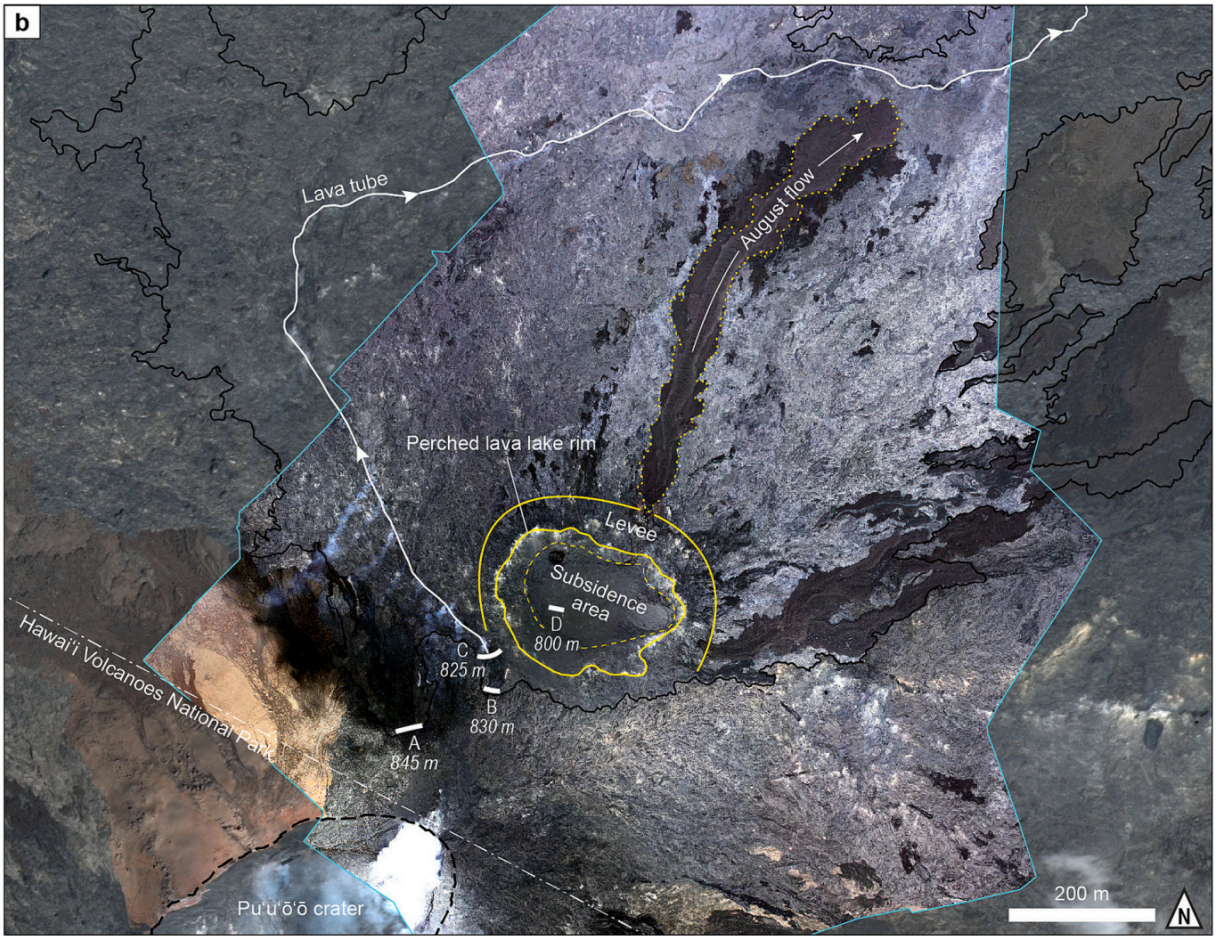

Figure 1.4: A single-finger *'a'ā flow* (dotted yellow line, also labelled as "August flow" in the figure) following an eruption from the levee of a crusted perched lava lake (solid yellow line) that had been inactive for a month at Kilauea. The single-finger flow advanced downslope over the following few days. Image reproduced from Orr *et al.* (2023).

An example is shown in Figure 1.4, reproduced from Orr *et al.* (2023). Although levees do not typically behave as a Newtonian viscous fluid on the small scale of tens of centimetres, upon homogenisation over sufficiently long length and time scales, the levee can be thought of as a layer of fluid of much higher effective viscosity than that of the molten lava. The flows considered in Chapter 4 are, in this sense, a relevant viscous analogue. We also note the relevance of such finger-like free-surface flows to the seepage of lava stored in rootless shields, creating localised uplift zones (Patrick & Orr, 2012).

1.3 Haemodialysis and Haemodiafiltration

We now turn to the fluid mechanics of haemodialysis (HD) and haemodiafiltration (HDF), forming Part II (Chapter 5) of this thesis. Such treatment involves filtration in two-layer thin-film flows consisting of blood and sterile solution, known as dialysate, in artificial kidneys, known as dialysers. Understanding the underlying fluid mechanics and solute transport provides the

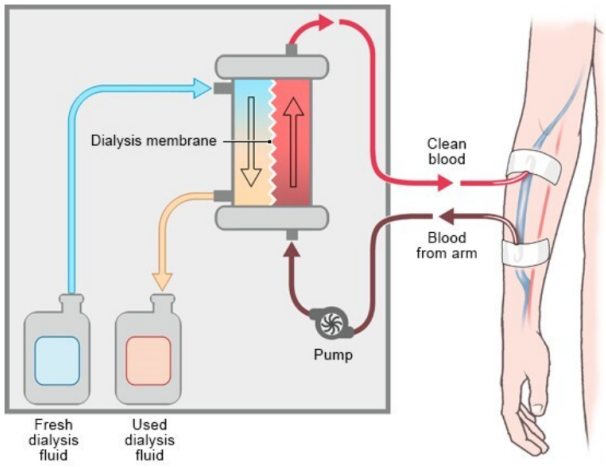

Figure 1.5: The schematic of a patient recieving haemodialysis. Image reproduced from National Center for Biotechnology Information (US) (2018).

framework necessary to tackle the main challenges preventing dialysis from being offered to the vast majority of those who need it.

Chronic kidney disease has emerged as one of the most significant causes of mortality in the 21st century, affecting over 10 percent of the global population, or approximately 850 million individuals (Jager *et al.*, 2019; Kovesdy, 2022). To put this into perspective, chronic kidney disease impacts more than twice as many people as diabetes and over 20 times as many people as HIV/AIDS (Jager *et al.*, 2019). While age-standardized mortality rates for most other chronic diseases such as cardiovascular disease and cancer have declined globally in recent decades, chronic kidney disease is now the third fastest-growing cause of death, projected to become the fifth leading cause of premature death by 2040 (Foreman & et al., 2018), rising from 13th place in 2016 (Naghavi & et al., 2017).

Current treatment options primarily include dialysis and kidney transplantation. While kidney transplantation is widely recognized as the preferred treatment for eligible patients with the end-stage renal disease (Tonelli & et al., 2010), several factors such as organ shortage (Matas *et al.*, 2023) limit its universal applicability, making dialysis the most common form of renal replacement therapy worldwide. For patients who are not transplant candidates or are awaiting a suitable donor, dialysis remains a vital and life-sustaining treatment (Chaudhry *et al.*, 2022). It is often considered a temporary bridge to kidney transplantation when a suitable organ becomes available. Nevertheless, dialysis is available to only less than 50% of those who need it owning to prohibitive costs and its reliance on large amounts of sterile water Francis *et al.* (2024). The latter is particularly inaccessible in developing countries.

Among dialysis therapies, HD is the most commonly used method, accounting for approximately 69% of all renal replacement therapies and 89% of all dialysis therapies (Bello *et al.*, 2022). Figure 1.5 shows a schematic of a patient receiving HD, in which the patient's blood is circulated outside the body through a device called a dialyser, often referred to as an artificial

Figure 1.6: Cross-sectional view of a dialyser, showing the bundle of hollow fibre membranes used for blood purification during HD. Image reproduced from B. Braun (n.d.).

kidney, where waste products and excess fluid are removed from the blood (Sargent & Gotch, 1996). The dialyser is a cylindrical filtration device containing thousands of hollow and porous fibres (Sakai, 2000), as depicted in Figure 1.6. The fibres are composed of a selective (or semi-permeable) membrane: it is designed to permit the passage of small solutes and water while retaining blood cells and large molecules such as albumin (Daugirdas *et al.*, 2012). Blood flows through the interior of these fibres while an aqueous solution, referred to as dialysate, designed to mimic extracellular fluid, is pumped in the opposite direction through the space between the fibres (Pittard, 2017). This counter-current flow, separated by semipermeable membrane walls of each fibre, allows for efficient removal of waste via diffusion, facilitating the movement of molecules along a concentration gradient between the blood and dialysate. This process is especially effective for small molecules (Lang *et al.*, 2023).

HDF is considered to be the most advanced dialysis therapy that is currently available, enhancing conventional HD by incorporating convective transport alongside diffusion (Kuhlmann, 2023). In HD, toxin removal primarily occurs through diffusion, which is effective for small molecules and less effective for large molecules. In contrast with HD, HDF combines diffusion with convection by introducing additional dialysate either directly before or directly after entry into the dialyser. These modes of HDF are referred to as pre- and post-dilution HDF, respectively. In convective transport, solutes are carried across the membrane pores from the blood into the dialysate along with the fluid flow. The extracted fluid volume is then replaced with a sterile substitution fluid, ensuring haemodynamic stability. Convection is less dependent on molecular size, meaning that, provided a solute can pass through the membrane, larger molecules can be removed as effectively as smaller ones (Lang *et al.*, 2023). This makes HDF particularly advantageous for clearing middle and large molecular weight toxins.

Although HD and HDF have evolved significantly, they continue to present numerous challenges today. Clinically, it is associated with a wide range of complications, including cardiovascular disease, diabetes, and vascular access-related infections, among others (Bello *et al.*, 2022).

Partly because of these complications, the mortality rate among patients undergoing dialysis remains relatively high, exceeding that of patients with several common cancers, such as prostate, breast, and colorectal cancer (Naylor *et al.*, 2019). Of all complications, cardiovascular disease is especially concerning, as it affects over two-thirds of patients and is responsible for nearly 50% of deaths in this population (Thompson & et al., 2015). This high burden is partly due to the haemodynamic stress caused by dialysis, which involves significant fluctuations in blood volume and pressure, placing acute strain on the cardiovascular system (Chirakarnjanakorn & et al., 2017). Economically, despite their clinical effectiveness, the widespread implementation of HD and HDF is financially unsustainable, even in high-income countries (Himmelfarb *et al.*, 2020). In 2010, approximately 2.6 million people worldwide received kidney replacement therapy, while an estimated equal number died due to lack of access (Liyanage *et al.*, 2015; Jager *et al.*, 2019). From a patient perspective, the burden of care remains substantial. HD and HDF often require frequent travel to dialysis centers, with treatments typically lasting four hours, at least three times per week. This routine contributes to a reduced quality of life and imposes significant limitations on employment and social participation. These ongoing challenges highlight the need for dialysis treatment options that are less complication-prone, more cost-effective, accessible, and patient-centered (Himmelfarb *et al.*, 2020).

Mathematical modelling of dialysis offers a way to tackle these challenges by improving dialyser design, enhancing treatment performance, reducing costs, and even enabling the development of new dialysis modalities. Despite its potential, this area has historically received limited attention and remains relatively underexplored. One of the earliest and most influential contributions to this field was made by Michaels (Michaels, 1966), who introduced a foundational model for evaluating dialyser performance when the fluid flux is assumed to be uniform, focusing solely on diffusive solute transport. Since then, various studies have increased our understanding of dialysis, including membrane transport in dialysers (Villarroel *et al.*, 1977), one-dimensional models (Jaffrin *et al.*, 1981; Akcahuseyin *et al.*, 1990; Waniewski *et al.*, 1994; Chang & Lee, 1988), two-dimensional models (Donato *et al.*, 2017; Osuga *et al.*, 1998), and more recently, three-dimensional models based on computational fluid dynamics (CFD) (Cancilla *et al.*, 2022; Ding *et al.*, 2015). As dialysis technology continues to evolve, mathematical modelling of dialysis should be viewed not only as a research topic but as a cornerstone of innovation in dialysis system design. Therefore, renewed attention and investment in this field are essential to drive meaningful progress in HD and HDF.

In Chapter 5, we develop a unified modelling framework faithful to the underlying hydrodynamics of HD and HDF, capturing both diffusive and convective solute transport. Using asymptotic techniques, we recover existing classical results found in the literature as special cases, thus giving credence to prior empirical assumptions being made. Our work serves as a foundation for testing further ideas for innovation in dialysis treatment, including the development of new flow modalities that optimise clearance given limited sterile water availability.

Part I

Thin-film flows over a lubricated substrate

Chapter 2

Dynamics of a thin film of fluid spreading over a lubricated substrate

The content of this chapter (and the relevant part of Chapter 1) has been published in

- Yang, H., Mottram, N. J. and Kowal, K. N. (2024) Dynamics of a thin film of fluid spreading over a lubricated substrate. *J. Fluid Mech.*, 1001: A47.

2.1 Introduction

We examine the flow of a viscous gravity current spreading under its own weight over a horizontal substrate that is prewetted by another thin film of viscous fluid of different density and viscosity, as depicted in Figure 2.1. A perhaps unexpected feature of the associated flows is that they may exhibit symmetry-breaking instabilities, similar to viscous fingering instabilities. In particular, we will demonstrate in Chapter 3 that viscous gravity currents intruding into another thin film of viscous fluid are susceptible to a novel frontal viscous fingering instability. The instability is similar to the Saffman-Taylor instability for viscous fluids intruding into one another in a Hele-Shaw cell or other porous medium, but this time without a Hele-Shaw cell or any porous medium present.

We assume that the flow of both layers is resisted dominantly by vertical viscous shear stresses, and that the effects of inertia and surface tension are negligible. In particular, we apply principles of lubrication theory to model the flow in terms of depth-integrated quantities and examine similarity solutions describing the flow.

We extend the work of Dauck *et al.* (2019), in which a version of this problem was examined theoretically and experimentally, focusing on the limit in which the two layers are of equal density. This problem is also relevant to the work of Lister & Kerr (1989) on the propagation of viscous gravity currents at the interface between two dissimilar fluids. Setting the properties of the uppermost fluid to match that of vapour recovers the present setup under some additional assumptions made by Lister & Kerr (1989), which we remove. These include setting up a quasi-

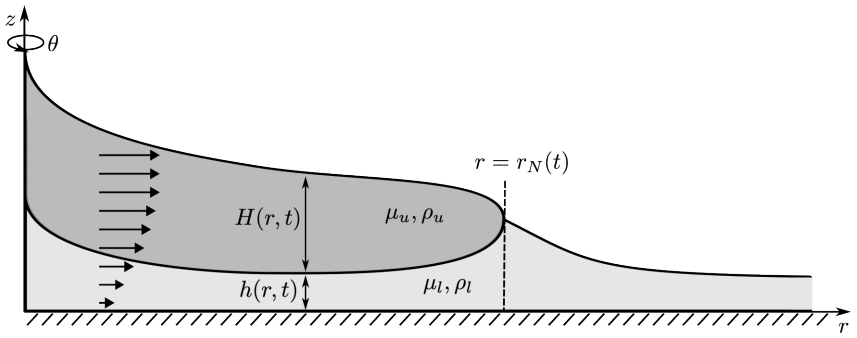

Figure 2.1: Schematic of a thin film of viscous fluid spreading under gravity over a rigid horizontal substrate pre-wetted by another viscous fluid in an axisymmetric geometry.

steady equilibrium in which there is no net flux of lower fluid through any cross-section of the flow and assuming that the intruding fluid is of uniform velocity, which is applicable when the viscosity of the intruding fluid is not much smaller than that of the ambient fluids. We find that a number of our results are recoverable under these assumptions. Other two-layer flows most relevant to our work include those of Kowal & Worster (2015), in which the intruding fluid is supplied from below rather than from above, its generalisation to power-law fluids (Leung & Kowal, 2022*a*; Gyllenberg & Sayag, 2022) and related two-layer flows down an inclined plane (Shah *et al.*, 2021).

We begin with a theoretical development, deriving the governing equations and similarity solutions in two-dimensional and axisymmetric geometries in §2.2. We also characterise a frontal singularity by performing an asymptotic analysis near the nose of the intruding layer in both geometries. We use our similarity solutions in the two geometries to map out the range of different flow behaviours in §2.3, discussing changes in the flow regimes as parameters vary and some asymptotic limits. Finally, we finish with concluding remarks in §2.4.

2.2 Theoretical development

Consider the flow of two thin films of incompressible, Newtonian viscous fluids of viscosities μ_u and μ_l and densities ρ_u and ρ_l in the configuration depicted in the schematic of Figure 2.1. The subscripts $_u$ and $_l$ correspond to quantities involving the upper and lower layers, respectively. The plane $z = 0$ denotes a rigid, horizontal substrate that has been initially pre-wetted with a uniform depth h_∞ of lower-layer fluid. The thicknesses of the upper and lower layers are denoted by $H(\boldsymbol{x},t)$ and $h(\boldsymbol{x},t)$, respectively, where $\boldsymbol{x}$ is the spatial variable, $\boldsymbol{x} = (r,\theta,z)$ or (x,y,z) in the axisymmetric and two-dimensional geometry, respectively.

Although the flow is depicted in an axisymmetric geometry in Figure 2.1, we consider both axisymmetric and two-dimensional geometries in this work. In the axisymmetric geometry, the two fluids are supplied from a point source at the origin, while in the two-dimensional geometry,

the fluids are instead supplied from a line source at $x = 0$. The upper viscous fluid occupies a region from the source up to the intrusion front, denoted by $r = r_N(t)$ in the axisymmetric geometry and $x = x_N(t)$ in the two-dimensional geometry. The intrusion front is a moving boundary that splits the domain into two regions: a two-layer region, involving both viscous fluids ($0 < r < r_N(t)$ and $0 < x < x_N(t)$ in the axisymmetric and two-dimensional geometries, respectively), and a single-layer region ($r > r_N(t)$ and $x > x_N(t)$ in the axisymmetric and two-dimensional geometries, respectively) of the same material properties as the lower-layer fluid.

In developing a theoretical framework, we assume negligible inertia and surface tension, corresponding respectively to small reduced Reynolds and large Bond numbers, so that the flow is governed by a balance between viscous and buoyancy forces, and interfacial mixing may be neglected (Huppert, 1982*b*). We also assume that the horizontal length scale associated with the two films of viscous fluid is much greater than the corresponding vertical length scale, and that vertical shear provides the dominant resistance to the flow. We, therefore, apply the approximations of lubrication theory and obtain the momentum equations

$$\mathbf{0} = -\nabla p_i + \rho_i \boldsymbol{g} + \mu_i \frac{\partial^2 \boldsymbol{u}_i}{\partial z^2}, \tag{2.1}$$

where $\boldsymbol{u}_i = \boldsymbol{u}_i(\boldsymbol{x}, t)$ is the velocity, assumed to be horizontal, the subscript $i = u, l$ denotes the upper and lower layers, respectively, $\boldsymbol{g} = -g\mathbf{e}_z$ is the acceleration due to gravity, and $\mathbf{e}_z$ is the unit basis vector in the z-direction.

Our approach is in line with generalised frameworks for two-layer thin film flows (e.g. Christy & Hinton, 2023; Gyllenberg & Sayag, 2022) and the related work of Dauck *et al.* (2019). The latter presented generalised equations for a variation of the problem studied here, later focusing on the limit in which $\rho_u = \rho_l$. Here, we explore flows for which $\rho_u < \rho_l$ and investigate additional buoyancy effects present in this scenario, which, in particular, change the behaviour of the flow near the intrusion front. We note that the equal density limit is a singular limit in which the order of the equations reduces by one, giving rise to shock-front solutions. These no longer appear when the densities are unequal.

In what follows, we obtain depth-integrated governing equations modelling the flow in axisymmetric and two-dimensional geometries simultaneously. The main difference between the two geometries is the orientation of vectors, such as the velocity vector $\boldsymbol{u}_i$. These vectors are aligned with the radial and x-directions in the axisymmetric and two-dimensional geometries, respectively. We organise the main governing equations by the relevant regions: the two-layer region and the single-layer region.

2.2.1 The two-layer region

Given that vertical shear stresses provide the dominant resistance to the flow, the pressure in the two layers is hydrostatic, so that

$$p_u = \rho_u g(H + h - z), \tag{2.2}$$

$$p_l = \rho_u g H + \rho_l g(h - z), \tag{2.3}$$

(see Kowal & Worster, 2015, for example). We assume the upper layer is stress-free at its upper surface, so that

$$\mu_u \frac{\partial \boldsymbol{u}_u}{\partial z} = 0 \quad \text{at} \quad z = H + h. \tag{2.4}$$

We assume that the velocity and shear stress at the interface between the upper and lower fluids are continuous, so that

$$\boldsymbol{u}_l = \boldsymbol{u}_u \qquad \text{at} \quad z = h, \tag{2.5}$$

$$\mu_l \frac{\partial \boldsymbol{u}_l}{\partial z} = \mu_u \frac{\partial \boldsymbol{u}_u}{\partial z} \quad \text{at} \quad z = h. \tag{2.6}$$

We also assume that the lower layer satisfies the no-slip condition at the substrate, so that

$$\boldsymbol{u}_l = 0 \quad \text{at} \quad z = 0. \tag{2.7}$$

Solving (2.1) for the velocity field subject to (2.4)–(2.7) gives

$$\boldsymbol{u}_u = \left(\frac{(h-z)(h+2H-z)}{2\mu_u} - \frac{hH}{\mu_l} \right) (\nabla p_u)\big|_{z=h} - \frac{h^2}{2\mu_l} (\nabla p_l)\big|_{z=h}, \tag{2.8}$$

$$\boldsymbol{u}_l = -\frac{Hz}{\mu_l} (\nabla p_u)\big|_{z=h} + \frac{z(z-2h)}{2\mu_l} (\nabla p_l)\big|_{z=h}. \tag{2.9}$$

Integrating these velocities across the depth of each layer yields the depth-integrated flux of upper- and lower-layer fluid, per unit width, given by

$$\boldsymbol{q}_u = -\frac{\rho_u g}{3\mu_l} \left[\left(\mathcal{M} H^3 + \frac{3}{2} H h^2 + 3 H^2 h \right) (\nabla H + \nabla h) + \frac{3}{2} \mathcal{D} H h^2 \nabla h \right], \tag{2.10}$$

$$\boldsymbol{q}_l = -\frac{\rho_u g}{3\mu_l} \left[\left(\frac{3}{2} H h^2 + h^3 \right) (\nabla H + \nabla h) + \mathcal{D} h^3 \nabla h \right]. \tag{2.11}$$

These align with the relevant expressions presented in Kowal & Worster (2015) and Dauck *et al.* (2019) in two-dimensional and axisymmetric configurations. Here, the dimensionless

parameters

$$\mathcal{M} = \frac{\mu_l}{\mu_u}, \tag{2.12}$$

$$\mathcal{D} = \frac{\rho_l - \rho_u}{\rho_u}, \tag{2.13}$$

define the viscosity ratio and relative density difference, respectively.

The upper surface and the interface between the two fluids evolve in line with the mass conservation equations,

$$\frac{\partial H}{\partial t} + \nabla \cdot \boldsymbol{q}_u = 0, \tag{2.14}$$

$$\frac{\partial h}{\partial t} + \nabla \cdot \boldsymbol{q}_l = 0, \tag{2.15}$$

for the upper and lower layers, respectively. These equations, along with the equations (2.10)–(2.11) for the depth-integrated fluxes, fully specify the evolution of the two free surfaces, subject to appropriate boundary conditions, which we discuss in §2.2.3 and §2.2.4.

2.2.2 The single-layer region

In the single-layer region, we retain the subscript $_l$ to reflect that the material properties are the same as that of the lower layer upstream of the intrusion front. Similarly to the two-layer region, the pressure is hydrostatic in the single-layer region, so that

$$p_l = \rho_l g(h - z), \tag{2.16}$$

(see Huppert, 1982*b*). The upper surface satisfies the stress-free condition,

$$\mu_l \frac{\partial \boldsymbol{u}_l}{\partial z} = 0 \quad \text{at} \quad z = h, \tag{2.17}$$

and we assume the no-slip condition at the substrate,

$$\boldsymbol{u}_l = 0 \quad \text{at} \quad z = 0. \tag{2.18}$$

Solving (2.1) subject to (2.17) and (2.18) for the velocity profile and integrating across the depth of the current gives rise to the depth-integrated flux

$$\boldsymbol{q}_l = -\frac{\rho_u g}{3\mu_l}(\mathcal{D} + 1)h^3 \nabla h, \tag{2.19}$$

in line with Huppert (1982*b*). This is supplemented by the mass conservation equation

$$\frac{\partial h}{\partial t} + \nabla \cdot \boldsymbol{q}_l = 0, \tag{2.20}$$

which determines the evolution of the free surface. What remains to do to close the problem is to specify the remaining boundary conditions and matching conditions to couple the two regions, which we organise by geometry.

2.2.3 Axisymmetric currents

In the axisymmetric geometry, the upper and lower layers flow radially outwards so that $\boldsymbol{q}_u = q_u \boldsymbol{e_r}$ and $\boldsymbol{q}_l = q_l \boldsymbol{e_r}$, where $\boldsymbol{e}_r$ is the radial unit basis vector. We outline the corresponding boundary conditions and matching conditions across the intrusion front below.

Following Kowal & Worster (2015), we assume that the upper and lower layers are supplied at a constant source flux $\hat{Q}_u$ and $\hat{Q}_l$, respectively, at the origin, so that

$$\lim_{r\to 0} 2\pi r q_u = \hat{Q}_u, \tag{2.21}$$

$$\lim_{r\to 0} 2\pi r q_l = \hat{Q}_l. \tag{2.22}$$

The thickness and the flux of the lower layer are continuous across the intrusion front $r = r_N(t)$, so that

$$[h]^+_- = 0 \quad \text{at} \quad r = r_N, \tag{2.23}$$

$$[q_l]^+_- = 0 \quad \text{at} \quad r = r_N. \tag{2.24}$$

In addition, the upper-layer flux vanishes at the front, so that

$$q_u = 0 \quad \text{at } r = r_N. \tag{2.25}$$

The front evolves kinematically, which gives rise to an evolution equation for the frontal position,

$$\frac{dr_N}{dt} = \lim_{r\to r_N^-} \frac{q_u}{H}, \tag{2.26}$$

as in Kowal & Worster (2015, 2019*a*,*b*) and Gyllenberg & Sayag (2022), for example. In the far field, we approach a uniform thickness so that

$$\lim_{r\to\infty} h = h_\infty. \tag{2.27}$$

This condition implies that the flux vanishes in the far field.

The boundary conditions and matching conditions specified in this section fully close the

problem for the evolution of the two liquid layers. This includes the frontal position, which needs to be determined as part of the solution of the problem.

Self-similar axisymmetric flows

Although there is an externally imposed vertical length scale, h_∞, the lack of a horizontal length scale is sufficient to allow for the existence of a similarity solution, which we can also deduce by performing a scaling analysis. In the axisymmetric geometry, such similarity solutions exist only when the source flux is constant, as assumed here. However, as discussed in §2.2.4, similarity solutions do not exist if the source flux is constant in the two-dimensional geometry. Instead it is necessary for the source flux to follow a specific power-law, proportional to t^a for some constant $a \neq 0$, in order for similarity solutions to exist in two dimensions. For a related problem in which a viscous gravity current intrudes at the interface between two dissimilar fluids, it has been reported that in either geometry, the late-time behaviour of the injected fluid depends crucially on a (Lister & Kerr, 1989). Below a critical value, the injected fluid reduces in height with time, allowing for one to approximate the lower fluid layer to be uniform in height. Above the critical value, the injected fluid height increases with time, allowing the effects of the lower fluid to be neglected, thus recovering the classical single-layer gravity current. At the critical value, the injected fluid height is constant in time and exact similarity solutions exist (Lister & Kerr, 1989).

Formally, solutions obtained from specific initial conditions approach a similarity solution at late times for diffusive problems of the type considered here (Ball & Huppert, 2019). This is seen also in analogue laboratory experiments, in which flows become self-similar after an initial transient (Huppert, 1982*b*).

To formulate the governing equations in terms of similarity variables and to non-dimensionalise the problem, we introduce the following change of variables

$$(\xi, \xi_N) = \left(\frac{Qt}{2\pi h_\infty}\right)^{-1/2} (r, r_N) = (2\pi)^{\frac{3}{8}} \left(\frac{\rho_u g Q^3}{3\mu_l}\right)^{-\frac{1}{8}} t^{-\frac{1}{2}} (r, r_N), \tag{2.28}$$

for the spatial variable and the frontal position,

$$\big(F(\xi), f(\xi)\big) = \frac{1}{h_\infty}\big(H(r,t), h(r,t)\big) = (2\pi)^{\frac{1}{4}} \left(\frac{\rho_u g}{3\mu_l Q}\right)^{\frac{1}{4}} \big(H(r,t), h(r,t)\big), \tag{2.29}$$

for the thicknesses, and

$$\big(\phi_u(\xi), \phi_l(\xi)\big) = \sqrt{\frac{2\pi t}{h_\infty Q}}\big(q_u(r,t), q_l(r,t)\big) = \left(\frac{(2\pi)^5 \rho_u g t^4}{3\mu_l Q^5}\right)^{\frac{1}{8}} \big(q_u(r,t), q_l(r,t)\big) \tag{2.30}$$

for the flux of both layers. Here, we define

$$Q = 2\pi h_\infty^4 \frac{\rho_u g}{3\mu_l} \tag{2.31}$$

to be a dimensional measure of the flux associated with a depth of h_∞. Using this measure, we non-dimensionalise the source fluxes as

$$(Q_u, Q_l) = Q^{-1}(\hat{Q}_u, \hat{Q}_l). \tag{2.32}$$

Substituting into the governing equations (2.14–2.15) and (2.20), describing mass conservation, yields the ordinary differential equations

$$-\frac{1}{2}F'\xi + \frac{1}{\xi}(\xi\phi_u)' = 0, \tag{2.33}$$

$$-\frac{1}{2}f'\xi + \frac{1}{\xi}(\xi\phi_l)' = 0, \tag{2.34}$$

where the radial components of the fluxes of fluid within the two layers, in both regions of the domain are given by

$$\phi_u = \begin{cases} -\left[\left(\mathcal{M}F^3 + \frac{3}{2}Ff^2 + 3F^2 f\right)(F' + f') + \frac{3}{2}\mathcal{D}Ff^2 f'\right], & 0 < \xi < \xi_N, \\ 0, & \xi \geq \xi_N, \end{cases} \tag{2.35}$$

and

$$\phi_l = \begin{cases} -\left[\left(\frac{3}{2}Ff^2 + f^3\right)(F' + f') + \mathcal{D}f^3 f'\right], & 0 < \xi < \xi_N, \\ -(\mathcal{D}+1)f^3 f', & \xi \geq \xi_N. \end{cases} \tag{2.36}$$

These are obtained from equations (2.10–2.11) and (2.19). Here, the prime $'$ denotes differentiation with respect to ξ. These equations are supplemented by the boundary conditions

$$\xi\phi_u \to Q_u, \quad \xi\phi_l \to Q_l, \quad \text{as} \quad \xi \to 0^+, \tag{2.37}$$

$$[f]_-^+ = 0, \quad [\phi_l]_-^+ = 0, \quad \phi_u = 0, \quad \text{at} \quad \xi = \xi_N, \tag{2.38}$$

$$\frac{\phi_u}{F} \to \frac{1}{2}\xi_N, \quad \text{as} \quad \xi \to \xi_N^-, \tag{2.39}$$

$$f \to 1, \quad \text{as} \quad \xi \to \infty, \tag{2.40}$$

at the source, at the intrusion front, and in the far field, all derived from the dimensional boundary conditions (2.21)–(2.27). This system of differential equations and corresponding boundary conditions and matching conditions fully prescribes the evolution of the two layers in similarity coordinates. These equations were solved using a shooting method implemented using Mathematica's in-built solver *NDSolve*. The governing equations were integrated outwards from the

front on a finite domain. Instead of subtracting the singularities at $\xi = 0$ and $\xi = \xi_N$ analytically, the domain was truncated to avoid the singular points and auxiliary boundary conditions using the asymptotic solution of the next section, §2.2.3, were implemented. Numerical tests were performed to ensure that the computed solutions are independent of all numerical parameters, including the truncation of the computational domain. In particular, these numerical parameters were varied over a range of values, with no observable effect on the numerical solutions within the plotted region. Numerical results are discussed in subsequent sections.

Asymptotic solutions near the nose of axisymmetric intrusions

Near the intrusion front $\xi = \xi_N$, the normal component of the upper-layer flux ϕ_u and the upper-layer thickness F tend to 0, while thickness gradients and stress diverge. A similar stress singularity features at the intrusion front of single-layer (Huppert, 1982*b*) and two-layer (Kowal & Worster, 2015, 2019*b*; Gyllenberg & Sayag, 2022; Leung & Kowal, 2022*a*,*b*) viscous gravity currents under the approximations of lubrication theory. The stress singularity arises within the lubrication formulation and does not represent a genuine physical singularity; rather, it reflects the breakdown of the lubrication assumptions in the immediate vicinity of the front, where the underlying asymptotic scalings are no longer valid.

We examine the singular point $\xi = \xi_N$ asymptotically by performing a local analysis following the approach of Huppert (1982*b*), Kowal & Worster (2015) and Leung & Kowal (2022*a*). As shown in Appendix A, we obtain asymptotic solutions that feature a square-root singularity of the form

$$F \sim A_1\delta^{\frac{1}{2}} + A_2\delta + \cdots, \tag{2.41}$$

$$f \sim a_0 + a_1\delta^{\frac{1}{2}} + a_2\delta + \cdots, \tag{2.42}$$

valid for $\delta = (1 - \xi/\xi_N) \ll 1$. Equations (A.3) and (A.10)–(A.11) in Appendix A demonstrate that the coefficients a_1, A_2, and a_2 of the higher-order terms can be written in terms of A_1, a_0 and ξ_N. The latter set of coefficients can be determined by matching to the outer numerical solutions. This square-root singularity is also observed by Lister & Kerr (1989) in a similar scenario involving a thin current moving over a nearly uniform lower layer, and by Dauck *et al.* (2019) in the equal-density limit. The asymptotic solution identified by Lister & Kerr (1989) in this scenario is in agreement with (2.41)–(2.42) if we set $Q_l = 0$ to account for the lower layer remaining uniform.

The asymptotic approximations (2.41)–(2.42) elucidate the behaviour near the front and inform an appropriate scheme for the numerical solution of the full system of governing differential equations. These asymptotic solutions are shown in Figure 2.2a up to $O(\delta^{1/2})$ and $O(\delta)$, in comparison to the full numerical solutions, which are valid throughout the domain. As expected, the more terms we include in the asymptotic expansion, the better the agreement with

the full numerical solution near the front, as can be seen by including terms up to $O(\delta)$ versus terms up to $O(\delta^{1/2})$. Our asymptotic calculation also indicates that the upper-layer pressure gradient, $F' + f'$, is singular at the front, while the lower-layer pressure gradient, $F' + (1+\mathcal{D})f'$, is non-singular.

We note that the structure of the frontal singularity at $\xi = \xi_N$ differs from that of single-layer viscous gravity currents propagating over a rigid horizontal substrate, for which the thickness is $O(\delta^{1/3})$, rather than $O(\delta^{1/2})$, as $\delta \to 0$ (Huppert, 1982*b*). This also contrasts with the structure of the singularity at the front of a thin film of viscous fluid spreading beneath another viscous gravity current, for which the thickness of the intruding layer is also $O(\delta^{1/3})$ as $\delta \to 0$ (Kowal & Worster, 2015, 2019*a*,*b*).

We include $O(\delta)$ terms in the asymptotic solution (2.41)–(2.42) during the initialization of the numerical computation, as they play a role in determining the lower-layer flux at the nose. In particular, replacing quantities associated with the lower layer by their asymptotic approximations gives rise to the following leading-order asymptotic expression for the lower-layer flux,

$$\phi_l = \frac{3a_0^2A_1^2\mathcal{D}}{4\xi_N(\mathcal{D}+1)} + \frac{a_0^3}{\xi_N}A_2 + \frac{a_0^3(\mathcal{D}+1)}{\xi_N}a_2 + O(\delta^{\frac{1}{2}}), \tag{2.43}$$

which simplifies to

$$\phi_l = \frac{a_0\xi_N}{3} - \frac{a_0^2A_1^2\mathcal{D}}{4\xi_N(\mathcal{D}+1)} + O(\delta^{\frac{1}{2}}), \tag{2.44}$$

using (A.10)–(A.11). Importantly, (2.43) shows that the leading order contribution to ϕ_l includes correction terms involving the second-order coefficients a_2 and A_2. The appearance of these coefficients in the leading-order expression for the lower-layer flux emphasises the need to determine them, which is equivalent to determining the $O(\delta)$ terms in the asymptotic solution (2.41)–(2.42).

2.2.4 Two-dimensional currents

In the two-dimensional configuration, the upper and lower layers flow in the x-direction so that $\boldsymbol{q}_u = q_u\boldsymbol{e_x}$ and $\boldsymbol{q}_l = q_l\boldsymbol{e_x}$, where $\boldsymbol{e}_x$ is the unit basis vector in the x-direction. Below, we specify the associated boundary conditions and matching conditions to couple the two regions of the flow.

For reasons described in §2.2.3, we assume that the upper and lower layers are supplied at a specified line flux $\hat{Q}_u t^a$, $\hat{Q}_l t^a$, respectively, where $\hat{Q}_u$, $\hat{Q}_l$ and $a > -1$ are constants. Explicitly,

$$q_u = \hat{Q}_u t^a, \quad q_l = \hat{Q}_l t^a \quad \text{at} \quad x = 0. \tag{2.45}$$

Equivalently, the volume of injected fluid is given by $\hat{Q}_u t^{a+1}/(a+1)$ and $\hat{Q}_l t^{a+1}/(a+1)$ for the upper and lower layers, respectively. When $-1 < a < 0$, the two fluids are supplied at a rate that

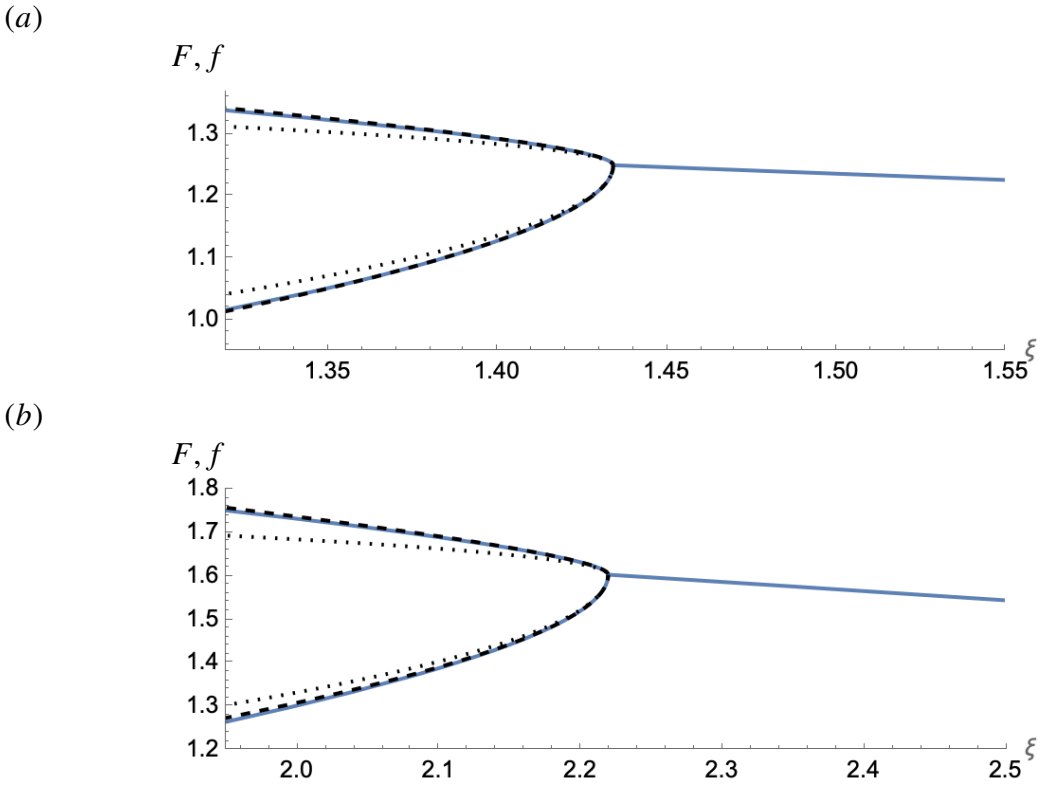

Figure 2.2: The full numerical solution versus the asymptotic solutions (2.41)–(2.42) near the intrusion front in (a) axisymmetric and (b) two-dimensional geometries, for $\mathcal{M} = 0.1$, $\mathcal{D} = 0.3$, $Q_u = 1$ and $Q_l = 0.5$. Solid curves: full numerical solution. Dotted curves: asymptotic solution containing terms up to $O(\delta^{1/2})$. Dashed curves: asymptotic solution containing terms up to $O(\delta)$.

is decreasing with time from a point singularity at $t = 0$, while the volume is increasing with time. Experimentally, such a flow can be achieved by releasing a finite volume of fluid at $t = 0$, followed by a time-dependent supply of fluid at the source; however, the imposed release is an idealisation and may not be realised exactly in practice.

The thickness and the normal flux of the lower layer are assumed to be continuous across the intrusion front $x = x_N(t)$, so that (2.23)–(2.24) hold but at $x = x_N$ rather than at $r = r_N$. In addition, the normal component of the upper-layer flux vanishes at the front, so that (2.25) holds but at $x = x_N$. The front evolves kinematically, which yields the evolution equation (2.26) for the frontal position, with r_N replaced by x_N. In the far field, the thin film approaches a uniform thickness so that (2.27) continues to hold. These boundary/matching conditions and the two-dimensional version of the system of differential equations (2.10–2.11), (2.14–2.15), (2.19–2.20) are sufficient to fully specify the evolution of the two-dimensional flow.

Self-similar two-dimensional flows

In contrast to axisymmetric flows, similarity solutions do not exist in the two-dimensional geometry when the flux is constant, as mentioned in §2.2.3. Instead, a specific power-law is required for a similarity solution to exist, consistently with prior work on related problems (Lister & Kerr, 1989; Dauck *et al.*, 2019). In particular, the flow becomes self-similar when $a = -\frac{1}{2}$, as can be seen through a scaling argument. Such similarity solutions serve as attractors, to which other two-dimensional solutions, associated with different initial conditions, converge at late times (Ball & Huppert, 2019). To formulate the governing equations in similarity variables, we introduce the following change of variables

$$(\xi, \xi_N) = \frac{h_\infty}{Qt^{1/2}}(x, x_N) = \left(\frac{3\mu_l}{\rho_u g Q^3}\right)^{\frac{1}{5}} t^{-\frac{1}{2}}(x, x_N), \tag{2.46}$$

for the spatial coordinate and the frontal position,

$$\big(F(\xi), f(\xi)\big) = \frac{1}{h_\infty}\big(H(x,t), h(x,t)\big) = \left(\frac{\rho_u g}{3\mu_l Q^2}\right)^{\frac{1}{5}} \big(H(x,t), h(x,t)\big), \tag{2.47}$$

for the thicknesses, and

$$\big(\phi_u(\xi), \phi_l(\xi)\big) = Q^{-1} t^{\frac{1}{2}} \big(q_u(x,t), q_l(x,t)\big), \tag{2.48}$$

for the fluxes of the two layers. Here, we define

$$Q = \left(\frac{\rho_u g}{3\mu_l}\right)^{\frac{1}{2}} h_\infty^{\frac{5}{2}} \tag{2.49}$$

to be a dimensional measure characterising the flux associated with a thickness of h_∞. Using this measure, we express the two constants describing the source fluxes in dimensionless form as

$$(Q_u, Q_l) = Q^{-1}(\hat{Q}_u, \hat{Q}_l). \tag{2.50}$$

In similarity coordinates, the governing equations yield the following system of ordinary differential equations

$$-\frac{1}{2}F'\xi + \phi_u' = 0, \tag{2.51}$$

$$-\frac{1}{2}f'\xi + \phi_l' = 0, \tag{2.52}$$

describing conservation of mass within the two layers, where the upper- and lower-layer fluxes in both regions of the domain, upstream and downstream of the intrusion front, are given by the same expressions (2.35)–(2.36) as in the axisymmetric geometry.

As we switch to the two-dimesional geometry, the only boundary conditions that change are the source flux conditions

$$\phi_u = Q_u, \quad \phi_l = Q_l \quad \text{at} \quad \xi = 0. \tag{2.53}$$

The remaining boundary conditions and matching conditions remain the same. This includes continuity of thickness and flux across the intrusion front (2.38), the kinematic condition for the evolution of the intrusion front (2.39), and the far-field condition (2.40). These governing equations and boundary conditions are sufficient to fully determine the two-dimensional similarity solutions.

Asymptotic solutions near the nose of two-dimensional intrusions

It can be verified that the local analysis of §2.2.3, including the asymptotic solutions (2.41)–(2.42) and the relationships between a_1, A_2, and a_2 and the quantities A_1, a_0 and ξ_N apply to the two-dimensional geometry without modification. The expansions are identical in the two geometries as the analysis is local to the front and the governing equations are identical in the two geometries apart from differences in the divergence in flux (factors of ξ and $1/\xi$), which only affects the asymptotic solution at higher orders. Apart from differences in the divergence in flux, the equations are identical because the similarity scalings reflect a *non-constant* source flux (proportional to $t^{-1/2}$) in the two-dimensional case and a *constant* source flux in the axisymmetric case. Had the source fluxes in both geometries been constant, there would have been additional differences in the governing equations, and hence in the asymptotic solutions, between the two geometries. An illustration of this difference includes prior work in which the intruding layer is supplied from below (see Kowal & Worster, 2015, for example).

A comparison between the asymptotic solutions up to $O(\delta^{1/2})$ and up to $O(\delta)$ against the

full numerical solutions, valid throughout the whole domain, is shown in Figure 2.2b in the two-dimensional geometry. As in the axisymmetric case, it is unsurprising that there is better agreement between the asymptotic solutions and the full numerical solutions near the front, the more terms are included in the asymptotic expansion. In particular, including terms up to $O(\delta)$ improves the agreement over a wider neighbourhood of the front in comparison to terms up to $O(\delta^{1/2})$. The structure of the singularity remains the same as in the axisymmetric geometry; namely, the thickness is $O(\delta^{1/2})$ as $\delta \to 0$. This contrasts with the structure of the frontal singularity for single-layer viscous gravity currents propagating over a rigid horizontal substrate, and for thin films of viscous fluid intruding beneath another viscous gravity current (Huppert, 1982*b*; Kowal & Worster, 2015, 2019*a*,*b*).

2.3 Results and discussion

As found in §2.2, the flow of thin films of viscous fluid over pre-lubricated substrates depends upon the four dimensionless parameters $\mathcal{M}$, $\mathcal{D}$, Q_u and Q_l, yielding a range of different flow regimes. Figure 2.3 depicts typical similarity solutions for the profile thicknesses of the two layers in axisymmetric and two-dimensional geometries as the viscosity ratio $\mathcal{M}$ and fluxes Q_u and Q_l vary, while the flux ratio Q_l/Q_u remains fixed. The main difference in the profiles between the two geometries is the presence of a logarithmic singularity at the origin, in which the thickness of both layers diverges, for axisymmetric flows. This is a purely geometric effect, arising from the fact that axisymmetric flows are supplied at non-zero flux from a point source. This is also the case for single-layer axisymmetric flows supplied at non-zero flux (Huppert, 1982*b*).

A range of possible flow profiles across parameter space is displayed in Figures 2.3a,b for the axisymmetric and two-dimensional geometries, respectively. Relative to the lower layer, the upper layer is thick and of small extent when the viscosity ratio is low and the upper-layer flux is high, as seen in the top-left panels of Figures 2.3a,b, and thin when the viscosity ratio is high, as seen in the top-right panels. Decreasing the upper-layer flux reduces the thickness and extent of the upper layer, as seen in the bottom-right panels of Figures 2.3a,b, while decreasing the viscosity ratio further increases the thickness of the upper layer, and reduces its extent, as seen in the bottom-left panels of Figures 2.3a,b. In general, low viscosity ratios correspond to thick upper layers, while high viscosity ratios correspond to thin upper layers, which coat the lower layer from above. Such low-viscosity, thin coating films exert negligible traction at the interface between the two fluids and only negligibly affect the dynamics of the lower layer, save near the front.

There is a change in behaviour of the flow as we traverse from the origin to the nose, in that the contribution $q_{lb} \equiv -(1+\mathcal{D})f^3 f'$ to the lower-layer flux from gravitational spreading under its own weight (associated with lower-layer buoyancy forces) is positive near the source

(*a*)

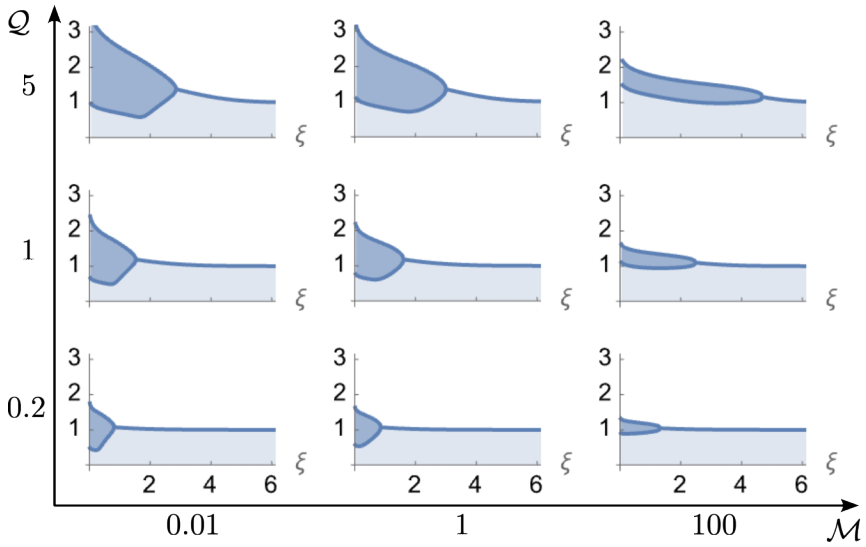

(*b*)

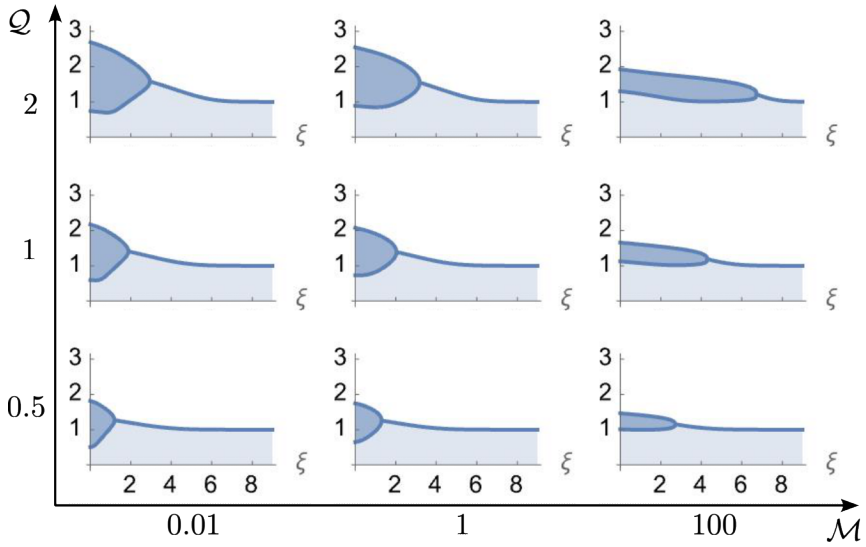

Figure 2.3: Numerical solutions for the self-similar flow of a thin film of viscous fluid spreading over another thin film of fluid in (*a*) axisymmetric and (*b*) two-dimensional geometries for various viscosity ratios $\mathcal{M}$ and source fluxes Q_u and Q_l, such that $Q_u = 5Q_l = Q$. The density difference is fixed at $\mathcal{D} = 1$.

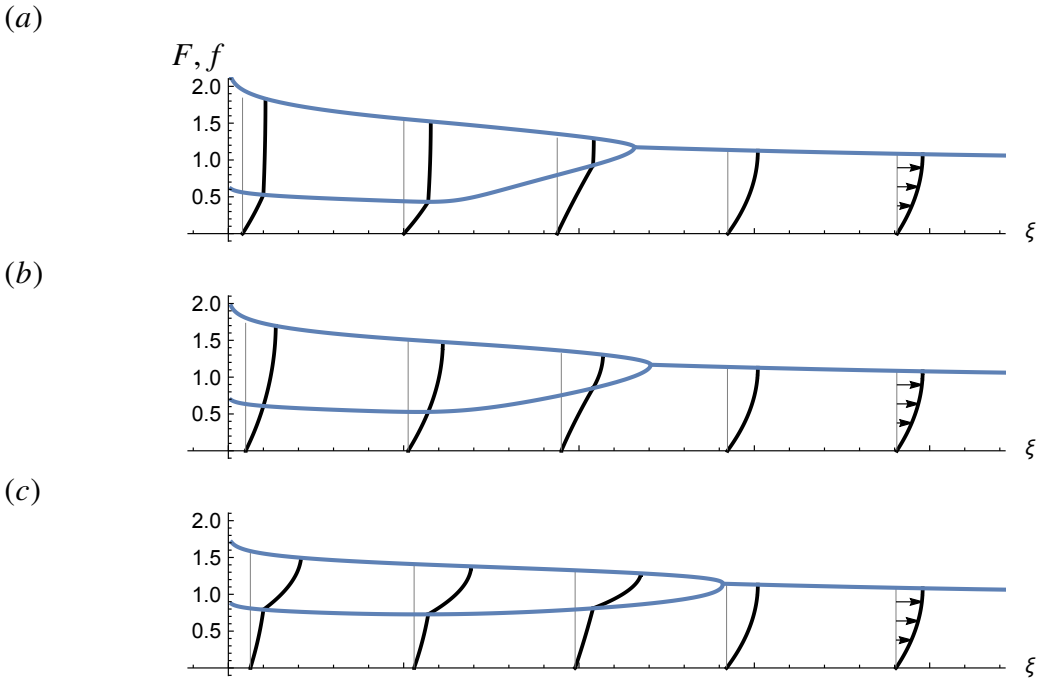

Figure 2.4: Radial velocity profiles in similarity coordinates (in the axisymmetric geometry), integrated over a disc of radius ξ, for (a) $\mathcal{M} = 0.1$, (b) $\mathcal{M} = 1$, and (c) $\mathcal{M} = 10$, where $\mathcal{D} = 0.5$, $Q_u = 0.5$, $Q_l = 0.1$.

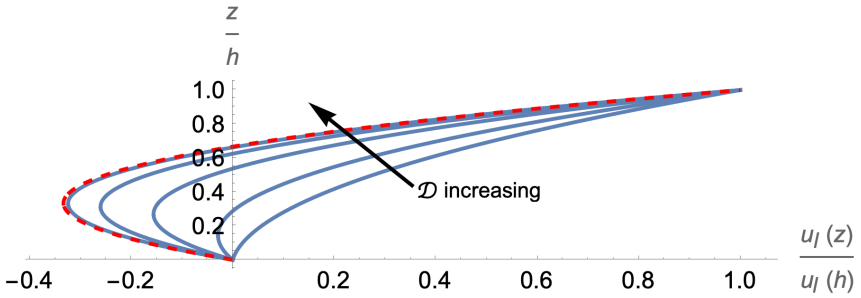

Figure 2.5: Scaled lower-layer radial velocity near the nose as a function of depth in similarity coordinates in the axisymmetric geometry (solid curves), evaluated at $\xi = 0.99\xi_N$ for varying $\mathcal{D} = 0.5, 1, 3, 10, 500$ and $\mathcal{M} = 10$, $Q_u = 0.1$, $Q_l = 0.001$. The velocity becomes negative near the lower boundary for large enough density differences. These velocity profiles are compared against the lower-layer velocity profile predicted by Lister & Kerr (1989), which is valid for $Q_u \ll 1$ and $Q_l = 0$ (dashed red curve).

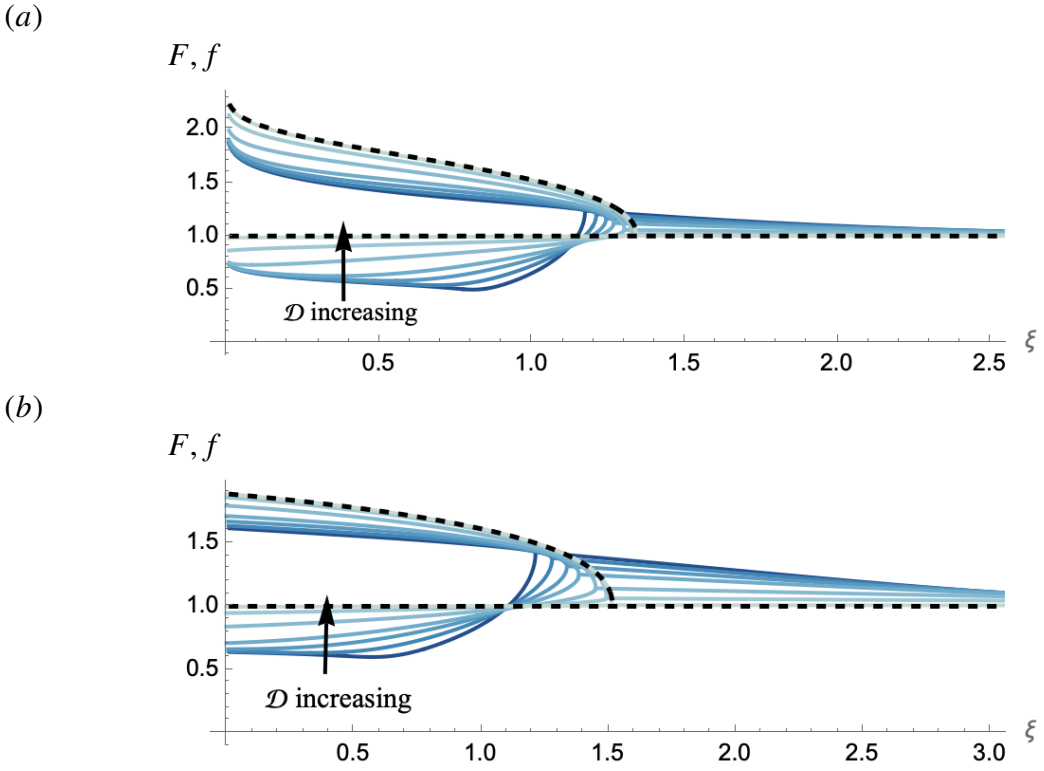

Figure 2.6: Profile thicknesses (solid curves) in (a) axisymmetric and (b) two-dimensional geometries as the density difference varies, in comparison to the large-$\mathcal{D}$ asymptotic solution (dashed curve). Parameter values used: $\mathcal{M} = 2$, $\mathcal{D} = 0.05, 0.2, 0.5, 1, 3, 10, 100$, $Q_l = 0.1$ and $Q_u = 0.5$.

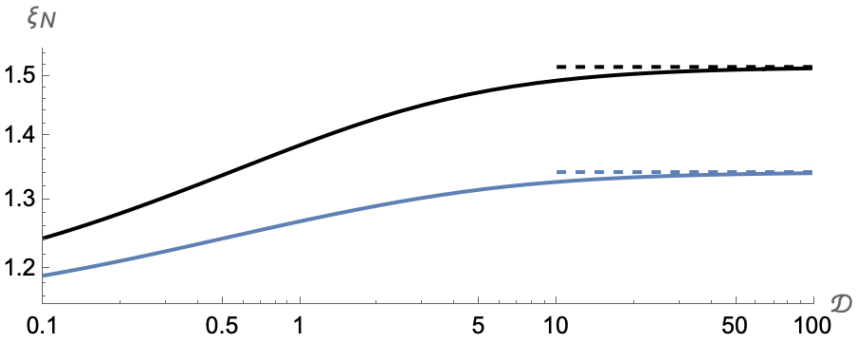

Figure 2.7: The extent of the intruding layer of fluid as a function of the density difference. The large $\mathcal{D}$ limit is shown as a dashed curve. Parameter values used: $\mathcal{M} = 2$, $Q_l = 0.1$ and $Q_u = 0.5$. Blue: axisymmetric flows. Black: two-dimensional flows.

and negative near the front, as can be identified by examining the sign of f'. In particular, as displayed in the top-left panels of Figure 2.3a,b, for example, the interface slope f' changes sign from negative near the source to positive near the front, and hence the opposite sign change occurs for q_{lb}. This indicates that lower-layer buoyancy forces tend to decrease the outwards flow of the lower layer near the front. These buoyancy forces are relatively more important, over a larger proportion of the domain the more viscous the upper layer (the smaller $\mathcal{M}$ is). For very viscous upper layers, the flow is mainly uniform within the upper layer and the curvature of the interface between the two layers is relatively small over most of the domain, save for a small region in which the slope of the interface between the two layers changes sign, as demonstrated in the top-left panels of Figure 2.3a,b and in Figure 2.4. That is, the change in sign of q_{lb} is more pronounced the more viscous the upper layer. This occurs in both axisymmetric and two-dimensional geometries, which precludes geometric effects, arising from the singularity at the origin in the axisymmetric geometry.

The flow at low viscosity ratios is equivalent to the upper layer being almost solid and lubricated from below by a much less viscous fluid. Rescaling variables with respect to the upper layer rather than the lower layer reveals an analogy to the plug flow of a thin film of viscous fluid over an inviscid layer. This regime is in some degree relevant to experiments involving the flow of ice shelves floating freely over the ocean, except that here we neglect the resistance of viscous extensional stress or any transverse shear stress, which would be more important than shear stress in nature. Examples include experiments of viscous gravity currents over an inviscid layer in unconfined geometries (Robison *et al.*, 2010; Pegler & Worster, 2012) and in a narrow channel (Pegler *et al.*, 2013; Kowal & Worster, 2016). Another example involves experiments of the formation of lava deltas in the limit in which the injected fluid is less dense than the ambient inviscid layer (Taylor-West *et al.*, 2024).

Radial velocity profiles of the two thin films are depicted in Figure 2.4 in an axisymmetric geometry for various viscosity ratios. As shown in Figure 2.4a, the velocity profile is mainly uniform within the upper layer for small viscosity ratios and most of the shear is confined to the lower layer alone. The flow of the lower layer transitions from a primarily Couette flow, upstream of the intrusion front, to a parabolic Poiseuille flow ahead of the intrusion front. As the viscosity ratio increases, the upper layer thins and its velocity increases, as do the velocity gradients within the upper layer, as shown in Figures 2.4b,c.

As seen in Figure 2.5, for large enough density differences, the velocity of the lower layer near the intrusion front becomes negative (the flow reverses) near the lower boundary. This reflects the existence of a stagnation line (where the velocity is zero), which intersects the bottom boundary near the front. Similar flow reversals have been reported by Lister & Kerr (1989), in the limiting scenario in which the lower layer is shallow, which requires $Q_u \ll 1$ and $Q_l = 0$ in our notation. In fact, the velocity profiles of Figure 2.5 approach that of Lister & Kerr (1989) (shown in Figure 2.5 as a dashed red curve, from their equation (2.27)) as $\mathcal{D} \to \infty$. Such

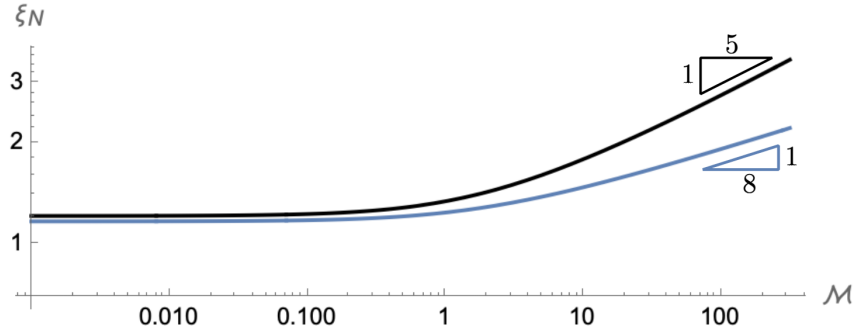

Figure 2.8: The extent of the intruding layer of fluid as a function of the viscosity ratio. Parameter values used: $\mathcal{D} = 2$, $Q_l = 0.1$ and $Q_u = 0.5$. Blue: axisymmetric flows. Black: two-dimensional flows.

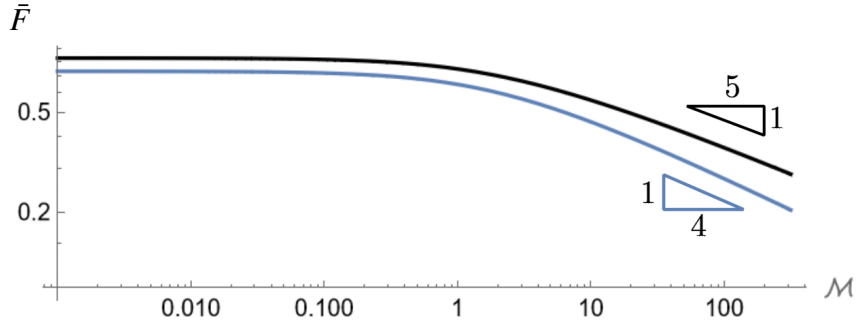

Figure 2.9: The average thickness of upper layer as a function of the viscosity ratio. Parameter values used: $\mathcal{D} = 2$, $Q_l = 0.1$ and $Q_u = 0.5$. Blue: axisymmetric flows. Black: two-dimensional flows.

flow reversals occur above a critical value of the density difference, above which the lower layer spreads mainly under its own weight. In particular, in contrast to single-layer flows, gradients of the lower-layer thickness are positive near the nose, giving rise to negative contributions to the velocity profile, akin to those of blade coating problems. This effect is more pronounced for low viscosity ratios, for which the upper layer is relatively more viscous in comparison to the lower layer and there are greater thickness gradients near the nose. An alternative explanation for this reverse flow near the front can be understood by considering mass conservation. The negative velocity near the substrate counteracts higher velocities near the interface, arising from viscous coupling between the two layers, so as to conserve mass. This is particularly relevant when the density of the lower layer greatly exceeds that of the upper layer (large $\mathcal{D}$), in which case the lower-layer thickness gradient and flux become small.

As seen in the numerical solutions displayed in Figure 2.6, it is interesting to note that the slope of the interface between the two layers steepens as we decrease the density difference towards zero. The smaller the density difference, the steeper the interface near the intrusion front. As the density difference decreases, these solutions approach a shock front in which the thickness of the upper layer is nonzero at the front while the thickness of lower layer is discontinuous. These shock-front solutions arise in the equal-density regime under the approximations of lubrication theory, as described by Dauck *et al.* (2019), when the viscosity ratio is large enough.

(*a*)

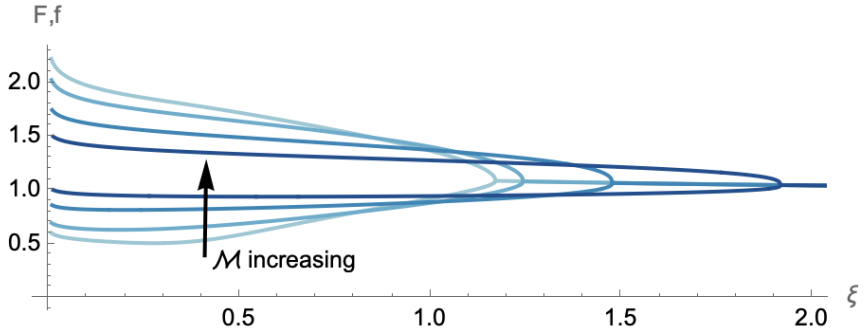

(*b*)

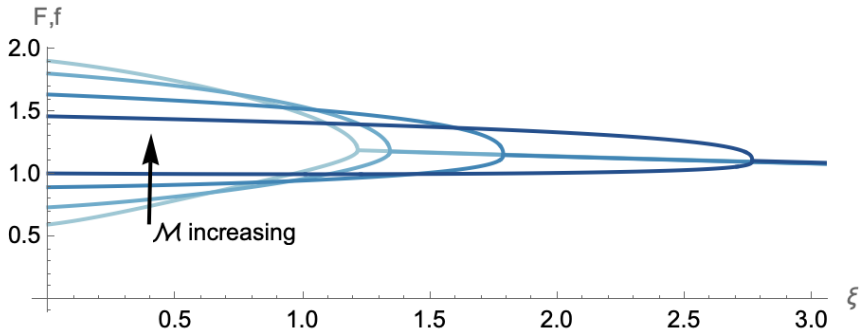

Figure 2.10: Profile thicknesses in (*a*) axisymmetric and (*b*) two-dimensional geometries as the viscosity ratio varies. Parameter values used: $\mathcal{D} = 2$, $\mathcal{M} = 0, 1, 10, 100$, $Q_l = 0.1$ and $Q_u = 0.5$.

On the other hand, as the density difference approaches infinity, the lower layer becomes significantly denser than the upper layer and the interface between the two layers becomes flat to leading order, as demonstrated through an asymptotic analysis for $\mathcal{D} \gg 1$, outlined in Appendix B. Asymptotic solutions valid for $\mathcal{D} \gg 1$ are overlain in Figure 2.6, depicting a close match to full numerical solutions when $\mathcal{D}$ is large. The higher the density difference $\mathcal{D}$, the flatter the interface between the two fluids, as depicted in Figure 2.6.

In contrast to changes in the thickness gradients near the nose, the position of the nose varies only minimally as the density difference varies over three orders of magnitude, as shown in Figure 2.7. With the chosen scaling for the similarity variable ξ as defined in (2.28) for the axisymmetric geometry and (2.46) for the two-dimensional geometry, this implies that the speed of the upper-layer fluid remains largely unchanged by the density of the lower-layer fluid.

There are two asymptotic regimes corresponding to small and large viscosity ratios $\mathcal{M}$ as depicted in Figures 2.8 and 2.9, which display the frontal position ξ_N and the average thickness of the upper layer as a function of the viscosity ratio and how these approach different power laws in both regimes. We examine these regimes by rescaling the dependent variables with respect to the lower (or upper) layer for small (or large) viscosity ratios. For large viscosity ratios ($\mu_u \ll \mu_l$), the upper layer is much more mobile, undergoing larger deformations than the lower layer. This gives rise to upper layers that are long and thin as depicted in the right-hand panels of Figures 2.3*a*, *b* and in Figure 2.10. In this regime, the deformation of the lower layer is negligible compared to that of the upper layer, and the nose position can be determined solely

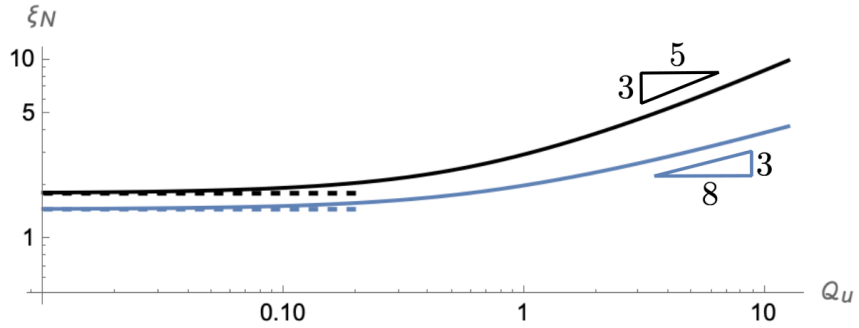

Figure 2.11: The extent of the intruding layer of fluid as a function of the upper-layer flux. Asymptotic solutions for $Q_u \ll 1$, derived in Appendix C, are shown as dashed lines. Parameter values used: $\mathcal{M} = 2$, $\mathcal{D} = 1$ and $Q_l = 1$. Blue: axisymmetric flows. Black: two-dimensional flows.

(a)

(b)

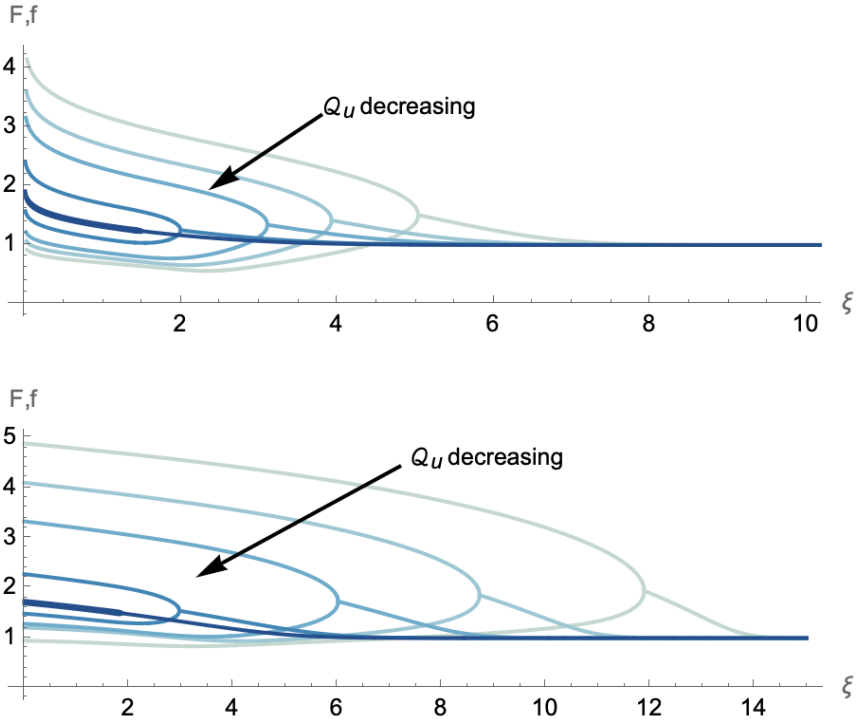

Figure 2.12: Profile thicknesses in (a) axisymmetric and (b) two-dimensional geometries as the upper-layer flux varies. Parameter values used: $\mathcal{M} = 2$, $\mathcal{D} = 1$, $Q_l = 1$ and $Q_u = 0.05, 1, 5, 10, 20$.

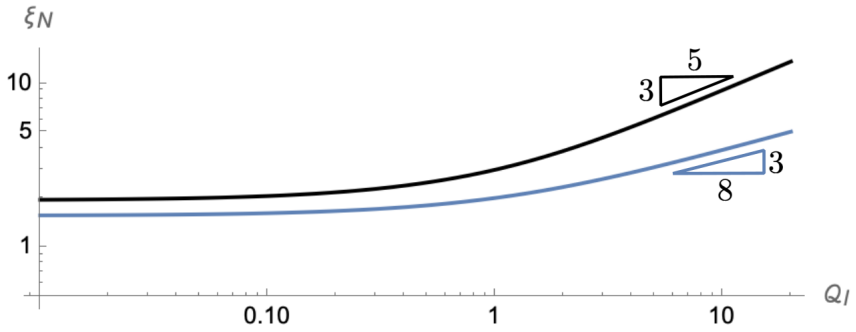

Figure 2.13: The extent of the intruding layer of fluid as a function of the lower-layer flux. Parameter values used: $\mathcal{M} = 2$, $\mathcal{D} = 1$ and $Q_u = 1$. Blue: axisymmetric flows. Black: two-dimensional flows.

by the upper layer. Therefore, we expect the nose position to scale with the horizontal length scale associated with the deformation of the upper layer. That is, it is appropriate to scale the similarity variable ξ with respect to quantities describing the properties of the upper layer. This can be done by rescaling the spatial similarity coordinate (2.28) and (2.46) by a factor of $\mathcal{M}^{1/8}$ in the axisymmetric geometry and $\mathcal{M}^{1/5}$ in the two-dimensional geometry, and the thickness (2.29) and (2.47) by a factor of $\mathcal{M}^{-1/4}$ in the axisymmetric geometry and $\mathcal{M}^{-1/5}$ in the two-dimensional geometry. As shown in Figure 2.8, the nose position indeed varies as $\mathcal{M}^{1/8}$ and $\mathcal{M}^{1/5}$ for $\mathcal{M} \gg 1$, in the axisymmetric and two-dimensional geometries, respectively. Similarly, the average thickness of the upper layer indeed scales as $\mathcal{M}^{-1/4}$ and $\mathcal{M}^{-1/5}$ for $\mathcal{M} \gg 1$, in the axisymmetric and two-dimensional geometries, respectively, as shown in Figure 2.9.

For small viscosity ratios ($\mu_u \gg \mu_l$), the upper layer is much less mobile, undergoing much smaller deformations than the lower layer. The upper layer thickness is large relative to the lower layer and its extent is small as depicted in the left-hand panels of Figure 2.3a, b and in Figure 2.10 for a range of values of the viscosity ratio. In this regime, the lower layer undergoes significantly greater deformation compared to the upper layer, and so the nose position is solely determined by lower-layer dynamics. As such, scaling with respect to quantities describing the properties of the lower layer is appropriate, as in our initial choice of similarity scalings (2.28)–(2.30) and (2.46)–(2.48). Under this choice of scaling, we expect the nose position to approach a constant as the viscosity ratio approaches zero ($\mathcal{M} \ll 1$), which is confirmed in Figure 2.8. Similarly, the average upper-layer thickness approaches a constant as the viscosity ratio approaches zero ($\mathcal{M} \ll 1$), as depicted in Figure 2.9.

As illustrated in Figure 2.11 in both geometries, variations in the upper-layer flux Q_u lead to two distinct parameter regimes, characterised by whether $Q_u \ll Q_l \sim Q_\infty$ or $Q_u \gg Q_l \sim Q_\infty$, given a fixed value of $Q_l \sim Q_\infty$. Here, Q_∞ is a dimensionless measure of flux associated with the depth of the lower layer in the far-field. Although we find it illuminating to refer to Q_∞ explicitly in this discussion, we note that owing to our choice of similarity scalings, we have $Q_\infty = 1$. Thickness profiles in both of these parameter regimes are depicted in Figure 2.12 for

(*a*)

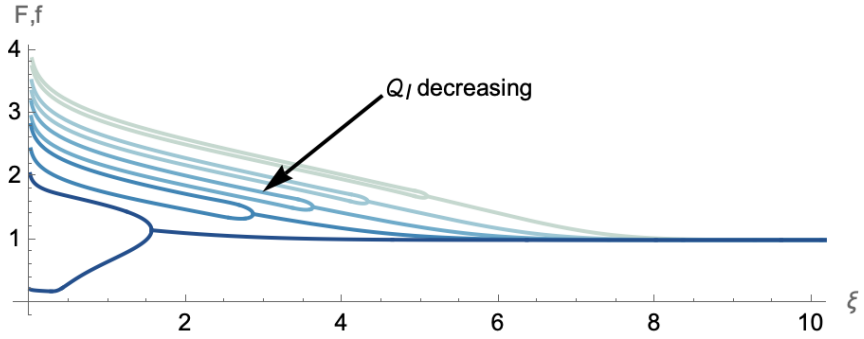

(*b*)

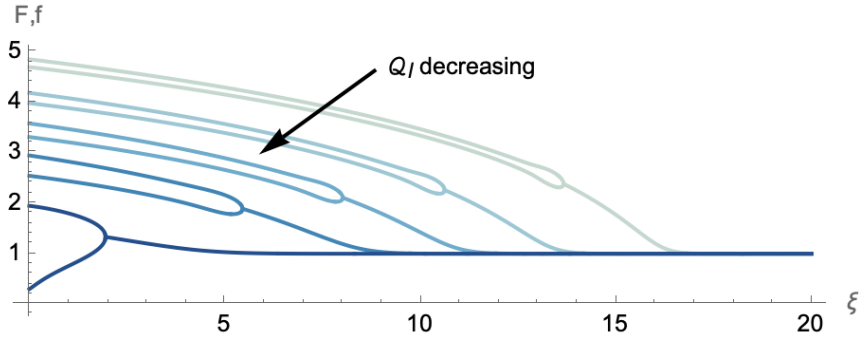

Figure 2.14: Profile thicknesses in (*a*) axisymmetric and (*b*) two-dimensional geometries as the lower-layer flux varies. Parameter values used: $\mathcal{M} = 2$, $\mathcal{D} = 1$, $Q_u = 1$ and $Q_l = 20, 13, 8, 4, 0.01$.

a range of values of Q_u. In the former regime ($Q_u \ll Q_l \sim Q_\infty$), the nose position is determined by the dynamics of the lower layer, which is fed at a specified flux determined by Q_l, so that ξ_N tends towards a constant as $Q_u \to 0$. We examine this regime in more detail in Appendix C, where we arrive at an asymptotic solution for the nose position when $Q_u \ll 1$, which compares well against the full numerical solutions, as shown in Figure 2.11. The upper layer thickness becomes small in this regime and scales with $Q_u \ll 1$. In the latter regime ($Q_u \gg Q_l \sim Q_\infty$), the upper layer is much thicker than the lower layer, as shown in Figure 2.12. The nose position in this regime is determined by the dynamics of the upper layer, for which the effects of the lower layer are negligible. In effect, the dynamics of the upper layer tend towards that of a single-layer viscous gravity current fed at a specified flux determined by Q_u as $Q_u \to \infty$. Therefore, the nose position ξ_N scales with the upper-layer flux as $Q_u^{3/5}$ in the two-dimensional geometry and $Q_u^{3/8}$ in the axisymmetric geometry, as confirmed the power laws depicted in Figure 2.11. These can be obtained by rescaling the similarity variable ξ in terms of the upper-layer source flux instead of Q.

Similarly, as illustrated in Figure 2.13 for both geometries, variations in the lower-layer flux Q_l lead to two slightly different parameter regimes: $Q_l \ll Q_u \sim Q_\infty$ or $Q_l \gg Q_u \sim Q_\infty$, given a fixed value of $Q_u \sim Q_\infty$. In the former regime, ξ_N approaches a constant as $Q_l \to 0$. In the latter regime, the upper layer forms a thin film that coats the underlying fluid from above, as depicted in Figure 2.14. In this regime, the lower layer drags the upper layer along with it and

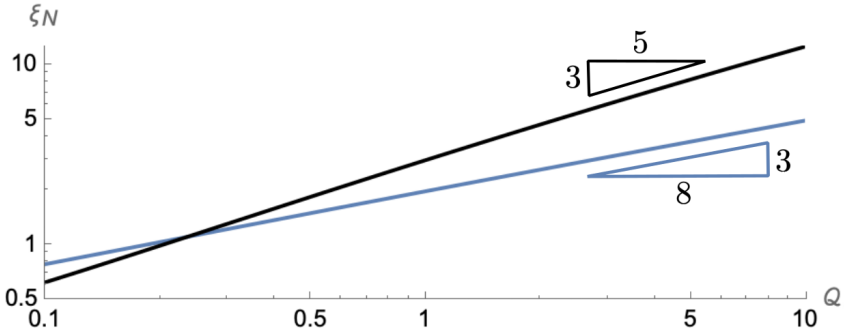

Figure 2.15: The extent of the intruding layer of fluid as a function of both of the upper- and lower- layer flux. Parameter values used: $\mathcal{M} = 2$, $\mathcal{D} = 1$, and $Q_u = Q_l = Q \in [0.1, 10]$. Blue: axisymmetric flows. Black: two-dimensional flows.

.

(a)

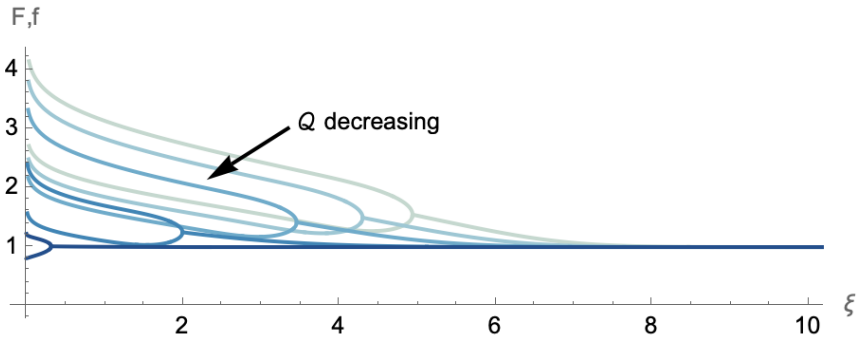

(b)

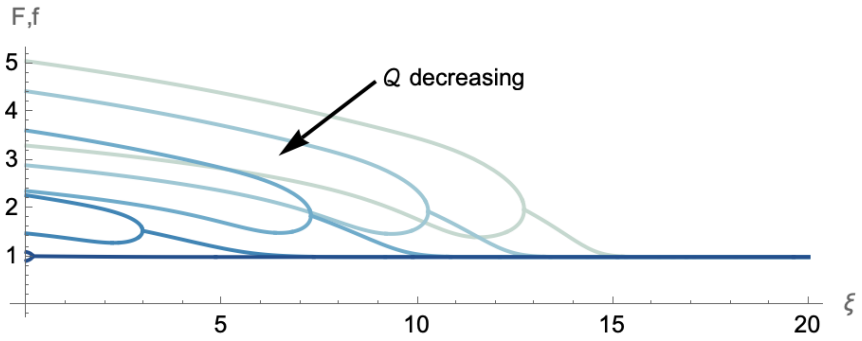

Figure 2.16: Profile thicknesses in (a) axisymmetric and (b) two-dimensional geometries as both the upper- and lower-layer fluxes vary. Parameter values used: $\mathcal{M} = 2$, $\mathcal{D} = 1$, and $Q_u = Q_l = Q = 0.01, 1, 4, 7, 10$.

behaves as a single-layer viscous gravity current fed at a specified flux determined by Q_l, with a pre-wetting film of small thickness. As such, the nose position ξ_N scales with the lower-layer flux as $Q_l^{3/5}$ in the two-dimensional geometry and $Q_l^{3/8}$ in the axisymmetric geometry, which is confirmed by the power laws depicted in Figure 2.13. These can be obtained by rescaling the similarity variable ξ in terms of the lower-layer source flux instead of Q.

In contrast to Figures 2.11 and 2.13, Figure 2.15 displays the frontal position ξ_N as the upper- and lower-layer fluxes vary whilst their ratio is kept constant. Specifically, we set $Q_u \sim Q_l \sim Q$ and note that the nose position scales as $Q^{3/5}$ in the two-dimensional geometry and $Q^{3/8}$ in the axisymmetric geometry for both $Q \ll 1$ and $Q \gg 1$. When $Q \ll 1$, both source fluxes are negligible and so $\xi_N \to 0$ as displayed in Figure 2.15. This contrasts with the regimes in which $Q_u \ll Q_l \sim Q_\infty$ and $Q_l \ll Q_u \sim Q_\infty$, discussed previously. The value of Q effectively determines the depth of the two layers in comparison to the far field depth. Small values of Q give rise to flows over a deep lower layer, which is effectively uniform, while large values of Q correspond to flows over a thin lower layer, where lower-layer fluid prominently accumulates ahead of the intrusion front as shown in Figure 2.16.

2.4 Conclusions

In this work, we examined the flow of a viscous gravity current spreading over a thin film of viscous fluid of dissimilar density and viscosity. We considered similarity solutions in axisymmetric and two-dimensional configurations and characterised the flow across parameter space spanned by four key dimensionless parameters: the viscosity ratio, the density difference, and the dimensionless source fluxes for the two layers. In particular, we characterised the thicknesses and velocities of the two layers as well as the extent of the upper layer as parameters vary. We have also conducted an asymptotic analysis of a stress singularity that forms at the intrusion front when the density difference is nonzero, obtaining asymptotic solutions valid near the front.

We found that a range of flow behaviours is possible depending on the dimensionless parameters and we discussed possible asymptotic regimes. In terms of shape, the upper layer is thick and of small extent for small viscosity ratios and small upper-layer source fluxes, and it is thin and of large extent for large viscosity ratios and large upper-layer source fluxes. There are notable differences in the velocity profiles for different viscosity ratios. For small viscosity ratios, the velocity profile is mainly uniform within the upper layer while most of the shear is confined to the lower layer alone, which is characterised by a primarily Couette (Poiseuille) flow upstream (downstream) of the intrusion front. This is no longer the case for large viscosity ratios, for which the velocity of the upper layer and its gradients become relatively large and most of the shear is instead confined to the upper layer.

Our study also indicates that thickness gradients near the intrusion front steepen as the den-

sity difference between the two layers decreases, ultimately approaching a shock-front solution in the equal-density regime. Large density differences give rise to dynamics that would not be expected in the equal-density regime, including flow reversals near the intrusion front owing to the gravitational spreading of the lower layer under its own weight. While the frontal position changes only gradually with the density difference, the thicknesses of the two layers and, in particular, the front steepness, undergo more pronounced changes as the density difference varies.

A particular regime of interest is one in which the viscosity ratio is large, which corresponds to thin films of viscous fluid spreading over a much more viscous lower layer. These flows mimic those of thin films spreading over a soft, deformable substrate. As demonstrated in a companion paper (Yang & Kowal, 2025), these flows are susceptible to a novel viscous fingering instability, referred to as a non-porous viscous fingering instability. The instability is similar to, yet distinct from, the Saffman-Taylor viscous fingering instability in that it does not involve a Hele-Shaw cell or other porous medium.

Chapter 3

Non-porous viscous fingering of a thin film of fluid spreading over a lubricated substrate

The content of this chapter (and the relevant part of Chapter 1) has been published in

- Yang, H. and Kowal, K. N. (2025) Non-porous viscous fingering of a thin film of fluid spreading over a lubricated substrate. *J. Fluid Mech.*, 1013: A32.

3.1 Introduction

In this chapter, we demonstrate that the base flows investigated in Chapter 2 are susceptible to a novel viscous fingering instability. In particular, we examine the formation of viscous fingering instabilities that emerge when a viscous gravity current intrudes radially outwards over another thin film of viscous fluid, where the two fluids are of unequal densities and viscosities. By conducting a linear stability analysis using the axisymmetric similarity solutions of Chapter 2 as the base flow, we characterise the parameter space over which these instabilities occur. We also compare it with instabilities that emerge when the injected fluid intrudes from below. To formulate the problem, we directly build upon the framework of Chapter 2 and Dauck *et al.* (2019) by allowing for variations in the azimuthal direction. We also refer to the experiments of Dauck (2020), where similar frontal instabilities emerge. The linear stability analysis of Dauck (2020), focusing on the limit in which the two layers are of equal density, also confirms these instabilities but did not reveal a most unstable wavenumber, much like the equal-density stability calculations of Kowal & Worster (2019*b*) when the less viscous fluid intrudes from below and growth rates increase with the wavenumber indefinitely. Interestingly, no instabilities were observed in related experiments of Lister & Kerr (1989), involving a thin film of viscous fluid intruding at a fluid interface, save for small-scale frontal patterning attributed to contamination of

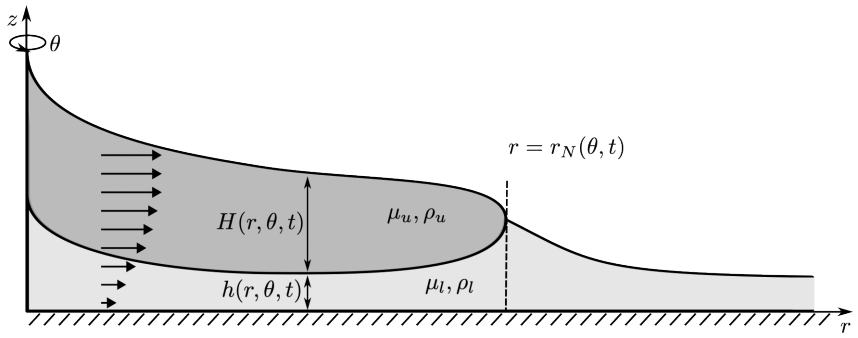

Figure 3.1: Schematic of a thin film of viscous fluid spreading over a lubricated substrate in an axisymmetric geometry. Schematic adapted from Yang *et al.* (2024).

the fluid surface by dust. We find through our stability calculations that the parameter regime in which the latter experiments were performed correspond to stable configurations. Other relevant works include single-layer (Smith, 1969; Huppert, 1982*b*,*a*) and two-layer (Kowal & Worster, 2015; Dauck *et al.*, 2019; Shah *et al.*, 2021) flows over horizontal and inclined substrates, and non-Newtonian analogues (Hewitt, 2013; Gyllenberg & Sayag, 2022; Hinton, 2022; Christy & Hinton, 2023), to name a few.

We begin with a theoretical development in §3.2, in which the geometry of the problem, the assumptions, and the governing equations are laid out. We investigate the stability of the flow to small non-axisymmetric disturbances by performing a linear stability analysis in §3.3, in which we also derive asymptotic solutions for perturbations around a stress singularity at the injection front. We solve the resulting perturbation equations numerically, characterise the instability across parameter space and further discuss our results in §3.4. We finalise with concluding remarks in §3.5.

3.2 Theoretical development

As depicted in Figure 3.1, we consider the flow of two thin films of incompressible, Newtonian viscous fluids of constant viscosities μ_u and μ_l and constant densities ρ_u and ρ_l in an axisymmetric geometry. The subscripts $_u$ and $_l$ correspond to quantities involving the upper and lower layers, respectively. The subscript $_l$ also describes quantities ahead of the intrusion front. We assume that the effects of inertia and surface tension are negligible and that both fluid layers are long and thin, and are resisted dominantly by vertical shear stresses within the limits of lubrication theory.

We note that the use of the lubrication approximation reflects an idealised scenario in which only vertical shear stress appears, and we aim to determine whether or not this suffices to explain the emergence of instability. Strictly speaking, the approximations of lubrication theory break down at the nose, where there is a frontal stress singularity, thus warranting the need for the

solution of the full Stokes equations near the nose. We do not attempt this in this paper. We note that the experiments of Dauck (2020), performed in a similar configuration to the present paper, and their close agreement to theoretical predictions (which make use of lubrication theory) for their propagation and shape (Dauck, 2020; Dauck *et al.*, 2019), give credence to the use of lubrication theory at least as a first attempt upon which higher-order corrections can be made in the future. Another similar example is the experiments and stability analysis of Kowal & Worster (2019*b*), which similarly made use of the lubrication approximation, albeit in a different configuration (in that the less viscous fluid intrudes from below rather than from above).

The two fluids are supplied at constant fluxes $\hat{Q}_u$ and $\hat{Q}_l$ at the origin and spread radially outwards over a horizontal, rigid substrate, which is pre-wetted by the lower-layer fluid to an initial, uniform depth h_∞. While the two fluids spread radially outwards, we allow for non-axisymmetric variations in the flow. The upper current extends to the intrusion front $r = r_N(\theta, t)$, which splits the domain into two regions: a two-layer region $0 < r < r_N$, involving both viscous fluids, and a single-layer region $r > r_N$, involving a single viscous fluid of the same material properties as the underlying layer of the two-layer region. The thicknesses of the upper and lower layers are denoted by $H(r, \theta, t)$ and $h(r, \theta, t)$, respectively.

Applying the standard lubrication approximation (see Yang *et al.* (2024) for details of the derivation in the axisymmetric case) results in the following mass conservation equations

$$\frac{\partial H}{\partial t} + \nabla \cdot \boldsymbol{q}_u = 0, \tag{3.1}$$

$$\frac{\partial h}{\partial t} + \nabla \cdot \boldsymbol{q}_l = 0, \tag{3.2}$$

within the two layers, where the depth-integrated fluxes of upper- and lower-layer fluid are given by

$$\boldsymbol{q}_u = \begin{cases} -\dfrac{\rho_u g}{3\mu_l}\left[\left(\mathcal{M}H^3 + \frac{3}{2}Hh^2 + 3H^2h\right)(\nabla H + \nabla h) + \frac{3}{2}\mathcal{D}Hh^2\nabla h\right] & (0 < r < r_N), \\ 0 & (r \geq r_N), \end{cases} \tag{3.3}$$

$$\boldsymbol{q}_l = \begin{cases} -\dfrac{\rho_u g}{3\mu_l}\left[\left(\frac{3}{2}Hh^2 + h^3\right)(\nabla H + \nabla h) + \mathcal{D}h^3\nabla h\right] & (0 < r < r_N), \\ -\dfrac{\rho_u g}{3\mu_l}(\mathcal{D}+1)h^3\nabla h & (r \geq r_N), \end{cases} \tag{3.4}$$

in terms of the dimensionless parameters

$$\mathcal{M} = \frac{\mu_l}{\mu_u} \quad \text{and} \quad \mathcal{D} = \frac{\rho_l - \rho_u}{\rho_u}, \tag{3.5}$$

which denote the viscosity ratio and relative density difference, respectively. In general, the quantities described here may vary in θ.

At the origin, $r = 0$, we assume that the upper and lower layers are supplied at a constant

flux $\hat{Q}_l$, $\hat{Q}_u$, respectively, so that

$$\lim_{r\to 0} 2\pi r \boldsymbol{q}_u \cdot \boldsymbol{e}_r = \hat{Q}_u, \tag{3.6}$$

$$\lim_{r\to 0} 2\pi r \boldsymbol{q}_l \cdot \boldsymbol{e}_r = \hat{Q}_l, \tag{3.7}$$

where $\boldsymbol{e}_r$ is the radial unit basis vector.

The thickness and the normal flux of the lower layer are continuous across the intrusion front $r = r_N(\theta, t)$, so that

$$[h]^+_- = 0 \quad \text{at } r = r_N, \tag{3.8}$$

$$[\boldsymbol{q}_l \cdot \boldsymbol{n}]^+_- = 0 \quad \text{at } r = r_N, \tag{3.9}$$

where $\boldsymbol{n}$ is the outward unit normal vector to the intrusion front. In addition, the normal component of the upper-layer flux vanishes at the front, so that

$$\boldsymbol{q}_u \cdot \boldsymbol{n} = 0 \quad \text{at } r = r_N. \tag{3.10}$$

The front evolves kinematically, so that

$$\dot{r}_N = \lim_{r\to r_N^-} H^{-1} \boldsymbol{q}_u \cdot \boldsymbol{\nabla}(r - r_N) = \lim_{r\to r_N^-} \left[\frac{\boldsymbol{q}_u \cdot \boldsymbol{e}_r}{H} - \frac{\boldsymbol{q}_u \cdot \boldsymbol{e}_\theta}{H r_N} \frac{\partial r_N}{\partial \theta} \right]. \tag{3.11}$$

Here, $\boldsymbol{e}_\theta$ is the azimuthal unit basis vector. In the far field, we assume that the thickness is uniform so that

$$\lim_{r\to\infty} h = h_\infty. \tag{3.12}$$

These governing equations, boundary conditions, matching conditions, and the evolution equation for the front, fully specify the moving boundary problem considered in this paper.

3.3 Non-axisymmetric disturbances

We investigate the evolution of non-axisymmetric disturbances of the base flow by expanding about the zeroth-order axisymmetric similarity solutions of Yang *et al.* (2024). In the present study, we restrict attention to real eigenvalues σ. This choice is motivated by experimental observations of closely related configurations, including those reported in Dauck (2020) and earlier experiments by Kowal & Worster (2015). In these systems, the instability is observed to develop monotonically in time, with no evidence of temporal oscillations, suggesting that the dominant eigenvalues are real. Consequently, there is no *a priori* physical motivation to expect complex eigenvalues in the present setting. While it may be of interest in future work to search explicitly for complex eigenvalues, or to establish rigorously that none exist, for example, by

demonstrating that the associated linear operator is self-adjoint, this lies beyond the scope of the current study.

We change the independent variables (r,θ,t) to (ξ,ϑ,τ) and nondimensionalize the system by applying the following transformations

$$(\xi,\xi_N(\vartheta,\tau)) = \left(\frac{3\mu_l}{\rho_u g h_\infty^3 t}\right)^{1/2}(r,r_N(\theta,t)), \quad \vartheta=\theta, \quad \tau=\log(t/t_0), \tag{3.13}$$

$$\big(F(\xi,\vartheta,\tau),f(\xi,\vartheta,\tau)\big) = h_\infty^{-1}\big(H(r,\theta,t),h(r,\theta,t)\big), \tag{3.14}$$

$$\big(\boldsymbol{\phi}_u(\xi,\vartheta,\tau),\boldsymbol{\phi}_l(\xi,\vartheta,\tau)\big) = \left(\frac{3\mu_l t}{\rho_u g h_\infty^5}\right)^{1/2}\big(\boldsymbol{q}_u(r,\theta,t),\boldsymbol{q}_l(r,\theta,t)\big), \tag{3.15}$$

where $t_0 = 3\mu_l/(\rho_u g h_\infty)$. We also rescale the two input source fluxes at the origin so that

$$Q_u = \hat{Q}_u/\hat{Q} \quad \text{and} \quad Q_l = \hat{Q}_l/\hat{Q}, \tag{3.16}$$

where

$$\hat{Q} = 2\pi h_\infty^4 \frac{\rho_u g}{3\mu_l} \tag{3.17}$$

is a dimensional measure of the lower-layer flux associated with a depth of h_∞. Alternatively, the parameter $\hat{Q}$ can be interpreted as the flux required to attain a thickness of h_∞ near the source.

The transformation (3.13)–(3.15) into similarity space transforms the base flow (the similarity solutions of Yang *et al.* (2024)) into a steady solution, which is key to allow a straightforward stability analysis to be performed. This can be seen by examining the transformed system of partial differential equations

$$\frac{\partial F}{\partial\tau} - \frac{1}{2}\frac{\partial F}{\partial\xi}\xi + \frac{1}{\xi}\frac{\partial(\xi\phi_{ur})}{\partial\xi} + \frac{1}{\xi}\frac{\partial\phi_{u\theta}}{\partial\vartheta} = 0, \tag{3.18}$$

$$\frac{\partial f}{\partial\tau} - \frac{1}{2}\frac{\partial f}{\partial\xi}\xi + \frac{1}{\xi}\frac{\partial(\xi\phi_{lr})}{\partial\xi} + \frac{1}{\xi}\frac{\partial\phi_{l\theta}}{\partial\vartheta} = 0, \tag{3.19}$$

describing mass conservation within the two layers of viscous fluid, the coefficients of which are independent of the transformed time variable τ. Here, the radial and azimuthal components of the depth-integrated fluxes of the two layers of fluid are given by

$$(\phi_{ur},\phi_{lr}) = (\boldsymbol{\phi}_u\cdot\boldsymbol{e}_r,\ \boldsymbol{\phi}_l\cdot\boldsymbol{e}_r), \tag{3.20}$$

$$(\phi_{u\theta},\phi_{l\theta}) = (\boldsymbol{\phi}_u\cdot\boldsymbol{e}_\theta,\ \boldsymbol{\phi}_l\cdot\boldsymbol{e}_\theta), \tag{3.21}$$

where

$$\boldsymbol{\phi}_u = \begin{cases} -\left[\left(\mathcal{M}F^3 + \frac{3}{2}Ff^2 + 3F^2 f\right)(\nabla F + \nabla f) + \frac{3}{2}\mathcal{D}Ff^2\nabla f\right] & (0 < \xi < \xi_N) \\ 0 & (\xi \geq \xi_N), \end{cases} \tag{3.22}$$

$$\boldsymbol{\phi}_l = \begin{cases} -\left[\left(\frac{3}{2}Ff^2 + f^3\right)(\nabla F + \nabla f) + \mathcal{D}f^3\nabla f\right] & (0 < \xi < \xi_N) \\ -(\mathcal{D}+1)f^3\nabla f & (\xi \geq \xi_N), \end{cases} \tag{3.23}$$

for the upper and lower layers, respectively. The operator ∇ is now the gradient operator in the two-dimensional polar coordinate system spanned by (ξ, ϑ).

As for the boundary conditions, the source flux boundary conditions reduce to

$$\xi\phi_{ur} \to Q_u, \quad \xi\phi_{lr} \to Q_l \quad (\xi \to 0), \tag{3.24}$$

while the matching conditions at the intrusion front, describing continuity of lower-layer thickness, continuity of lower-layer flux and the zero-flux condition for the upper layer, are given by

$$[f]^+_- = 0, \quad [\boldsymbol{\phi}_l \cdot \boldsymbol{n}]^+_- = 0, \quad \boldsymbol{\phi}_u \cdot \boldsymbol{n} = 0 \quad (\xi = \xi_N), \tag{3.25}$$

respectively, where the normal vector at the intrusion front becomes

$$\boldsymbol{n} = \left(\boldsymbol{e_r} - \frac{1}{\xi_N}\frac{\partial \xi_N}{\partial \vartheta}\boldsymbol{e_\theta}\right)\left(1 + \left(\frac{1}{\xi_N}\frac{\partial \xi_N}{\partial \vartheta}\right)^2\right)^{-1/2}. \tag{3.26}$$

These are supplemented by the kinematic condition, which reduces to

$$\frac{\boldsymbol{e_r}\cdot\boldsymbol{\phi}_u}{F} - \frac{1}{\xi_N}\frac{\partial \xi_N}{\partial \vartheta}\frac{\boldsymbol{e_\theta}\cdot\boldsymbol{\phi}_u}{F} \to \frac{\partial \xi_N}{\partial \tau} + \frac{1}{2}\xi_N \quad (\xi \to \xi_N^-), \tag{3.27}$$

and the far-field condition,

$$f \to 1 \quad (\xi \to \infty), \tag{3.28}$$

reflecting the choice to scale vertical lengths with respect to the dimensional far-field thickness.

These governing equations are a set of nonlinear partial differential equations describing the flow of general disturbances to the axisymmetric base flow. In a later section, we will focus on small-amplitude disturbances and linearise these equations about the base flow. However, the singular structure of the intrusion front raises problems with formulating the small-amplitude equations and boundary conditions consistently. To avoid these issues, we first investigate the structure of the singularity at the intrusion front in the following section, and then use it to make an informed coordinate transformation that will allow for a consistent set of small-amplitude

equations and boundary conditions to be formulated.

3.3.1 Frontal singularity and asymptotic solution

Similar to the behaviour of the unperturbed, axisymmetric flow (the basic state considered in Yang *et al.* (2024)), there is a frontal singularity inherent to the perturbed flow. We generalise the asymptotic analysis of Yang *et al.* (2024) for the unperturbed flow near the intrusion front to include variations in the azimuthal direction and find a generalised asymptotic solution near the front, of the form

$$\begin{aligned} F(\xi,\vartheta,\tau) &\sim A_1(\vartheta,\tau)\left(1-\frac{\xi}{\xi_N}\right)^{\frac{1}{2}} + A_2(\vartheta,\tau)\left(1-\frac{\xi}{\xi_N}\right) + ..., \\ f(\xi,\vartheta,\tau) &\sim a_0(\vartheta,\tau) + a_1(\vartheta,\tau)\left(1-\frac{\xi}{\xi_N}\right)^{\frac{1}{2}} + a_2(\vartheta,\tau)\left(1-\frac{\xi}{\xi_N}\right) + ..., \end{aligned} \tag{3.29}$$

reflecting a square-root singularity, in contrast to the cube-root frontal singularity of a single-layer viscous gravity current (Huppert, 1982*b*). Here, the relationships between the coefficients a_0, a_1, a_2, A_1 and A_2 are given by (see Appendix D for further details)

$$a_1 = -\frac{A_1}{\mathcal{D}+1}, \tag{3.30}$$

$$A_2 = -\frac{4A_1^2}{9a_0}\left(\mathcal{M}-\frac{3}{\mathcal{D}+1}\right), \tag{3.31}$$

$$a_2 = \frac{1}{9(\mathcal{D}+1)a_0^2}\left[3\xi_N\left(\xi_N + 2\frac{\partial\xi_N}{\partial\tau}\right) + A_1^2 a_0\left(4\mathcal{M}-9-\frac{3}{\mathcal{D}+1}\right)\right]. \tag{3.32}$$

As the base flow involves a singularity at the intrusion front, singular terms appear also in the equations governing the perturbations. This prevents one from formulating consistent linearised boundary conditions at the front. A similar problem occurs when linearising about the Barenblatt-Pattle similarity solution and various methods have been introduced to handle it, including the use of the method of strained coordinates (Grundy & McLaughlin, 1982) and a transformation of the dependent variable (Mathunjwa & Hogg, 2006*a*). Instead, we follow an approach similar to that of Kowal & Worster (2019*b*) by simply mapping the two-layer region to a fixed interval $[0,1]$ via the coordinate transformation

$$\Lambda = \xi/\xi_N. \tag{3.33}$$

Such a coordinate transformation eliminates the need to perturb the position of the singular point, which is now fixed at $\Lambda = 1$, for the corresponding boundary conditions. We summarise the equations and boundary conditions for the small-amplitude perturbations in terms of Λ in the following section. However, to aid numerical integration, we further transform the independent

variable nonlinearly by defining

$$\hat{\Lambda} = 1 - (1 - \Lambda)^{1/2} \tag{3.34}$$

in the two-layer region and $\hat{\Lambda} = \Lambda$ in the single layer region. The transformation (3.34) is motivated by our asymptotic solution (3.29), which identifies a square-root singularity near the front. Under the transformation (3.34), the thicknesses of the two layers are instead linear near the intrusion front, and hence their gradients no longer diverge. In essence, the frontal singularity is now a removable singularity, which is simpler to handle numerically.

3.3.2 Small-amplitude perturbations

We wish to examine the evolution of small pertubations to the base, axisymmetric flow, and in order to do so, we linearise the transformed problem by defining

$$X(\xi, \vartheta, \tau) \equiv X(\Lambda, \Theta, \mathcal{T}) = X_0(\Lambda) + \epsilon \tilde{X}_1(\Lambda, \Theta, \mathcal{T}) + ..., \tag{3.35}$$

for variables $X = f, F, \phi_{ur}, \phi_{u\theta}, \phi_{lr}, \phi_{l\theta}, \boldsymbol{\phi}_l, \boldsymbol{\phi}_u$, where ϵ is an arbitrary small number, $\Theta = \vartheta$, $\mathcal{T} = \tau$ and

$$\chi = \chi_0 + \epsilon \tilde{\chi}_1(\Theta, \mathcal{T}) + ..., \tag{3.36}$$

for variables $\chi = \xi_N, a_0, a_1, a_2, A_1, A_2, \boldsymbol{n}$. We note that the governing equations and boundary conditions describing the evolution of the basic state (involving variables with the subscript $_0$) are outlined in Yang *et al.* (2024), which we do not repeat here, for brevity.

To examine the evolution of the perturbations, we search for normal mode solutions of the form

$$\tilde{X}_1(\Lambda, \Theta, \mathcal{T}) = X_1(\Lambda) e^{\sigma \mathcal{T} + ik\Theta}, \tag{3.37}$$

$$\tilde{\chi}_1(\Theta, \mathcal{T}) = \chi_1 e^{\sigma \mathcal{T} + ik\Theta}. \tag{3.38}$$

As the transformed time variable $\mathcal{T}$ is logarithmic in the sense $\mathcal{T} = \tau = \log(t/t_0)$, these normal modes in fact represent algebraic growth/decay of perturbations in physical time t, since $e^{\sigma \mathcal{T}}$ is proportional to t^{σ}. We also note that owing to the transformation $r_N \propto \xi_N t^{1/2}$, if the growth rate satisfies $-1/2 < \sigma < 0$ then the perturbations to r_N will appear to grow even though the perturbations to ξ_N decay.

Substitution into (3.18)–(3.28) yields the following expressions for the perturbed fluxes (see

Appendix E for the coefficient expressions)

$$\phi_{ur1} = \alpha_{u1} f_1 + \alpha_{u2} F_1 + \alpha_{u3} f_1' + \alpha_{u4} F_1' + \alpha_{u5} \xi_{N1}, \tag{3.39}$$

$$\phi_{lr1} = \alpha_{l1} f_1 + \alpha_{l2} F_1 + \alpha_{l3} f_1' + \alpha_{l4} F_1' + \alpha_{l5} \xi_{N1}, \tag{3.40}$$

$$\phi_{u\theta 1} = ik(\alpha_{u3} \Lambda^{-1} f_1 + \alpha_{u4} \Lambda^{-1} F_1 + \alpha_{u5} \xi_{N1}), \tag{3.41}$$

$$\phi_{l\theta 1} = ik(\alpha_{l3} \Lambda^{-1} f_1 + \alpha_{l4} \Lambda^{-1} F_1 + \alpha_{l5} \xi_{N1}), \tag{3.42}$$

and the following perturbed governing equations

$$\sigma\left(F_1 - \frac{\xi_{N1}}{\xi_{N0}} \Lambda F_0'\right) - \frac{1}{2}\Lambda F_1' - \frac{\xi_{N1}}{\xi_{N0}^2 \Lambda} (\Lambda \phi_{u0})' + \frac{1}{\xi_{N0} \Lambda} (\Lambda \phi_{u1})' + \frac{ik}{\xi_{N0} \Lambda} \phi_{u\theta 1} = 0, \tag{3.43}$$

$$\sigma\left(f_1 - \frac{\xi_{N1}}{\xi_{N0}} \Lambda f_0'\right) - \frac{1}{2}\Lambda f_1' - \frac{\xi_{N1}}{\xi_{N0}^2 \Lambda} (\Lambda \phi_{l0})' + \frac{1}{\xi_{N0} \Lambda} (\Lambda \phi_{l1})' + \frac{ik}{\xi_{N0} \Lambda} \phi_{l\theta 1} = 0, \tag{3.44}$$

reflecting mass conservation within the two layers, where the prime symbol represents the derivative respect to Λ and α_{ij} are functions of the basic state quantities, including f_0, F_0, f_0', and F_0', as well as the parameters $\mathcal{M}$ and $\mathcal{D}$ and the unperturbed frontal position ξ_{N0}, as given explicitly in Appendix E.

As for the boundary conditions for the perturbed system, note that the coordinate transformation (3.33) eliminates the need to perturb the value of Λ at which the boundary conditions are applied. The perturbations to the frontal position are instead embedded into the governing equations, and through the appearance of additional terms in some boundary conditions following the linearisation of the normal vector. In particular, we have

$$\Lambda(\xi_{N1} \phi_{ur0} + \xi_{N0} \phi_{ur1}) \to 0, \quad \Lambda(\xi_{N1} \phi_{lr0} + \xi_{N0} \phi_{lr1}) \to 0 \quad (\Lambda \to 0), \tag{3.45}$$

reflecting that both fluids are supplied at a constant flux at the origin, and so the perturbed source fluxes vanish as we approach the origin. The frontal matching conditions for the perturbations reduce to

$$[f_1]_-^+ = 0, \quad [\phi_{lr1}]_-^+ = 0, \quad \phi_{ur1} = 0 \quad (\Lambda = 1), \tag{3.46}$$

reflecting the fact that the perturbed lower-layer thickness and flux is continuous and the perturbed upper-layer flux vanishes at the intrusion front. In simplifying these conditions, we use that $\boldsymbol{n}_0 = \boldsymbol{e}_r$ and that $\boldsymbol{n}_1$ is proportional to the azimuthal basis vector while the flux (for the base flow) is proportional to the radial basis vector, so that $\boldsymbol{\phi}_{u0} \cdot \boldsymbol{n}_1 = 0$ and $\boldsymbol{\phi}_{l0} \cdot \boldsymbol{n}_1 = 0$. A linearisation

of the kinematic condition yields the following boundary condition for the perturbations,

$$\frac{\phi_{ur1}}{F_0} - \frac{F_1\phi_{ur0}}{F_0^2} \to \left(\sigma + \frac{1}{2}\right)\xi_{N1} \quad (\Lambda \to 1^-), \tag{3.47}$$

while the far-field condition requires that the perturbations vanish in the far field,

$$f_1 \to 0 \quad (\Lambda \to \infty). \tag{3.48}$$

We note that this is a differential eigenvalue problem, with eigenfunctions (X_1, χ_1) and eigenvalues σ. That is, the growth rates σ can be found numerically for each wavenumber k, which we discuss in the following section.

3.3.3 Numerical method

We solve the perturbation equations in the variable $\hat{\Lambda}$, as defined in (3.34), by shooting backwards for ξ_{N1} and $Q_{l1}|_{\hat{\Lambda}=L}$ from the far-field at $\hat{\Lambda} = L$, where we define $Q_{i1} = \Lambda\phi_{ir}$ for $i = l, u$ and $L > 1$ is a constant that is sufficiently large that $\hat{\Lambda} = L$ acts as a *pseudo infinity*. To initiate the computations for the single-layer region, we start by specifying values of ξ_{N1} and $Q_{l1}|_{\hat{\Lambda}=L}$ and integrating the equations backwards from $\hat{\Lambda} = L$ towards the intrusion front $\hat{\Lambda} = 1$. Because the intrusion front is a singular point for the governing equations of the two-layer region, we use the asymptotic solutions as matching conditions for our numerical solutions. That is, we calculate the asymptotic solution at $\hat{\Lambda} = 1 - \delta$ using the computed numerical solution of the single-layer region at $\hat{\Lambda} = 1$, where $\delta \ll 1$. We integrate the perturbation equations for the two-layer region numerically, backwards from $\hat{\Lambda} = 1 - \delta$ towards $\hat{\Lambda} = \Delta$, where $\Delta \ll 1$.

By performing an asymptotic analysis for a single-layer viscous gravity current, we find that the general solution for the perturbed dependent variables is of the form

$$X_1 \sim (c_1\hat{\Lambda}^{-k} + c_2\hat{\Lambda}^{k})w(\hat{\Lambda}) \tag{3.49}$$

as $\hat{\Lambda} \to 0$, where w is a function that is at most logarithmically singular at the origin and c_1 and c_2 are arbitrary constants. This reflects a singularity at the origin, which is strongest for large wavenumbers k. For the purpose of resolving this singularity for all k in our computations, we use the transformation

$$X_1(\hat{\Lambda}) \equiv \frac{1}{x}\bar{X}_1(x), \tag{3.50}$$

where $x = \hat{\Lambda}^k$, within the two-layer region, and solve for $\bar{X}_1$ numerically as a function of x.

As the problem is 2π-periodic in the azimuthal direction, only integer values of k are permitted. However, we interpolate for intermediate values of k for illustrative purposes in displaying the results.

Given a value of the wavenumber k, the system admits non-zero solutions for specific growth rates, or eigenvalues, σ. To find such solutions, we designed an algorithm by exploiting the linearity of the governing equations and boundary conditions. In particular, for a given wavenumber and set of parameter values, we set a guess for the growth rate and shoot backwards as described above. In doing so, we obtain two test solutions, denoted by s_1 and s_2, where s_1 is calculated by setting $\xi_{N1} = 1$ and $Q_{l1}|_{\hat{\Lambda}=L} = 0$ and s_2 is calculated by setting $\xi_{N1} = 0$ and $Q_{l1}|_{\hat{\Lambda}=L} = 1$. These two solutions are linearly independent and satisfy the perturbation equations and boundary conditions except for perhaps the source flux conditions at the origin. Owing to the linearity of the system, any linear combination of the two solutions is also a solution.

In order to quantify the departure from the source flux boundary conditions, we define a residual matrix

$$\boldsymbol{R} = \begin{bmatrix} Q_{l1,1} & Q_{l1,2} \\ Q_{u1,1} & Q_{u1,2} \end{bmatrix}, \tag{3.51}$$

where the i^{th} column measures the perturbed source flux at the origin corresponding to the solution s_i and $i = 1, 2$. If the initial guess for the value of the growth rate σ is correct, it is possible to obtain a linear combination of the two test solutions such that the source flux conditions at the origin are satisfied, i.e. $Q_{l1} = 0$ and $Q_{u1} = 0$. This is equivalent to $\det(\boldsymbol{R}) = 0$, and this particular linear combination is the desired solution to the perturbation equations and all boundary conditions, including the zero source flux boundary conditions. However, if the guessed value of the growth rate is incorrect, then $\det \boldsymbol{R} \neq 0$. That is, the growth rate is an admissible eigenvalue if and only if $\det(\boldsymbol{R}) = 0$. We, therefore, wish to find values of the growth rate σ for which $\det(\boldsymbol{R}) = 0$ to within a specified tolerance. In essence, this reduces to a one-dimensional root finding problem for σ.

To validate our numerical results, the computations were performed with specified absolute and relative tolerances controlling the solver accuracy (namely, AbsTol = 10^{-12} and RelTol = 10^{-12} in Mathematica's in-built solver *NDSolve*, and automatic absolute and relative tolerances in *FindRoot*). These tolerances were chosen sufficiently small to ensure convergence of the computed eigenvalues while avoiding excessive computational cost, and further tightening of the tolerances produced no discernible change in the results. Additional numerical tests were carried out by varying other numerical parameters, including the truncation of the computational domain, confirming that the results are independent of these choices.

At zero wavenumber, that is, for axisymmetric perturbations, there exists a mode corresponding to an exact similarity solution shifted in time. This mode is given by

$$F_1 = 0, \quad f_1 = 0, \quad \xi_{N1} = 1, \quad \sigma = -1, \quad k = 0.$$

This analytical solution is known *a priori* and provides a further test case for validating the numerical implementation.

We note that in order to assess stability, it suffices to consider the eigensolution that corre-

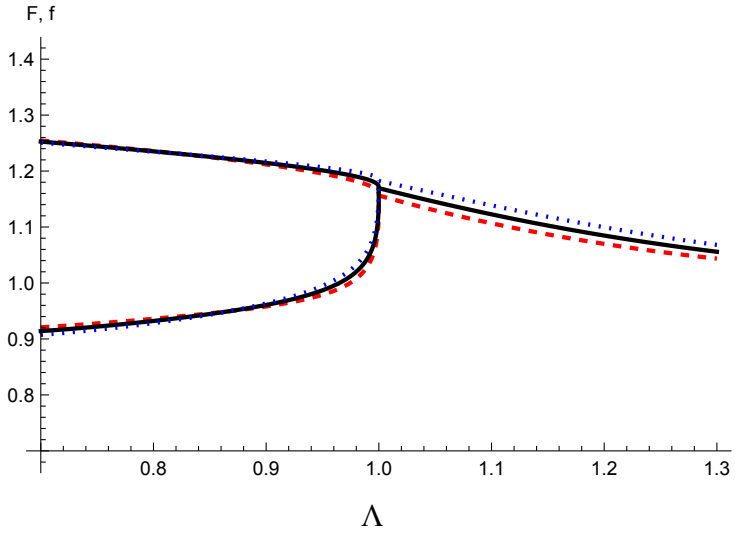

Figure 3.2: The unperturbed (solid) and perturbed (dashed and dotted) spatial profiles showing the shape of the nose when $k = 12$, $\mathcal{M} = 200$, $\mathcal{D} = 0.1$, $Q_u = 1$, and $Q_l = 0.2$. The perturbed profile shown as a dashed (dotted) curve corresponds to intrusions ahead of (behind) the nose of the base flow.

sponds to the largest growth rate, as this gives rise to the most unstable mode. We make sure that our computed solutions for σ are largest by manual inspection of plots of the determinant of $\boldsymbol{R}$ against the growth rate for a range of test cases. In the following section, we discuss results obtained by tracking the largest eigenvalue branch in the σ–k plane.

3.4 Discussion

In this section, we discuss the onset of instability and relevant characteristics in terms of the growth rates, interval of unstable wavenumbers and the critical wavenumber and how these vary across parameter space. In particular, we map out the behaviour of small disturbances to the base flow in terms of four key dimensionless quantities: the viscosity ratio $\mathcal{M}$, the density difference $\mathcal{D}$, the total source flux $Q_u + Q_l$, and the flux ratio Q_l/Q_u.

The spatial structure of the perturbation in an unstable configuration is depicted in Figure 3.2 in comparison to the unperturbed base flow. When the intruding layer is perturbed forwards (backwards), it thickens (thins) and protrudes downwards into (recedes upwards from) the lower layer and the lower layer thins (thickens) near the nose. As discussed further in §3.4.2, finger growth requires sufficient protrusion of an intruding less viscous fluid downwards into the more viscous underlying layer, rather than upwards into the less viscous air.

3.4.1 Thresholds of instability across parameter space

We find that the flow is unstable only for sufficiently large values of the viscosity ratio $\mathcal{M}$. That is, the intruding layer of viscous fluid needs to be of sufficiently small viscosity for the flow to

become unstable. This criterion is similar to what is necessary for the onset of Saffman-Taylor instabilities in porous media, which occur only when the viscosity of the intruding fluid is lower than that of the ambient fluid (Saffman & Taylor, 1958). Sufficiently large viscosity ratios are also necessary for the onset of fingering instabilities when the less viscous fluid intrudes from below a more viscous gravity current (Kowal & Worster, 2019*a*,*b*; Leung & Kowal, 2022*a*,*b*), and when it displaces the more viscous current completely (Kowal, 2021). Illustrative values of the viscosity ratio necessary for the onset of instability when the less viscous fluid intrudes from above a more viscous gravity current, as examined in this work, can be seen in Figure 3.3. In particular, Figure 3.3 displays the dispersion relation for the growth rate σ as a function of the wavenumber k, for illustrative parameter values and various values of the viscosity ratio $\mathcal{M}$. The growth rate is positive for a bounded interval of wavenumbers only when the viscosity ratio is large enough. That is, the flow is unstable for a bounded interval of wavenumbers only above a critical viscosity ratio. We also observe that high-wavenumber perturbations are suppressed due to the buoyancy force arising from the density difference between the two fluids. This is evidenced by comparison with Figure 5.8 of Dauck (2020), which shows the σ–k plane in the absence of a density difference. In that case, the growth rate appears to diverge, with $\sigma \to \infty$ as $k \to \infty$.

The interval of unstable wavenumbers is shown in Figure 3.4 as a function of the viscosity ratio $\mathcal{M}$, where it can be seen that the interval of unstable wavenumbers expands as the viscosity ratio increases. The boundary between the stable and unstable regions, shown in Figure 3.4, depicts the neutral viscosity ratio, defined as the value of the viscosity for which the growth rate is zero. The flow is unstable when the viscosity ratio is above the neutral viscosity ratio. The critical wavenumber k_c, defined as the wavenumber for which the growth rate is maximal, gradually increases with the wavenumber as depicted in Figure 3.4.

We find that the instability is most profound for low values of the density difference and that it is suppressed completely when the density difference is sufficiently large. This is illustrated in Figure 3.5, depicting an interval of wavenumbers for which the system is unstable below a critical value of the density difference. This interval expands and the critical wavenumber k_c increases as the density difference decreases, as shown in Figure 3.5. Figure 3.5 also illustrates that the instability is suppressed completely above a critical value of the density difference. This agrees with stability analyses of flows of thin films of viscous fluid intruding underneath another viscous fluid of various rheologies (Kowal & Worster, 2019*b*; Leung & Kowal, 2022*b*).

We condense information in the $(\mathcal{M}, \mathcal{D})$-parameter space further in a contour plot of the maximal growth rate $\sigma_{\max}$ versus the viscosity ratio and density difference, depicted in Figure 3.6. Maximal growth rates are largest for large viscosity ratios and small density differences, with viscosity ratios of the order of ten required for the onset of instability when the density difference is small. This contrasts with instabilities formed when a free-surface flow is penetrated from below by a less viscous fluid (Kowal & Worster, 2019*a*,*b*) and with classical Saffman-

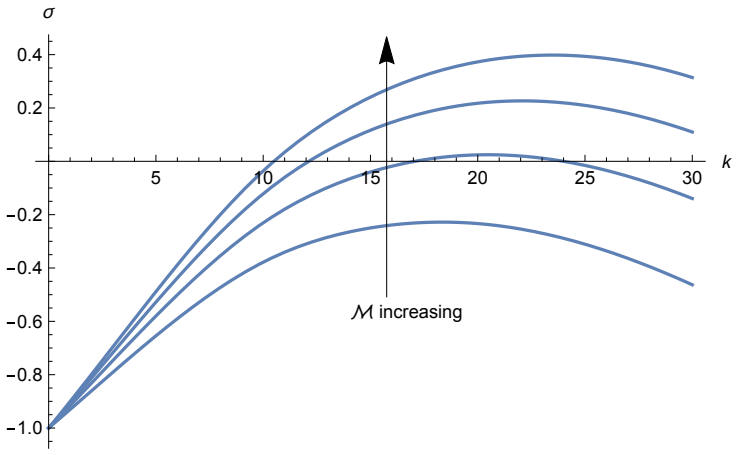

Figure 3.3: The growth rate versus the wavenumber for various viscosity ratios $\mathcal{M} = 20, 30, 40, 50$ when $\mathcal{D} = 0.05$, $Q_u = 1$, $Q_l = 1$.

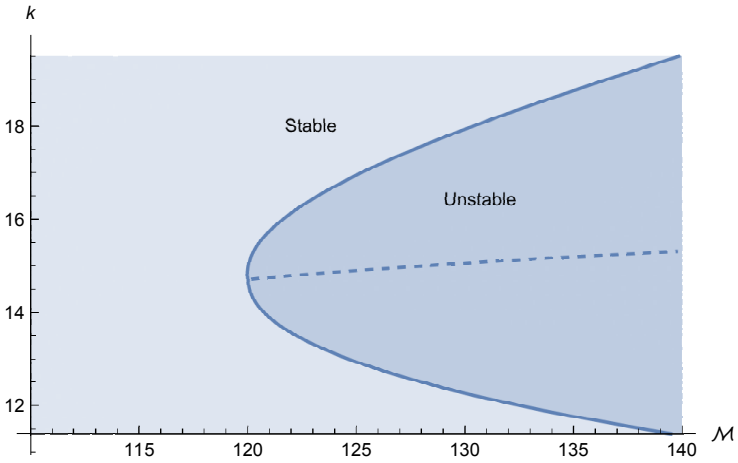

Figure 3.4: Neutral stability curve (solid) displaying the interval of unstable wavenumbers as a function of the viscosity ratio, also showing the critical wavenumber k_c (dashed), when $\mathcal{D} = 0.1, Q_u = 1$, and $Q_l = 1$. The flow is unstable (stable) for large (small) viscosity ratios.

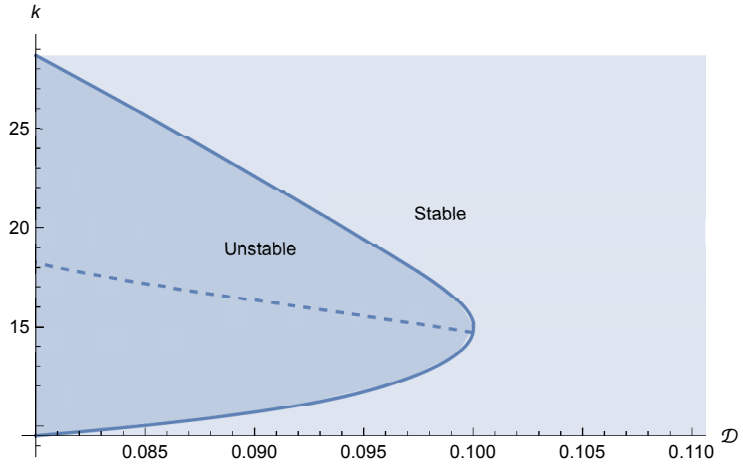

Figure 3.5: Neutral stability curve (solid) displaying the interval of unstable wavenumbers as a function of the density difference, also showing the critical wavenumber k_c (dashed), when $\mathcal{M} = 120, Q_u = 1$, and $Q_l = 1$. The flow is unstable (stable) for small (large) density differences.

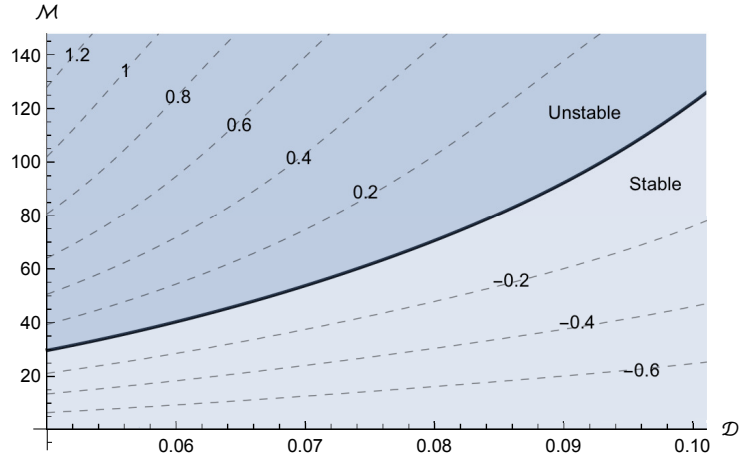

Figure 3.6: Contour plot of the maximal growth rate $\sigma_{\max}$ versus the viscosity ratio $\mathcal{M}$ and density difference $\mathcal{D}$, with the neutral stability curve ($\sigma_{\max} = 0$) displayed as a thick solid curve. The remaining parameter values are $Q_u = 1$, and $Q_l = 1$. The flow is unstable for high viscosity ratios and low density differences.

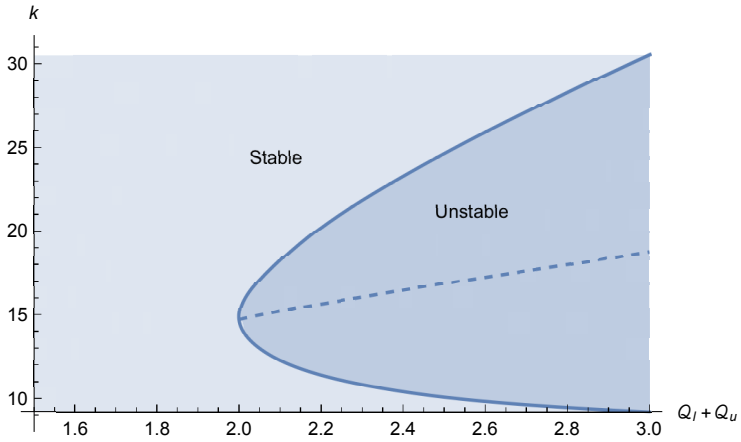

Figure 3.7: Neutral stability curve (solid) displaying the interval of unstable wavenumbers as a function of the total source flux, also showing the critical wavenumber k_c (dashed), when $\mathcal{D} = 0.1$, $\mathcal{M} = 120$, and $Q_l/Q_u = 1$. The flow is unstable (stable) for large (small) source fluxes.

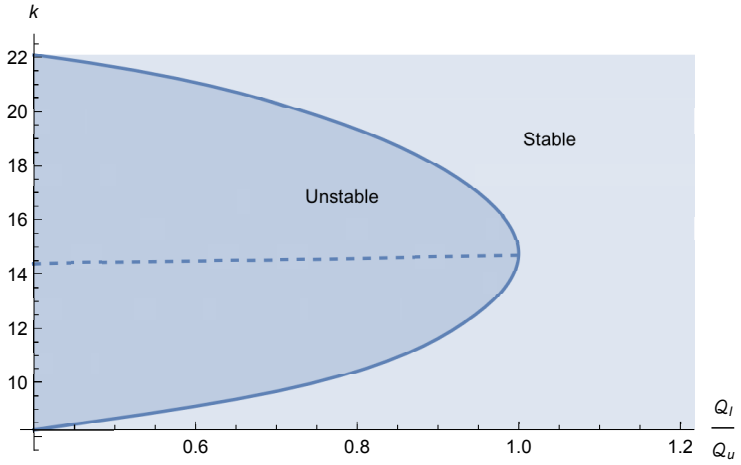

Figure 3.8: Neutral stability curve (solid) displaying the neutral flux ratio Q_l/Q_u as a function of the wavenumber, also showing the critical wavenumber k_c (dashed), when $\mathcal{D} = 0.1$, $\mathcal{M} = 120$, and $Q_l + Q_u = 1$. The flow is unstable for flux ratios above this neutral stability curve.

Taylor instabilities in a Hele-Shaw cell (Saffman & Taylor, 1958), for which the threshold of instability is of order unity in the viscosity ratio. We discuss why this is to be expected on physical grounds in §3.4.2.

We find that the instability is suppressed completely for a sufficiently small total flux $Q_l + Q_u$ and sufficiently large flux ratio Q_l/Q_u, as depicted in figures 3.7 and 3.8. The interval of unstable wavenumbers expands as the total source flux increases and the flux ratio decreases. The critical wavenumber increases with the total source flux and remains approximately constant with respect to the flux ratio. We can therefore expect to see an increasing number of fingers when the total source flux increases, which is consistent with recent experiments in which the intruding fluid is supplied from below (Kumar *et al.*, 2021).

We condense information further in a contour plot of the maximal growth rate $\sigma_{\max}$ versus the total flux and flux ratio, shown in Figure 3.9. As seen in Figure 3.9, growth rates are largest when the total flux is large and a sufficiently large total flux (of order unity) is required for the onset of instability. Equivalently, the onset of instability requires the flux of the upper layer to be sufficiently large relative to that of the lower layer. This is in line with the experiments of Lister & Kerr (1989), in which a low viscosity fluid intrudes at the interface between two other fluids and no instabilities were observed, save for small-scale frontal patterning that the authors attribute to contamination of the fluid surface by dust. These experiments were carried out for dimensionless fluxes in the range 8.7×10^{-6}–5.3×10^{-5}, which is much less than the threshold (of order unity) required for instability. The threshold is also consistent with the experiments of Dauck (2020), for which the dimensionless flux reached up to approximately 160 and instabilities were observed.

The stability thresholds discussed in this section are summarised in the most condensed contour plot shown in Figure 3.10, displaying the critical total flux required for the onset of instability in $(\mathcal{D}, \mathcal{M})$ space for various values of the flux ratio. Values of the critical viscosity ratio and critical density difference required for the onset of instability can be read off from Figure 3.10. Alternatively, Figure 3.10 can be interpreted as a plot of the critical viscosity ratio versus the density difference for various values of the total flux and flux ratio. The higher the total flux, the lower the viscosity ratio required for the onset of instability, and the larger the interval of density differences for which instabilities appear.

3.4.2 Mechanism of instability and suppression

To understand the mechanism of instability physically, it is instructive to compare to classical viscous fingering in porous-media/Hele-Shaw cells. The mechanisms of instability are similar in that there is less flow resistance along the fingers of less viscous fluid than in the gaps between them filled with more viscous fluid, thus resulting in the fingers growing (when the intruding fluid is less viscous than the ambient). However, in the free-surface case examined here, the intruding fluid is also advancing into atmosphere (which is less viscous, so the viscosity con-

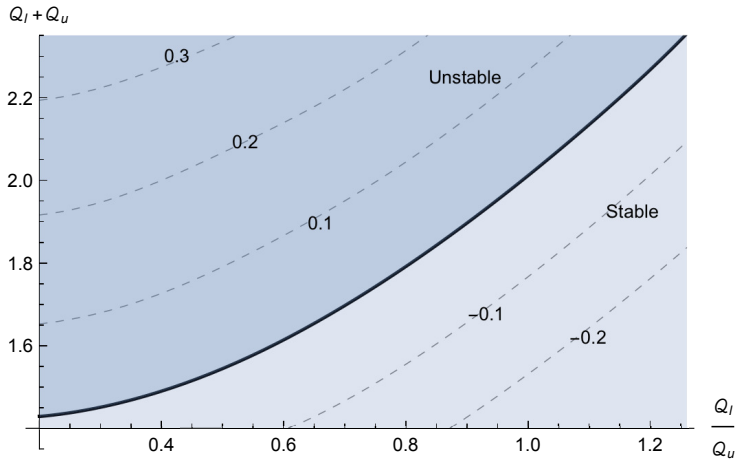

Figure 3.9: Contour plot of the maximal growth rate $\sigma_{\max}$ versus the flux ratio Q_l/Q_u and total flux $Q_l + Q_u$, with the neutral stability curve ($\sigma_{\max} = 0$) displayed as a thick solid curve. The remaining parameter values are $\mathcal{M} = 120$, and $\mathcal{D} = 0.1$. The flow is unstable when the total flux is large and flux ratio is small.

trast is stabilising), so finger growth is reliant on the intruding fingers displacing the lubricating liquid "more" than displacing the atmosphere. In other words, finger growth requires the density difference $\mathcal{D}$ to be sufficiently small (as seen in Figure 3.5) and the upper-layer flux Q_u to be sufficiently large relative to the lower-layer flux Q_l and relative to unity (as seen in figures 3.7–3.9) that the fingers can sink down into rather than just riding on top of the lubricating layer.

In contrast, when the less viscous fluid intrudes beneath another thin film of viscous fluid (the setup of Kowal & Worster (2019*a*,*b*)), it is not stabilised by its advance into a less viscous atmosphere and so the instability thresholds are lower than reported here. In particular, the critical viscosity ratio required for the onset of instability in the setup of Kowal & Worster (2019*a*,*b*) is of order unity when the intruding layer is supplied from below, which is one to two orders of magnitude smaller than when the less viscous fluid intrudes from above as in the current work. However, the general trends in the stability thresholds are qualitatively similar as the parameters vary. For example, for both systems, there is a critical density difference above which the instabilities are compressed, with the interval of unstable wavenumbers widening as the density difference decreases. The critical density difference is of order unity (versus one tenth) when the less viscous fluid intrudes from below (versus above).

To explore the mechanism of suppression further, it is also instructive to focus on contributions that are significant for large density differences. Nonzero density differences between the two layers of viscous fluid give rise to additional buoyancy forces within the lower layer near the front of the intruding fluid. These are associated with the gravitational spreading of the underlying layer under its own weight, dragging the upper layer along with it. As gradients of the lower-layer thickness are positive near the front when the density difference is nonzero, the contributions to the flow velocity, arising from the spreading of the lower layer under its own weight, are negative within the underlying layer. This, in turn, induces an inwards contribution

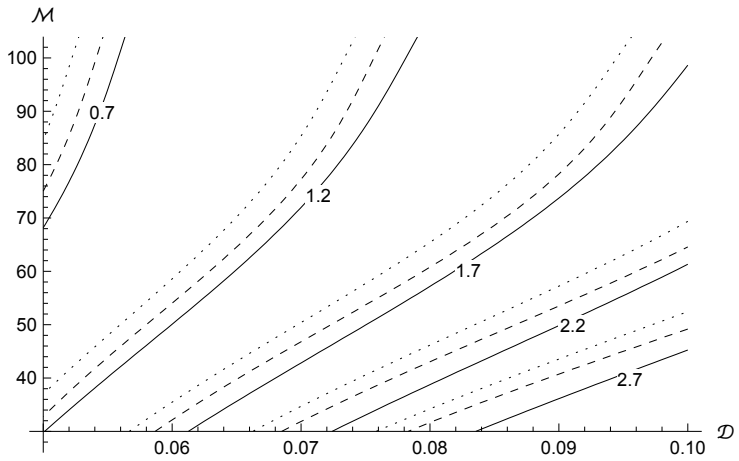

Figure 3.10: Contour plot of the critical total flux $Q_l + Q_u$ required for the onset of instability in $(\mathcal{D}, \mathcal{M})$) space when Q_l/Q_u=0.4 (solid curves), 0.5 (dashed curves) and 0.6 (dotted curves).

to the flow, seen most clearly in the velocity profiles of Figure 5 of Yang *et al.* (2024). That is, in what would have been an unstable configuration, this contribution involves more viscous fluid intruding (inwards) into less viscous fluid, which is stabilising.

Similar buoyancy forces stabilise the flow of single-layer viscous gravity currents, where a viscous fluid intrudes into air (less viscous) – a stable viscosity contrast (Mathunjwa & Hogg, 2006*a*). Small perturbations to single-layer viscous gravity currents, which are driven by buoyancy forces alone, have been found to decay and the flow has been found to approach a similarity solution at late times (Mathunjwa & Hogg, 2006*a*; Ball & Huppert, 2019). For two-layer flows, these buoyancy forces contribute to the flow only when the densities of the two viscous fluids are unequal. When the density difference increases, so does the effect of these buoyancy forces, especially near the front, where they are most profound as depicted in Figure 5 of Yang *et al.* (2024). As the instability is a frontal instability, the dynamics near the front, and particularly the effect of these buoyancy forces, are what determines the onset of instability, and hence it is natural to expect these forces to have a stabilising effect when the density difference is sufficiently large, as seen in Figure 3.5.

3.5 Conclusions

In this work, we have demonstrated that a free-surface flow consisting of a thin film of viscous fluid intruding over another layer of fluid of dissimilar viscosity and density is prone to a new type fingering instability, termed the non-porous viscous fingering instability. This type of instability is most closely related to Saffman-Taylor viscous fingering in a porous medium or a Hele-Shaw cell, but this time without a porous medium or Hele-Shaw cell present. The similarity between these two types of instability is that a viscosity contrast between two fluids is needed for both instabilities to occur. The difference between them is that the jump in pressure

gradient driving the instabilities is hydrostatic for the former and dynamic for the latter form of instability.

We also point out features distinguishing the non-porous viscous fingering instability from other frontal instabilities, including the fingering of a driven spreading film and thermoviscous fingering. We found that a free-surface flow of a low-viscosity fluid is more prone to instability when intruding into a high-viscosity fluid from below (as in Kowal & Worster, 2019*a*,*b*) than from above (as in the present paper). Intuitively, this is because the less viscous fluid also displaces the atmosphere (an even less viscous fluid) in the latter scenario, which is stabilising.

We have also examined the stabilising influence of buoyancy forces, which form near the nose of a thin film of viscous fluid as it intrudes into another viscous fluid of different density and viscosity. These buoyancy forces are greatest near the front of the intruding layer and feature as the only physical mechanism driving the flow of single-layer viscous gravity currents, for example. Such buoyancy forces have been shown to be stabilising for single-layer flows (Grundy & McLaughlin, 1982; Mathunjwa & Hogg, 2006*a*) and for two-phase flows, when the intruding layer is supplied from below (Kowal & Worster, 2019*a*,*b*) or when it completely displaces the ambient layer (Kowal, 2021).

We found that a sufficiently large viscosity ratio is required in order for the instability to occur, and that the instability is suppressed completely for large enough density differences between the two layers. For large enough density differences, driving buoyancy forces associated with the gravitational spreading of the lubricating layer under its own weight become more pronounced, and stabilise the flow completely. For lower density differences, for which the system is unstable, this mechanism provides for wavelength selection, stabilising the flow for large wavenumbers in contrast to intermediate wavenumbers. This indicates that the hydrodynamic interactions of the two layers of viscous fluid alone suffice in stabilising the flow for large wavenumbers, giving rise to wavelength selection. This contrasts with classical Saffman-Taylor viscous fingering, which is instead stabilised by other mechanisms, such as the effects of surface tension, or fluid mixing, for example. Such effects, however, may further stabilise the flow considered in this work, likely leading to smaller growth rates for large wavenumbers and smaller critical wavenumbers.

We also found evidence of the role of the source flux in the onset of these fingering instabilities. In particular, the flow is unstable only when the source flux of the upper layer is large enough relative to that of the lower layer, which is consistent with available experimental observations when the intruding fluid is supplied from below, for various rheologies, and from above.

Our observations may shed light on the appearance and possible suppression mechanisms of similar fingering instabilities found in nature and industry at various length and time scales, modulo the influence of secondary effects such as surface tension, or fluid mixing, for instance. Examples include drug-mucus interactions in nasal drug/vaccine delivery, the manufacture of

patterned substrates and the interaction of dissimilar lava flows, for example.

Chapter 4

Dynamics and stability of a thin film of fluid spreading over a lubricated inclined plane

4.1 Introduction

Having investigated the dynamics and instability of axisymmetric viscous gravity currents on a horizontal plane, we now extend our analysis to consider the behaviour of such currents on an inclined substrate. Introducing a slope alters the force balance governing the flow: while on a horizontal plane the motion is driven purely by the hydrostatic pressure gradient owing to gravity acting vertically, an inclined plane introduces a component of gravity acting tangentially to the substrate. We find this additional driving force promotes the flow instabilities examined in Chapter 3.

While similar in setup, we note the difference between non-porous viscous fingering of a thin film flowing down a lubricated plane, considered in this chapter, and fingering of a driven spreading film down a non-lubricated substrate (Huppert, 1982*a*; Troian *et al.*, 1989). While the former requires a viscosity contrast for instabilities to occur and is independent of surface tension, for the latter, there is no viscosity contrast and surface tension is key. The experimental study of Huppert (1982*a*) demonstrated that a fixed-volume single-layer viscous gravity current flowing down a slope can break into capillary-controlled rivulets at large times, exhibiting either finger-like or triangular sawtooth patterns. Building on this, the stability analysis of Troian *et al.* (1989) demonstrated that perturbations near the capillary ridge at the intruding front can grow and evolve into transverse fingering. In the latter analysis, the advancing front was pre-wetted by a precursor film to resolve the moving contact line problem whilst effectively capturing the influence of surface tension. Their analysis emphasized the key role of the interaction between surface tension and viscous forces in selecting the characteristic wavelength of the instability.

We also note the difference between the two-layer fingering instabilities examined in this

chapter, which are frontal instabilities, and instabilities owing to viscosity stratification (Yih, 1967; Balmforth *et al.*, 2003), which are longitudinal instabilities. First examined for two superposed layers of Newtonian viscous fluids (Yih, 1967) and later examined for power-law fluids (Balmforth *et al.*, 2003), it was shown that a that viscosity contrast can drive nonlinear interfacial wave formation, even in the absence of inertia, i.e., at low Reynolds numbers. These instabilities are purely longitudinal, with waves forming at the interface between the two layers in the direction of the flow. In contrast, the instabilities examined in this chapter are frontal instabilities, for which protrusions grow along the transverse direction, orthogonal to the flow. The instabilities considered in this chapter extend the analysis of (Kowal, 2021), in which two fluids of equal density interact through one fluid intruding into and displacing the other. This study revealed the emergence of transverse interfacial patterns and identified conditions under which fingering instabilities may arise.

The focus of this chapter is to investigate the instability that arises at the nose of an intruding fluid advancing over another fluid layer flowing down an inclined plane. The structure of the chapter is as follows. First, we present the governing equations describing the dynamics of the two-layer flow down an inclined plane. The equations are equivalent to those of Shah *et al.* (2021) except for the difference in setup: here, we focus on flows for which the intruding layer is supplied from above while Shah *et al.* (2021) considered flows for which the intruding fluid is supplied from below. Second, we explore the existence and properties of travelling wave solutions, which provide a tractable framework for performing a linear stability analysis and offer insight into the behavior of more general, time-evolving flows. Third, we carry out a linear stability analysis of these travelling wave solutions to identify the conditions under which the interface becomes unstable and to characterize the nature of the resulting instabilities across parameter space.

4.2 Theoretical Development

Consider the flow of two thin layers of incompressible, Newtonian viscous fluid with homogeneous viscosities μ_u and μ_l, and densities ρ_u and ρ_l flowing down an inclined plane as illustrated in Figure 4.1. Here, the subscripts $_u$ and $_l$ correspond to quantities characterising the upper and lower layers, respectively.

The rigid surface inclined at an angle α is initially coated with a uniform depth h_s of the lower-layer fluid. The total and lower-layer thicknesses are represented by $H(x,y,t)$ and $h(x,y,t)$, respectively.

The two fluids are supplied from the upstream far field ($x \to -\infty$). The upper-layer fluid occupies the upstream region up to the intrusion front (nose), denoted by $x = x_N(y,t)$, while the lower-layer fluid occupies the whole domain. The intrusion front is a moving boundary dividing the domain into two regions: a two-layer region, $-\infty < x < x_N(t)$, including both viscous fluids,

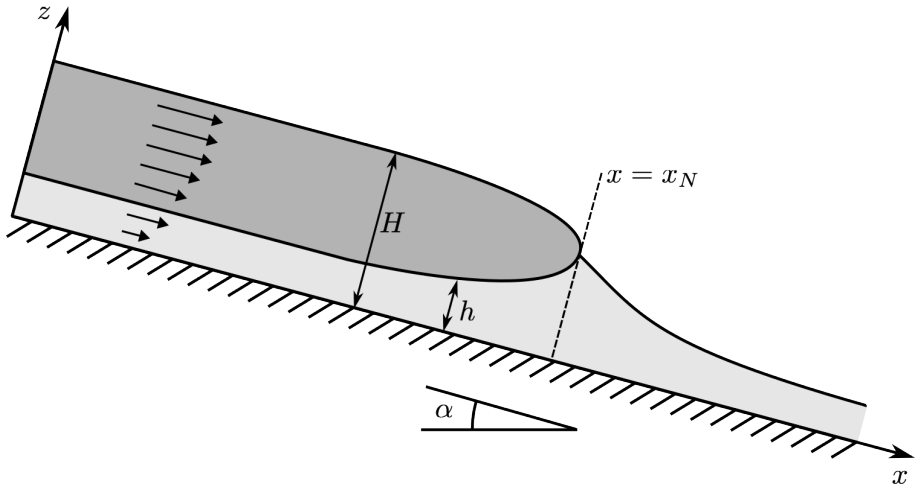

Figure 4.1: Schematic of a thin film of viscous fluid spreading over a lubricated inclined surface.

and a single-layer region, $x \geq x_N(t)$, involving only the lower-layer fluid.

In developing a theoretical framework, we neglect the effects of inertia, resulting in a balance between viscous and buoyancy forces. Additionally, we assume that the effects of surface tension and mixing at the fluid interfaces are negligible (Huppert, 1982*a*). We also assume that the horizontal length scale is much greater than the vertical length scale, and vertical shear provides the primary resistance to flow. With these assumptions, we apply lubrication theory and obtain the momentum equations

$$\mathbf{0} = -\nabla p_i + \rho_i \boldsymbol{g} + \mu_i \frac{\partial^2 \boldsymbol{u}_i}{\partial z^2}, \tag{4.1}$$

where $p_i = p_i(x, y, z, t)$ is the pressure, $\boldsymbol{u}_i = \boldsymbol{u}_i(x, y, z, t)$ is the velocity, the subscript $i = u, l$ denotes the upper and lower layers, respectively, $\boldsymbol{g} = g(\sin\alpha \mathbf{e}_x - \cos\alpha \mathbf{e}_z)$ is the acceleration owing to gravity, and $\mathbf{e}_x$ and $\mathbf{e}_z$ are the unit basis vectors in the x- and z-directions, respectively.

The two-layer region

Assuming that vertical shear stresses provide the primary resistance to the flow, the pressure within the two layers is hydrostatic so that

$$p_u = \cos\alpha \rho_u g(H - z), \tag{4.2}$$

$$p_l = \cos\alpha [\rho_u g(H - h) + \rho_l g(h - z)]. \tag{4.3}$$

We assume the upper layer to be stress-free at its upper surface, so that

$$\mu_u \frac{\partial \boldsymbol{u}_u}{\partial z} = 0 \quad \text{at} \quad z = H. \tag{4.4}$$

Furthermore, we assume continuity of velocity and shear stress at the interface between the upper and lower fluids, leading to

$$\boldsymbol{u}_l = \boldsymbol{u}_u \qquad \text{at} \quad z = h, \tag{4.5}$$

$$\mu_l \frac{\partial \boldsymbol{u}_l}{\partial z} = \mu_u \frac{\partial \boldsymbol{u}_u}{\partial z} \quad \text{at} \quad z = h. \tag{4.6}$$

Additionally, we assume the no-slip condition at the inclined substrate,

$$\boldsymbol{u}_l = 0 \quad \text{at} \quad z = 0. \tag{4.7}$$

By solving the momentum equations (4.1) for the velocity profile under boundary conditions (4.4)–(4.7) and integrating across the depth of each layer, we derive the following expressions for the depth-integrated fluxes of upper- and lower-layer fluids, per unit width,

$$\boldsymbol{q}_u = -\frac{\rho_l g \cos\alpha}{\mu_l(1+\mathcal{D})}\left[\frac{1}{3}\mathcal{M}\left(\nabla H - \tan\alpha \boldsymbol{e_x}\right)(H-h)^3 + \right.$$
$$\left.\frac{1}{2}\left(\mathcal{D}\nabla h + \nabla H - (1+\mathcal{D})\tan\alpha \boldsymbol{e_x}\right)(H-h)h^2 + \left(\nabla H - \tan\alpha \boldsymbol{e_x}\right)(H-h)^2 h\right], \tag{4.8}$$

$$\boldsymbol{q}_l = -\frac{\rho_l g \cos\alpha}{\mu_l(1+\mathcal{D})}\left[\frac{1}{3}\left(\mathcal{D}\nabla h + \nabla H - (1+\mathcal{D})\tan\alpha \boldsymbol{e_x}\right)h^3 + \frac{1}{2}\left(\nabla H - \tan\alpha \boldsymbol{e_x}\right)(H-h)h^2\right], \tag{4.9}$$

where $\nabla = \partial/\partial x \boldsymbol{e_x} + \partial/\partial y \boldsymbol{e_y}$. Equations (4.8) and (4.9) for the fluxes differ from the equivalent equations (2.10) and (2.11) for the flow over a horizontal substrate, derived in Chapter 2, in the $\tan\alpha \boldsymbol{e}_x$ terms, with equivalence between them when $\alpha = 0$. These expressions are equivalent to those of Shah *et al.* (2021).

The dimensionless parameters

$$\mathcal{M} = \frac{\mu_l}{\mu_u}, \tag{4.10}$$

$$\mathcal{D} = \frac{\rho_l - \rho_u}{\rho_u}, \tag{4.11}$$

define the viscosity ratio and relative density difference, respectively, as in Chapters 2–3. The evolution of the upper surface and the interface between the two fluids is determined by the mass conservation equations

$$\frac{\partial(H-h)}{\partial t} + \nabla \cdot \boldsymbol{q}_u = 0, \tag{4.12}$$

$$\frac{\partial h}{\partial t} + \nabla \cdot \boldsymbol{q}_l = 0, \tag{4.13}$$

for the upper and lower layers, respectively. These equations, alongside equations (4.8)–(4.9) for

the depth-integrated fluxes, determine the evolution of the free surfaces in the two-layer region.

The single-layer region

To obtain the flux of fluid in the single-layer region, we set $H = h$ in equation (4.9), indicating that there is no upper-layer fluid, yielding

$$\boldsymbol{q}_l = -\frac{\rho_l g}{\mu_l}\frac{1}{3}\left(\nabla h - \tan\alpha \boldsymbol{e_x}\right) h^3, \tag{4.14}$$

in line with Huppert (1982*a*). In addition, the evolution of the free surface is governed by the usual mass conservation equation

$$\frac{\partial h}{\partial t} + \nabla \cdot \boldsymbol{q}_l = 0. \tag{4.15}$$

This equation determines how the free surface changes over time in the single-layer region.

Boundary conditions

To simplify the system, we assume the free surfaces H and h do not vary in the y-direction, so that $\boldsymbol{q}_u = q_u \boldsymbol{e_x}$ and $\boldsymbol{q}_l = q_l \boldsymbol{e_x}$. Below, we outline the corresponding boundary conditions and matching conditions across the intrusion front.

At the upstream far field, we assume that both the upper and lower layers approach a uniform thickness, so that

$$\lim_{x\to-\infty} H = H_\infty, \tag{4.16}$$

$$\lim_{x\to-\infty} h = h_\infty. \tag{4.17}$$

These are equivalent to

$$\lim_{x\to-\infty} q_u = q_{u\infty}, \tag{4.18}$$

$$\lim_{x\to-\infty} q_l = q_{l\infty}, \tag{4.19}$$

where

$$q_{u\infty} = \frac{\rho_l g \sin\alpha}{\mu_l(1+\mathcal{D})}\left[\frac{1}{3}\mathcal{M}\left(H_\infty - h_\infty\right)^3 + \frac{1}{2}\left(1+\mathcal{D}\right)\left(H_\infty - h_\infty\right)h_\infty^2 + \left(H_\infty - h_\infty\right)^2 h_\infty\right], \tag{4.20}$$

$$q_{l\infty} = \frac{\rho_l g \sin\alpha}{\mu_l(1+\mathcal{D})}\left[\frac{1}{3}(1+\mathcal{D})h_\infty^3 + \frac{1}{2}(H_\infty - h_\infty)h_\infty^2\right]. \tag{4.21}$$

The thickness and the flux of the lower layer are continuous across the intrusion front $x =$

$x_N(y,t)$, so that

$$[h]_-^+ = 0 \quad \text{at} \quad x = x_N, \tag{4.22}$$

$$[q_l]_-^+ = 0 \quad \text{at} \quad x = x_N. \tag{4.23}$$

Furthermore, at the front, the flux of the upper layer vanishes, so that

$$q_u = 0 \quad \text{at} \quad x = x_N. \tag{4.24}$$

The front evolves kinematically, leading to the following evolution equation for the frontal position

$$\frac{\partial x_N}{\partial t} = \lim_{x \to x_N^-} \left[\frac{q_u}{H-h} - \frac{\boldsymbol{q}_u \cdot \boldsymbol{e}_y}{H-h} \frac{\partial x_n}{\partial y} \right]. \tag{4.25}$$

Lastly, in the downstream far field, we approach a uniform thickness h_s, so that:

$$\lim_{x \to \infty} h = h_s. \tag{4.26}$$

The boundary conditions and matching conditions detailed in this section close the problem for the evolution of the two liquid layers.

4.3 Nondimensionalization

We proceed by focusing on two-dimensional flows, in which variations in y are negligible. To identify the key dimensionless parameters governing the flow, we non-dimensionalize the system using the intrinsic length, height, flux and time scales

$$\mathcal{X} = \frac{h_s}{\tan\alpha}, \tag{4.27}$$

$$\mathcal{H} = h_s, \tag{4.28}$$

$$\mathcal{Q} = \frac{\rho_l g \cos\alpha}{\mu_l} \frac{1}{3} \frac{\mathcal{H}^4}{\mathcal{X}}, \tag{4.29}$$

$$\mathcal{T} = \frac{\mathcal{X}\mathcal{H}}{\mathcal{Q}}, \tag{4.30}$$

respectively. We define non-dimensional variables by

$$\hat{x} = \frac{x}{\mathcal{X}}, \tag{4.31}$$

$$[\hat{H}, \hat{h}] = \frac{[H, h]}{\mathcal{H}}, \tag{4.32}$$

$$[\hat{q}_u, \hat{q}_l] = \frac{[q_u, q_l]}{\mathcal{Q}}, \tag{4.33}$$

$$\hat{t} = \frac{t}{\mathcal{T}}. \tag{4.34}$$

Upon dropping hats, we obtain the dimensionless system

$$\frac{\partial (H-h)}{\partial t} + \frac{\partial q_u}{\partial x} = 0, \tag{4.35}$$

$$\frac{\partial h}{\partial t} + \frac{\partial q_l}{\partial x} = 0, \tag{4.36}$$

where

$$q_u = -\frac{1}{1+\mathcal{D}}\left[\mathcal{M}\left(\frac{\partial H}{\partial x} - 1\right)(H-h)^3 + \right.$$
$$\left. \frac{3}{2}\left(\mathcal{D}\frac{\partial h}{\partial x} + \frac{\partial H}{\partial x} - (1+\mathcal{D})\right)(H-h)h^2 + 3\left(\frac{\partial H}{\partial x} - 1\right)(H-h)^2 h\right], \tag{4.37}$$

$$q_l = -\frac{1}{1+\mathcal{D}}\left[\left(\mathcal{D}\frac{\partial h}{\partial x} + \frac{\partial H}{\partial x} - (1+\mathcal{D})\right)h^3 + \frac{3}{2}\left(\frac{\partial H}{\partial x} - 1\right)(H-h)h^2\right], \tag{4.38}$$

upstream of the intrusion front, $-\infty < x < x_N$, and

$$q_u = 0, \tag{4.39}$$

$$q_l = -\left(\frac{\partial h}{\partial x} - 1\right)h^3. \tag{4.40}$$

downstream of the intrusion front, $x_N \leq x < \infty$.

The boundary conditions and matching conditions simplify to

$$H \to H_\infty, \quad h \to h_\infty, \quad \text{as} \quad x \to -\infty, \tag{4.41}$$

$$[h]^+_- = 0, \quad [q_l]^+_- = 0, \quad q_u = 0, \quad \text{at} \quad x = x_N, \tag{4.42}$$

$$\frac{dx_N}{dt} \to \frac{q_u}{H-h} \quad \text{as} \quad x \to x_N^-, \tag{4.43}$$

$$h \to 1 \quad \text{as} \quad x \to \infty. \tag{4.44}$$

4.4 Numerical scheme and results

We obtain the numerical solution of the system (4.35)–(4.44) by discretizing the spatial derivative using the finite difference method on uniform grids. Specifically, second-order central difference schemes are employed at interior grid points, while fifth-order one-sided schemes are used at the boundaries. Following this spatial discretisation, the boundary conditions are imposed by enforcing the prescribed boundary fluxes or thicknesses, then we proceed to solve for the evolution of the free surfaces using the ODE solver *ode15s* in MATLAB. Numerical experiments suggest that the long-time behaviour of the PDE system is insensitive to the initial condition. This is evidenced, for example, in Figure 4.2(b) presented later, where a sharp transient response is observed at very early times ($t \ll 1$), before the solution relaxes towards its long-time dynamics. Consequently, the numerical solver is initialised using an arbitrary smooth thickness profile.

The principal difficulty in the numerical integration arises from the singular behaviour in the two-layer region ahead of the intruding front x_N, where the spatial derivatives of the layer thicknesses, $\partial H/\partial x$ and $\partial h/\partial x$, diverge, in a manner analogous to the horizontal substrate case discussed in §2. To resolve this issue, a change of spatial variables is introduced in the PDE solver, we define new variables $\tilde{t} = t$ and $\tilde{x} = (x_N - x)^a$, with $a > 0$, and rewrite all dependent variables in the two-layer region as functions of $(\tilde{x}, \tilde{t})$ instead of (x, t).

Based on the asymptotic analysis for the horizontal substrate case presented in §2, a natural choice is $a = 1/2$. Numerical experiments confirm that this choice is effective in regularising the solution near the front. Under this transformation, the layer thicknesses ahead of the nose behave approximately linearly in $\tilde{x}$, and the previously divergent spatial derivatives are rendered finite.

To ensure a finite computational domain, we replace $-\infty$ in the upstream far-field boundary condition (4.41) with a moving boundary $x_1(t)$, and ∞ in the downstream condition (4.44) with $x_2(t)$. The speeds of these pseudo-infinity boundaries, $\mathrm{d}x_1/\mathrm{d}t$ and $\mathrm{d}x_2/\mathrm{d}t$, are chosen to be moderate so that $x_1(t)$ and $x_2(t)$ remain sufficiently close to the nose position $x_N(t)$, ensuring that the computational grid does not become excessively large over time. The initial nose position $x_N(0)$ is selected to lie well within the domain bounded by $x_1(0)$ and $x_2(0)$. The system is initialized with a sufficiently smooth thickness profile.

The robustness of the numerical solutions was verified by varying the numerical parameters, including, for example, the grid size, the position and speed of the moving boundaries, the tolerances of *ode15s*, and confirming that the results are insensitive to these choices.

The numerical solution for an illustrative set of parameters is depicted in Figure 4.2. Figure 4.2(a) shows the evolution of the thickness profile near the nose over the time interval $1 \le t \le 10$. This interval is chosen to be sufficiently away from 0 to eliminate transient effects from the initial conditions, as our primary interest lies in the long-term behaviour of the PDE. We observe a square-root singularity at the nose, consistent with the findings of §2. In fact, the

(*a*)

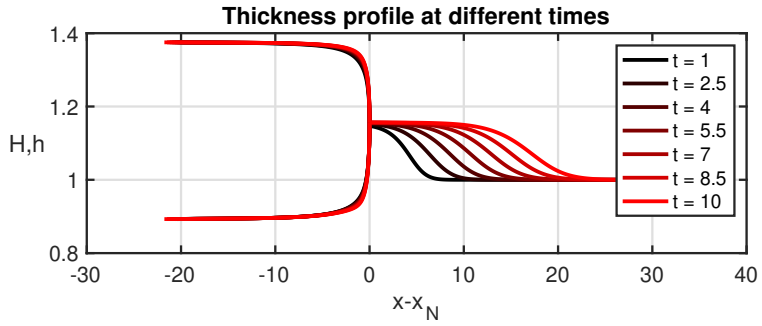

(*b*)

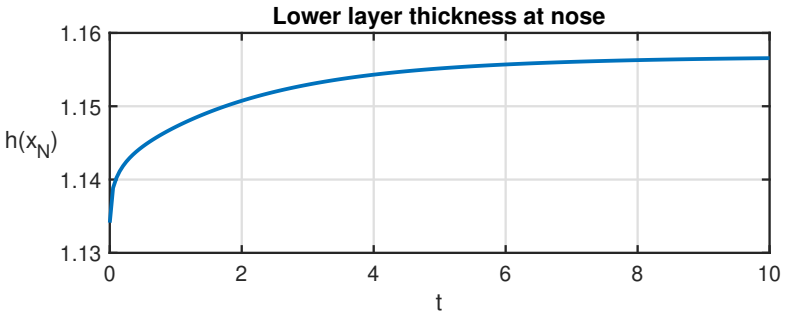

(*c*)

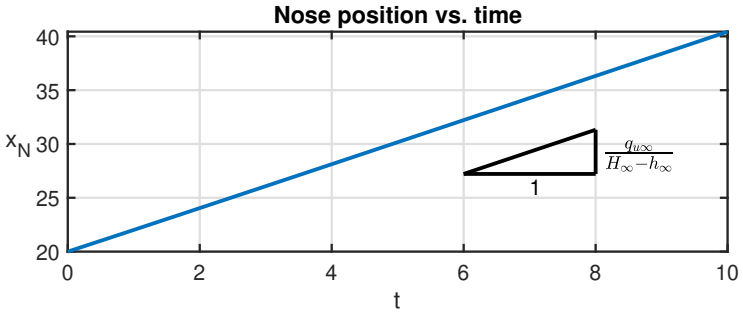

Figure 4.2: The numerical solutions when $\mathcal{M} = 2$, $\mathcal{D} = 1$, $q_{u\infty} = 1$ and $q_{l\infty} = 1$. (a) The thickness profiles for the specified time interval $1 \leq t \leq 10$. (b) The lower-layer thickness at the nose versus time. (c) The nose position versus time.

asymptotic analysis is identical to that presented in Appendix A. Figure 4.2(b) demonstrates that the lower-layer thickness at the nose approaches a constant value, while Figure 4.2(c) indicates that the nose propagates at a constant speed, approximately given by $q_{u\infty}/(H_\infty - h_\infty)$. Although it is not conclusive from Figure 4.2(a) whether the waveform converges to a fixed shape, the observations in Figures 4.2(b) and 4.2(c) provide strong evidence that the system may admit a travelling-wave solutions. This prompted us to search for travelling-wave solutions around the intrusion front x_N.

4.5 Travelling-wave solutions

To search for a travelling-wave solution with constant velocity v, we recast the equations in the frame of the front by changing variables $\xi = x - x_N(t)$, where $dx_N/dt = v$. Substituting this transformation into (4.35)–(4.40) yields

$$-v(H-h)' + q_u' = 0, \tag{4.45}$$

$$-vh' + q_l' = 0, \tag{4.46}$$

where $'$ represents $d/d\xi$ and the fluxes are given by

$$q_u = -\frac{1}{1+\mathcal{D}}\left[\mathcal{M}\,(H'-1)\,(H-h)^3 + \frac{3}{2}\,(\mathcal{D}h' + H' - (1+\mathcal{D}))\,(H-h)h^2 + 3(H'-1)(H-h)^2 h\right], \tag{4.47}$$

$$q_l = -\frac{1}{1+\mathcal{D}}\left[(\mathcal{D}h' + H' - (1+\mathcal{D}))\,h^3 + \frac{3}{2}(H'-1)(H-h)h^2\right], \tag{4.48}$$

upstream of the intrusion front $-\infty < \xi < 0$, and

$$q_u = 0, \tag{4.49}$$

$$q_l = -\,(h'-1)\,h^3, \tag{4.50}$$

downstream of the intrusion front $0 \le \xi < \infty$.

It can be shown that if we integrate (4.45)–(4.46) with respect to ξ, we have

$$-v(H-h) + q_u = 0, \tag{4.51}$$

$$-vh + q_l = -v + 1, \tag{4.52}$$

where the values on the right-hand-side can be obtained from the boundary conditions (4.43) and (4.44), respectively.

Additionally, from the upstream far-field boundary conditions (4.41), we have

$$-v(H_\infty - h_\infty) + q_{u\infty} = 0, \tag{4.53}$$

$$-vh_\infty + q_{l\infty} = -v + 1, \tag{4.54}$$

where the upstream far-field fluxes are given by

$$q_{u\infty} = \frac{1}{1+\mathcal{D}}\left[\mathcal{M}\,(H_\infty - h_\infty)^3 + \frac{3}{2}(1+\mathcal{D})(H_\infty - h_\infty)h_\infty^2 + 3(H_\infty - h_\infty)^2 h_\infty\right], \tag{4.55}$$

$$q_{l\infty} = \frac{1}{1+\mathcal{D}}\left[(1+\mathcal{D})h_\infty^3 + \frac{3}{2}(H_\infty - h_\infty)h_\infty^2\right]. \tag{4.56}$$

These conditions determine the velocity of the travelling wave, given by

$$v = \frac{q_{u\infty}}{H_\infty - h_\infty} = \frac{q_{l\infty} - 1}{h_\infty - 1}. \tag{4.57}$$

The first equality matches the result obtained in Figure 4.2(c) (demonstrating the velocity of the nose), while the second equality establishes a necessary condition for the existence of global travelling wave solutions, ensuring that the wave profile remains invariant over time. The derived condition implies that the values of $q_{u\infty}$ and $q_{l\infty}$ need to be chosen carefully to ensure a travelling-wave solution. Based on numerical solutions of the PDE as shown in Figure 4.2, one can infer that when the far-field boundary conditions do not satisfy (4.57), the region near the nose still develops a travelling-wave solution that satisfies (4.57), but with adjusted values of the upstream and downstream far-field flux. For example, Figure 4.2(a) provides evidence that the travelling-wave solution near the nose, were it to be extended beyond the vicinity of the nose, would satisfy the flux conditions at the upstream far field but not at the downstream far field. Also, in cases where no global travelling-wave solution exists, it is expected that there are regions away from the nose where the time derivative cannot be eliminated in the governing equations after transforming to the frame of the nose. A global travelling-wave solution only emerges when the far-field boundary conditions of the system happen to satisfy the derived condition (4.57), making it a special case. In summary, we find that travelling wave solutions exist at least locally near the nose.

4.6 Numerical scheme for the base flow

To solve equations (4.47)–(4.56), which are 1st-order ODEs describing the traveling-wave solutions, we impose boundary conditions $H = H_\infty$ and $h = h_\infty$ at the upstream far field, where (4.57) must be satisfied. To solve this system numerically, we employ Mathematica's in-built numerical solver NDSolve, by performing the following steps.

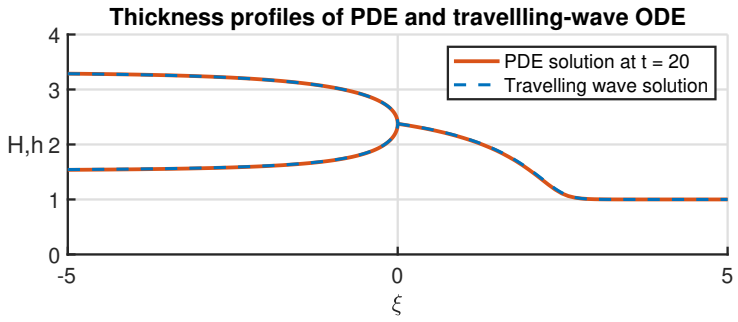

Figure 4.3: Comparison between the numerical solutions of the PDE system and travelling-wave system, parameter used: $\mathcal{M} = 2$, $\mathcal{D} = 1$, $q_{u\infty} = 19$, $q_{l\infty} = 6.73705$. Solid red: long-term PDE numerical solution. Dashed blue: travelling-wave ODE numerical solution.

First, we initiate the numerical integration of the two-layer region at an arbitrary value of ξ. Since the system consists of only autonomous ODEs, and so the choice of the initial ξ is arbitrary, the resulting thickness profile can be shifted so that the nose is located at $\xi = 0$. The integration is initialized with $[H, h] = [H_\infty, h_\infty] + \boldsymbol{\epsilon}_1$, where $\boldsymbol{\epsilon}_1$ is a small 2-dimensional vector added to perturb the starting thickness from the steady state $[H, h] = [H_\infty, h_\infty]$.

If the value of $\boldsymbol{\epsilon}_1$ is appropriately chosen, the numerical integration is expected to approach a square-root singularity in the thicknesses at the nose position $\xi = 0$. The integration is terminated just before the nose, at $\xi = -\delta$, where δ is a sufficiently small number, as the gradients H' and h' diverge at the nose. The local asymptotic analysis in Appendix A is then used to determine the variable values just after the nose, at $\xi = 0^+$, which serve as the initial conditions for the integration of the single-layer region. This integration is carried out until the lower-layer thickness h becomes sufficiently close to 1.

The numerically computed travelling wave solutions compare well with the numerical solution of the full PDEs, given that the parameter values are aligned, as depicted in Figure 4.3, where $q_{u\infty}$ is fixed and $q_{l\infty}$ is computed using (4.57). This comparison confirms that, given a prescribed downstream thickness, a global travelling-wave solution can be obtained by selecting the upstream far-field thicknesses H_∞ and h_∞ to satisfy condition (4.57).

4.7 Discussion of results for the base flow

4.7.1 Existence of multiple solutions

Upon exploring the parameter space, we find that for given values of $\mathcal{M}$ and D, multiple solutions can exist when the upper-layer far-field flux $q_{u\infty}$ is sufficiently low. For instance, when $\mathcal{M} = 2$ and $D = 1$, there exists a unique travelling-wave solution when $q_{u\infty} = 19$, as shown in Figure 4.3. In contrast, when $q_{u\infty} = 1$, infinitely many solutions appear, three examples of which are illustrated in Figure 4.4. All of these multiple travelling-wave solutions are of the same wave

(*a*)

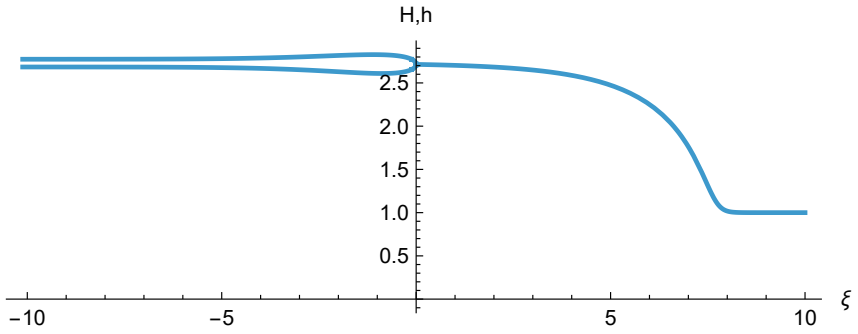

(*b*)

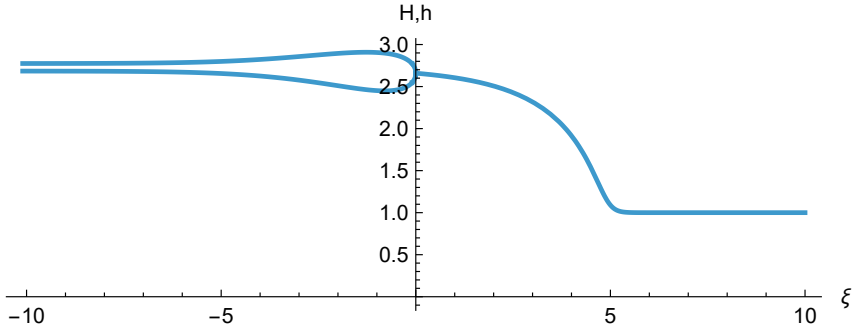

(*c*)

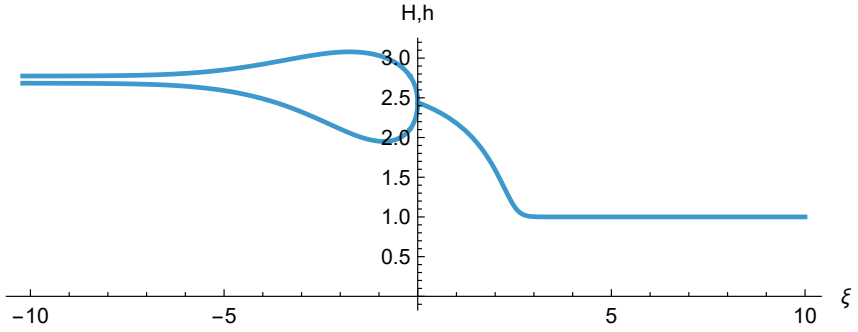

Figure 4.4: Examples of multiple numerical solutions found with the given parameter values $\mathcal{M} = 2$, $\mathcal{D} = 1$ and $q_{u\infty} = 1$.

(*a*)

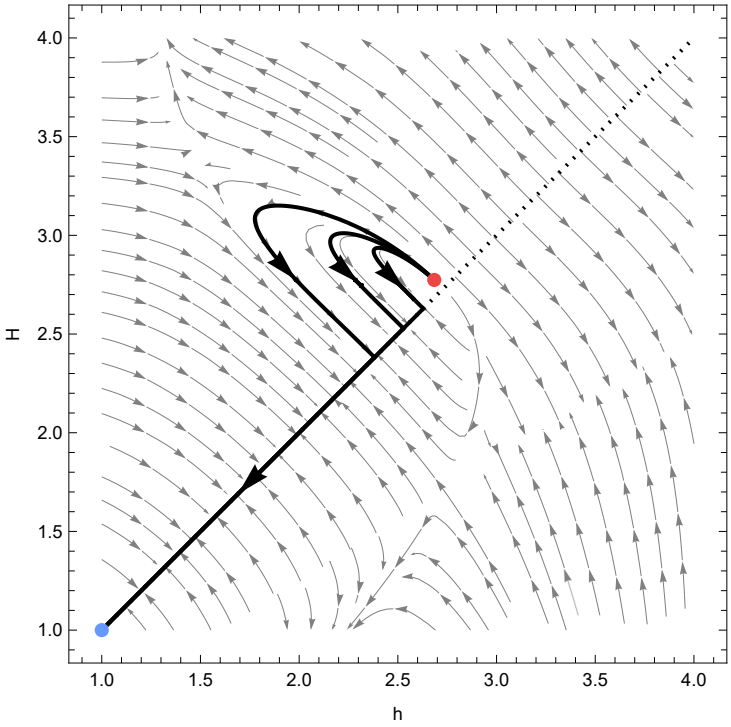

(*b*)

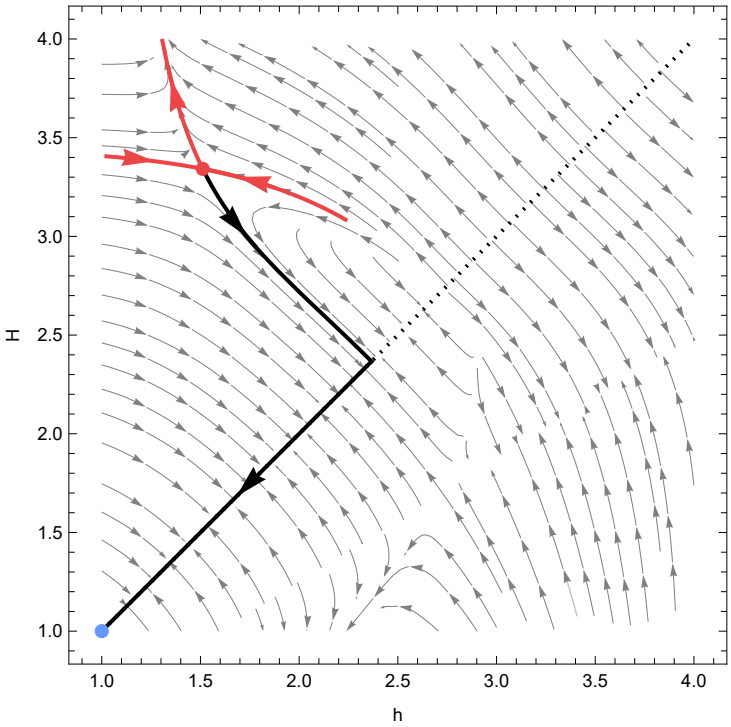

Figure 4.5: Phase portraits of the autonomous ODE system (4.51)–(4.52) in two regimes: (a) the multiple-solution case (Figure 4.4) and (b) the unique-solution case (Figure 4.3). The red (blue) point denotes the upstream (downstream) far-field fixed point. Solid black curves represent solution orbits. The dashed line corresponds to the constraint $H = h$, which separates the single-layer case ($H = h$) from the two-layer case ($H > h$). The red curves indicate the remaining stable and unstable manifolds of the saddle fixed point.

speed.

Mathematically, the multiplicity of travelling-wave solutions originates from a change in the stability of the upstream far-field fixed point (H_∞, h_∞) in the phase plane. Figure 4.5 presents representative phase portraits for two parameter regimes: (a) the multiple-solution case and (b) the unique-solution case. The red and blue points denote the upstream and downstream far-field fixed points, respectively, while the solid black curves represent solution trajectories. The arrows indicate the positive ξ-direction. The downstream far-field fixed point, corresponding to $h = 1$, remains stable throughout the parameter range considered. In contrast, the upstream far-field fixed point undergoes a qualitative change in stability as the control parameter $q_{u\infty}$ varies. Although the Jacobian matrix at this fixed point can be computed analytically, its complexity prevents us from obtaining an explicit criterion for this change in stability. As shown in Figure 4.5(a), the upstream far-field fixed point is unstable when $q_{u\infty}$ is sufficiently low. This instability causes nearby trajectories to diverge and ultimately approach the stable downstream far-field fixed point along different paths (the black curves), resulting in multiple valid travelling-wave solutions. In contrast, as shown in Figure 4.5(b), when $q_{u\infty}$ is sufficiently high, the upstream far-field fixed point becomes a saddle point. In this case, the system admits a unique heteroclinic orbit connecting the two fixed points. All nearby orbits in the vicinity of the upstream far-field fixed point decay toward this heteroclinic trajectory, resulting in a unique travelling-wave solution.

4.7.2 Large upper-layer flux limit

Since a unique solution exists when the upper-layer far-field flux $q_{u\infty}$ is sufficiently large, we are particularly interested in the asymptotic regime where $q_{u\infty} \to \infty$. By substituting this limit into the governing equations and performing an asymptotic analysis, we obtain the following results.

First, the wave speed is given by

$$v \sim \frac{q_{u\infty}^{2/3}\mathcal{M}^{1/3}}{(1+\mathcal{D})^{1/3}}. \tag{4.58}$$

The upstream lower-layer far-field flux becomes

$$q_{l\infty} \sim \frac{3q_{u\infty}^{1/3}}{2(1+\mathcal{D})^{2/3}\mathcal{M}^{1/3}}. \tag{4.59}$$

The upstream far-field thicknesses satisfy

$$H_\infty \sim \frac{q_{u\infty}^{1/3}(1+\mathcal{D})^{1/3}}{\mathcal{M}^{1/3}}, \tag{4.60}$$

$$h_\infty \sim 1. \tag{4.61}$$

(*a*)

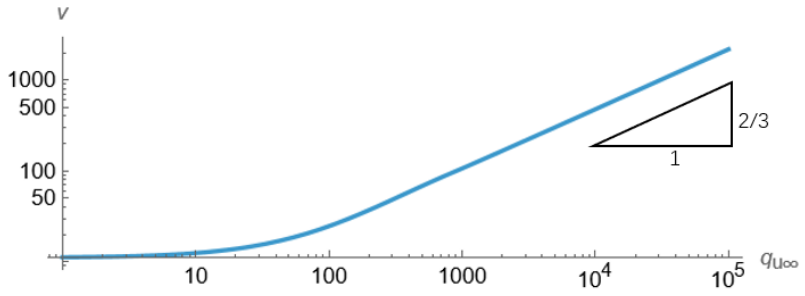

(*b*)

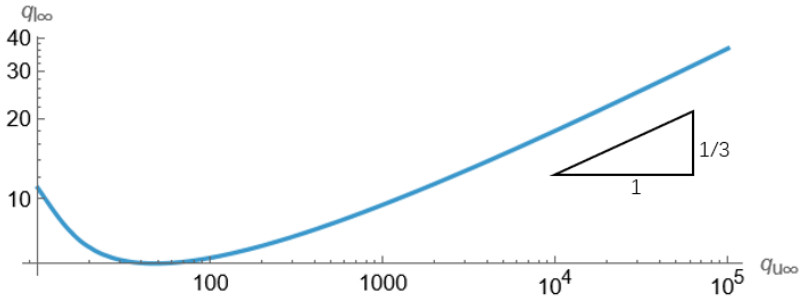

Figure 4.6: The (a) wave speed v and (b) upstream far-field lower-layer flux $q_{l\infty}$ for $q_{u\infty} \gg 1$ when $\mathcal{M} = 2$ and $\mathcal{D} = 1$. The asymptotic scalings (4.58) and (4.59) are displayed via the reference triangles, confirming consistency with the slope when $q_{u\infty} \gg 1$.

Furthermore, the two eigenvalues of the Jacobian matrix at the upstream far-field fixed point are given by

$$\lambda_1 \sim -\frac{(3+(-3+h_\infty)v)(1+\mathcal{D})}{h_\infty \mathcal{M}} H_\infty^3, \tag{4.62}$$

$$\lambda_2 \sim \frac{(3+(-3+h_\infty)v)(1+\mathcal{D})}{h_\infty \mathcal{M}}, \tag{4.63}$$

which confirms that the fixed point is a saddle, as λ_1 and λ_2 are real and of opposite signs.

Figure 4.6 shows the wave speed v and upstream far-field lower-layer flux $q_{l\infty}$ in the limit $q_{u\infty} \to \infty$. The numerical results verify the above asymptotic predictions.

4.7.3 Flow regimes across parameter space

We now explore the parameter space when the system has a unique solution. Three key parameters determine the flow: $\mathcal{M}$, $\mathcal{D}$, and $q_{u\infty}$. Each of these has a distinct influence on the structure and behaviour of the flow.

Figure 4.7 shows the thickness profile as the viscosity ratio $\mathcal{M}$ varies, where we observe a noticeable change in the interaction between the upper and lower layers. An increase in $\mathcal{M}$ implies that the lower layer becomes more viscous relative to the upper layer. In this case, the upper layer exerts negligible shear stress on the underlying layer, resulting in a relatively flat lower-layer thickness profile away from the nose. Conversely, when $\mathcal{M}$ is small, the upper layer

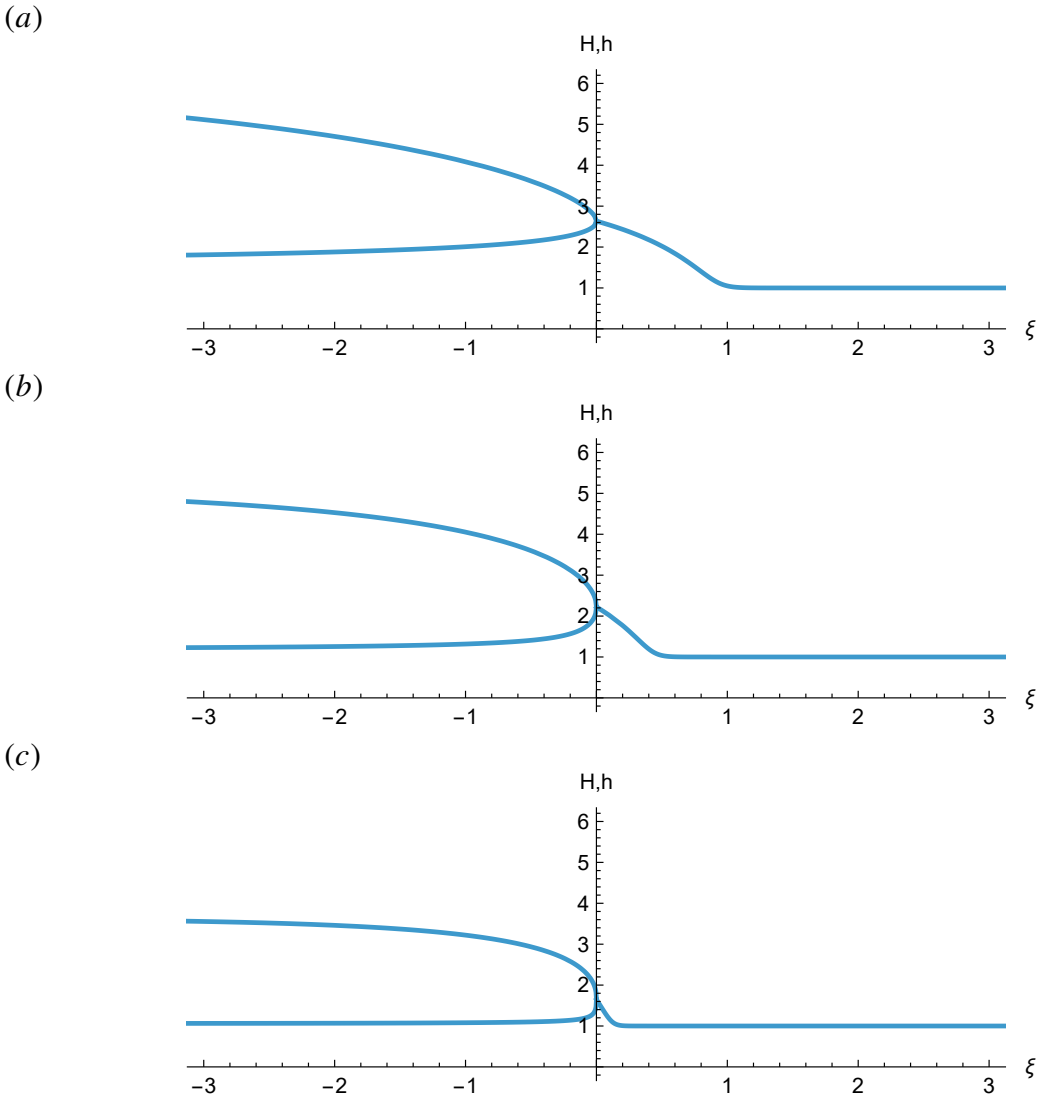

Figure 4.7: Wave profiles for varies viscosity ratios: (a) $\mathcal{M} = 0.4$, (b) $\mathcal{M} = 2$, (c) $\mathcal{M} = 10$, when $\mathcal{D} = 1$ and $q_{u\infty} = 100$.

(*a*)

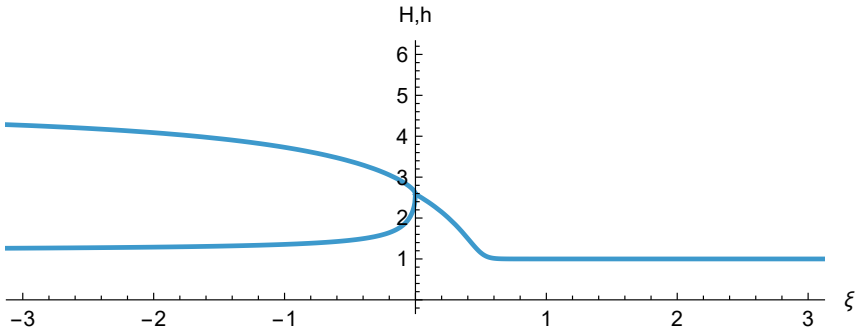

(*b*)

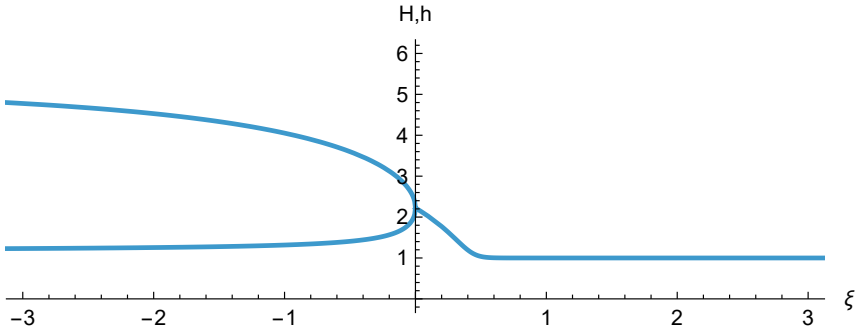

(*c*)

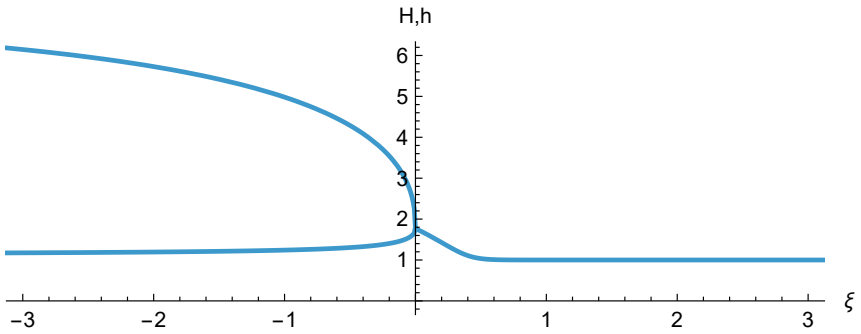

Figure 4.8: Wave profiles for various density differences: (a) $\mathcal{D} = 0.2$, (b) $\mathcal{D} = 1$, (c) $\mathcal{D} = 5$, when $\mathcal{M} = 2$ and $q_{u\infty} = 100$.

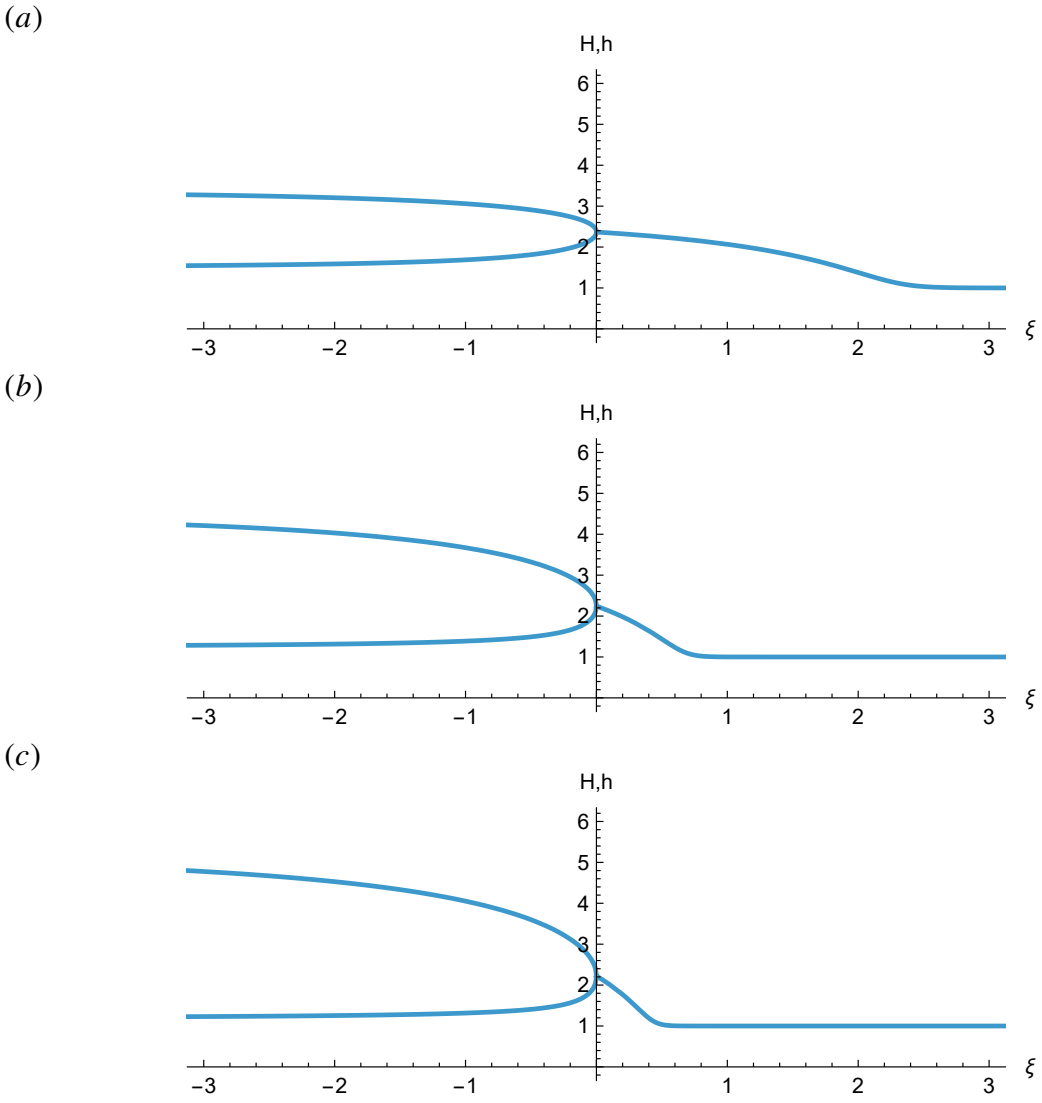

Figure 4.9: Wave profiles for various upper-layer upstream far-field fluxes: (a) $q_{u\infty} = 20$, (b) $q_{u\infty} = 60$, (c) $q_{u\infty} = 100$, when $\mathcal{M} = 2$ and $\mathcal{D} = 1$.

is more viscous, leading to more pronounced variations in the lower-layer thickness profile. In addition, at low values of $\mathcal{M}$, the intruding front tends to exhibit a linear rather than a singular structure, which aligns with the analogous observation reported in Dauck *et al.* (2019).

Figure 4.8 illustrates how the thickness profile changes with variations in the density difference $\mathcal{D}$. Decreasing $\mathcal{D}$ means that the density difference between the two layers becomes smaller, and so the upper layer becomes less and less buoyant relative to the lower layer, which causes a greater proportion of the upper-layer fluid to submerge into and invade the lower layer near the nose. On the other hand, increasing $\mathcal{D}$ results in the opposite effect: a smaller proportion of the upper-layer fluid submerges into the lower layer near the nose. We also observe that increasing $\mathcal{D}$ leads to a flatter upper surface of the lower layer, which is because the gravitational force within the lower layer outweighs that of the upper layer in this limit.

Finally, Figure 4.9 depicts the effects of varying the upper-layer upstream far-field flux $q_{u\infty}$. As $q_{u\infty}$ increases, the combined thickness of the two layers increases correspondingly, in line with the asymptotic result (4.60). Furthermore, thickness gradients downstream of the nose become sharper owing to a more substantial contrast in the far-field flux, and, therefore, thickness, upstream and downstream of the nose.

4.8 Stability analysis

We perform a linear stability analysis in a manner similar to that of §3. We aim to investigate how small perturbations evolve with the base, travelling-wave flow. For simplicity, we focus solely on the case where a unique solution exists. Specifically, we consider scenarios in which the upstream flux in the upper layer is sufficiently greater than the downstream flux in the lower layer, thereby ensuring the existence of a unique long-time travelling-wave solution.

As in §3, we restrict attention to real eigenvalues, motivated by experimental observations of closely related configurations that exhibit monotonic temporal behaviour. However, in the present setting the base state is a travelling wave, and temporal oscillations cannot be ruled out *a priori*. Although there is currently no direct experimental evidence indicating oscillatory instabilities in this regime, the possibility of complex eigenvalues cannot be excluded. Investigating this further, either through targeted experiments or by explicitly searching for complex eigenvalues, would be a natural direction for future work.

To facilitate this analysis, we linearize the transformed problem by defining

$$X(x,y,t) \equiv X(\Lambda,Y,\tau) = X_0(\Lambda) + \epsilon\tilde{X}_1(\Lambda,Y,\tau) + \ldots \tag{4.64}$$

for dependent variables $X = H, h, q_u, q_l$, where ϵ is an arbitrary small number, X_0 is the basic-state solution, $\tilde{X}_1$ is the small-amplitude perturbation to X_0 and the independent variable trans-

formation is given by

$$\Lambda = \begin{cases} -(x_N(y,t)-x)^{1/2} & \text{when} \quad x < x_N(t), \\ x - x_N(y,t) & \text{when} \quad x \geq x_N(t), \end{cases} \tag{4.65}$$

$$Y = y, \tag{4.66}$$

$$\tau = t. \tag{4.67}$$

Here, the transformation of $\Lambda = -(x_N(t)-x)^{1/2}$ for $x < x_N(t)$ is introduced to resolve the square-root singularity of H and h that occurs near the intrusion front within the two-layer region.

The intrusion front is linearized as

$$x_N(y,t) \equiv x_N(Y,\tau) = v\tau + \epsilon\tilde{x}_{N1}(Y,\tau), \tag{4.68}$$

where we note that $x_{N0} = v\tau$ is the position of the nose of the base flow, given it is a travelling wave, and $\tilde{x}_{N1}$ is the small-amplitude perturbation to the intrusion front.

Furthermore, to analyse the evolution of the perturbations, we seek normal mode solutions of the form

$$\tilde{X}_1(\Lambda,Y,\tau) = X_1(\Lambda)e^{\sigma\tau+ikY}, \tag{4.69}$$

$$\tilde{x}_{N1}(Y,\tau) = x_{N1}e^{\sigma\tau+ikY}. \tag{4.70}$$

Substituting the above transformation, we obtain the governing equations for the perturbations of the form

$$\sigma\boldsymbol{v} = \boldsymbol{L}\boldsymbol{v}, \tag{4.71}$$

where $\boldsymbol{v} = [H_1, h_1, x_{N1}]^T$ denotes the thickness perturbation vector, and $\boldsymbol{L} = \boldsymbol{L}(H_0, h_0, H_0', h_0', k)$ is a linear operator.

The accompanying boundary conditions are

$$H_1 \to 0 \quad \text{as} \quad \Lambda \to -\infty, \tag{4.72}$$

$$h_1 \to 0 \quad \text{as} \quad \Lambda \to -\infty, \tag{4.73}$$

$$h_1 \to 0 \quad \text{as} \quad \Lambda \to \infty, \tag{4.74}$$

$$[h_1]_-^+ = 0 \quad \text{at} \quad \Lambda = 0, \tag{4.75}$$

$$[q_{l1}]_-^+ = 0 \quad \text{at} \quad \Lambda = 0, \tag{4.76}$$

$$q_{u1} \to 0 \quad \text{as} \quad \Lambda \to 0^-, \tag{4.77}$$

$$\sigma x_{N1} - \frac{q_{u1}}{H_0 - h_0} + \frac{q_{u0}(H_1 - h_1)}{(H_0 - h_0)^2} \to 0 \quad \text{as} \quad \Lambda \to 0^-. \tag{4.78}$$

The equations and boundary conditions specified here form an eigenvalue problem for the un-

known growth rate σ, which we wish to find numerically, given a specified wavenumber k, in the following section.

4.9 Numerical scheme for the perturbations

The numerical scheme employed here is similar to the one described in §3. The approach involves shooting backwards from the downstream far field, using initial guesses for x_{N1}, σ, and $q_{l1}(\infty)$. If these guessed values are accurate, the solution will recover the correct boundary conditions at the upstream far field, namely $H_1(-\infty) = 0$ and $h_1(-\infty) = 0$, evidenced by the zero determinant of the corresponding error matrix, as described in §3.

Several challenges arise in implementing this method, which we resolve as follows. First, although we transformed the independent variable from x to Λ to eliminate the square-root singularity in the thickness profiles H and h, the nose position $\Lambda = 0$ remains a singular point. At this location, the expressions for H_1'', h_1'' as well as H_0'', h_0'' exhibit an indeterminate form $0/0$. This issue is resolved by employing an asymptotic approximation to smoothly pass through the nose position.

Second, just like in §3, we aware that H_1 and h_1 can exhibit exponential growth as $\Lambda \to \pm\infty$, which can degrade the accuracy of the numerical solution. To mitigate this, we introduce a rescaling of H_1 and h_1 to decouple the exponential behaviour, by setting

$$[H_1, h_1] = e^{\alpha\Lambda}[\hat{H}_1, \hat{h}_1] \quad \text{when} \quad \Lambda < 0, \tag{4.79}$$

$$h_1 = e^{\beta\Lambda}\hat{h}_1 \quad \text{when} \quad \Lambda > 0, \tag{4.80}$$

where the values of α and β are determined by solving the eigenvalue problem (4.71) in the limits $\Lambda \to -\infty$ and $\Lambda \to \infty$, respectively. The values of α and β are selected as those corresponding to the fastest growing eigenvalue in each limit. The numerical scheme is then implemented using variables $[\hat{H}_1, \hat{h}_1]$, which is of order unity at the two far fields.

To validate the numerical results, we verified that the computed solutions are invariant under changes in numerical parameters, including the solver tolerance and the truncation of the computational domain.

4.10 Stability Thresholds

In this section, we examine the onset of instability and its key characteristics, including growth rates, the range of unstable wavenumbers, the critical wavenumber, and how these quantities vary across the parameter space. In particular, we map the behavior of small disturbances to the base flow in terms of three key dimensionless parameters: the viscosity ratio $\mathcal{M}$, the density difference $\mathcal{D}$, and the upstream far-field upper-layer flux $q_{u\infty}$.

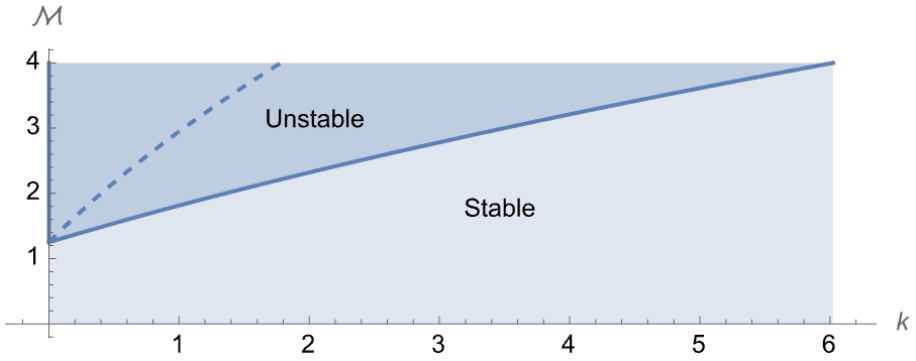

Figure 4.10: Neutral stability curve (solid) displaying the neutral viscosity ratio as a function of the wavenumber, also showing the critical wavenumber k_c (dashed), when $\mathcal{D} = 0.2$ and $q_u = 19$.

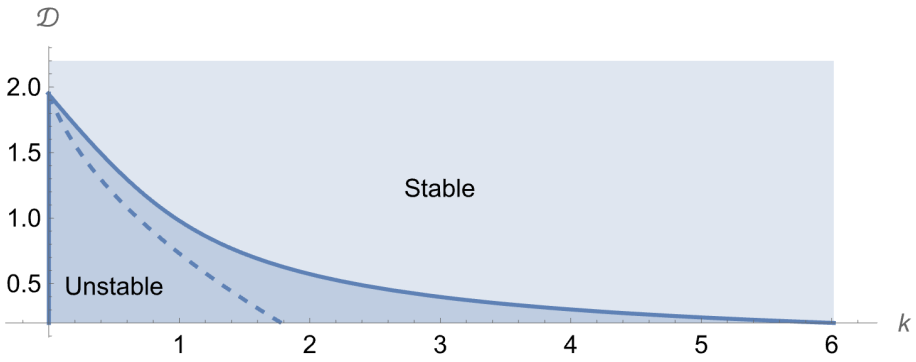

Figure 4.11: Neutral stability curve (solid) displaying the neutral density difference as a function of the wavenumber, also showing the critical wavenumber k_c (dashed), when $\mathcal{M} = 4, q_u = 19$, the flow is unstable for density differences below this neutral stability curve. The flow is stable for density differences above this neutral stability curve.

Figure 4.10 indicates that instability occurs only when the viscosity ratio $\mathcal{M}$ is sufficiently large. This implies that the intruding fluid layer must be sufficiently less viscous than the underlying fluid for the flow to become unstable. The critical wavenumber k_c, defined as the wavenumber at which the growth rate attains its maximum value, is found to increase monotonically with $\mathcal{M}$.

We find that instabilities arise only when the density difference $\mathcal{D}$ is sufficiently small, as shown in Figure 4.11. This suggests that the intruding fluid layer must be only slightly less dense than the underlying fluid for the flow to become unstable. That is, buoyancy forces associated with the upper layer are stabilising, as seen in Chapter 3 for flows over a horizontal substrate. Additionally, the critical wavenumber k_c decreases with $\mathcal{D}$.

We find that the flow is unstable only when the upstream far-field upper-layer flux $q_{u\infty}$ is sufficiently large, as shown in Figure 4.12. That is, a substantial flux of the intruding fluid is required for the onset of instability. The critical wavenumber k_c is also observed to increase with $q_{u\infty}$. Recalling that the upstream far-field lower-layer flux $q_{l\infty}$ is determined by condition (4.57) and scales as $q_{u\infty}^{1/3}$ in the limit $q_{u\infty} \to \infty$, as illustrated in Figure 4.6, we note that for large $q_{u\infty}$, an increase in $q_{u\infty}$ leads to a corresponding increase in the total upstream far-field flux. These

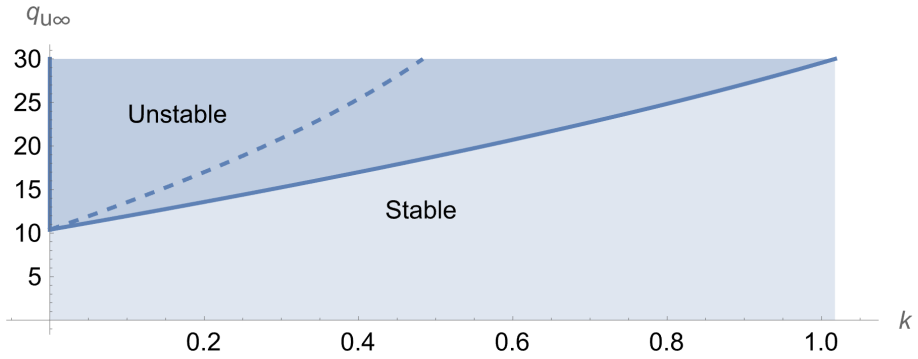

Figure 4.12: Neutral stability curve (solid) displaying the neutral density difference as a function of the wavenumber, also showing the critical wavenumber k_c (dashed), when $\mathcal{D} = 0.4$, $\mathcal{M} = 2$.

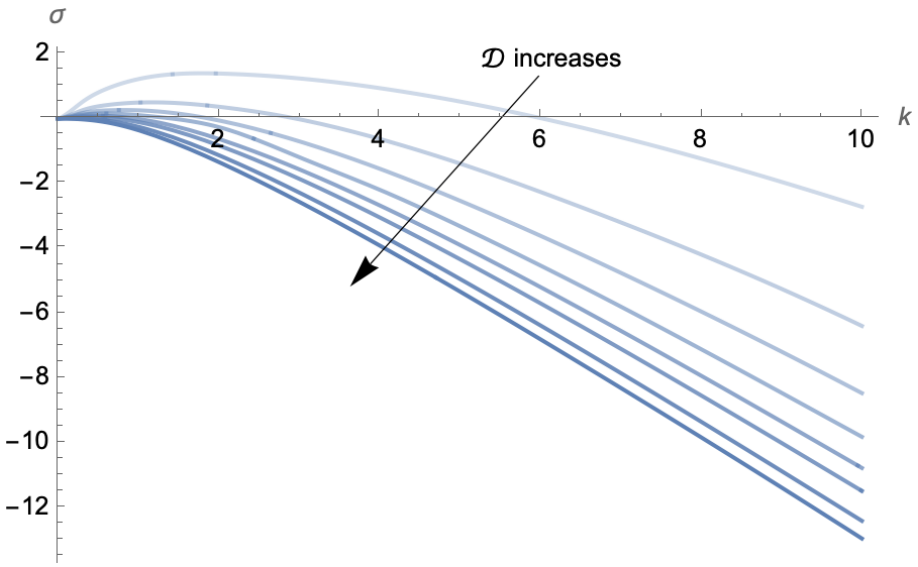

Figure 4.13: The growth rate versus the wavenumber for various densities differences $\mathcal{D} = 0.2, 0.4, 0.6, 0.8, 1.2, 1.6, 2$ when $\mathcal{M} = 4, q_u = 19$.

results collectively imply that a large total upstream flux is necessary for the flow to become unstable.

These findings indicate that the stability threshold exhibits similar trends to that of axisymmetric intrusions discussed in §3, suggesting a shared underlying mechanism driving the instability. However, numerical results also reveal that flow on the inclined plate is more prone to instability than axisymmetric flow on a horizontal substrate. This is evidenced by the fact that the critical parameter values required to trigger instability are less restrictive for flows down a plane. For instance, when all other parameters are of order unity, instability on the inclined plane occurs for viscosity ratios greater than about 1 (Figure 4.10), whereas for axisymmetric spreading over a horizontal substrate, $\mathcal{M}$ must exceed approximately 100 (Figure 3.4).

This observation is analogous to related fingering of gravity-driven single-layer films (Huppert, 1982*a*), in which a constant-volume flow down an inclined plane becomes unstable and develops a characteristic fingering pattern. In contrast, single-layer flows over a horizontal sub-

strate remain stable (Huppert, 1982*b*), highlighting that a streamwise component of gravity is necessary to induce fingering of single-layer spreading films. However, we note that fingering instabilities of gravity-driven single-layer films arise from capillary effects at the contact line, which is a mechanism that is fundamentally different from the one we consider here. The instability reported in this chapter arises from a viscosity contrast and is independent of capillary effects.

Lastly, we compare the eigenvalue branches in the two configurations. Figure 4.13 shows the dependence of the growth rate σ on the wavenumber k for different density differences $\mathcal{D}$ in flow down an inclined plane, while Figure 3.3 presents the corresponding variation of σ with k for different viscosity ratios $\mathcal{M}$ in the axisymmetric flow over a horizontal substrate. A notable distinction between the two cases arises at zero wavenumber. For the two-dimensional inclined-plane configuration, the growth-rate curve originates at the origin, indicating that the zero-wavenumber mode has zero growth rate. This behaviour is a direct consequence of the translational invariance of the travelling-wave base state under uniform shifts along the direction of propagation, which gives rise to a neutral mode at $k = 0$. In contrast, for the axisymmetric horizontal-substrate configuration, the growth rate at zero wavenumber is -1. This reflects a symmetry-induced time-shift mode associated with the self-similar base state, which is invariant under shifts of the time origin in physical time. The difference in behaviour at $k = 0$ is therefore purely structural, arising from the distinct symmetries of the two systems. Specifically, the two formulations employ different time parametrisations. In the inclined-plane case, the growth rate is defined with respect to physical time, whereas in the axisymmetric horizontal-substrate case the stability analysis is carried out in logarithmic (similarity) time.

4.11 Conclusions

We explored the dynamics of a viscous gravity current intruding over a denser, underlying thin film of viscous fluid down an inclined plane, fed by a uniform far-field line source. Both layers spread as long and thin films of fluid, which we model using lubrication theory.

Numerical simulations of the full system of governing equations reveal the emergence of a travelling-wave solution: both the thickness and the speed of the intrusion front approach a constant as time progresses. Motivated by this, we derived a necessary condition for the existence of travelling-wave solutions in terms of far-field quantities.

These travelling-wave solutions depend upon three key dimensionless parameters: the viscosity ratio and relative density difference between the two layers and the dimensionless flux of the intruding layer. Interestingly, we observed the presence of multiple solutions when the upper-layer flux is sufficiently small in the far field. In contrast, a unique solution emerges when the upper-layer flux is large, as confirmed by examining the eigenvalues of the Jacobian at the upstream, far-field fixed point. An asymptotic analysis reveals a power-law relationship between

key quantities in this large-flux limit. A range of flow behaviours is possible, with pronounced variations in the lower-layer depth near the nose when the density difference between the two layers is small. The upper layer exerts negligible shear stress on the lower layer when the viscosity ratio is large, leading to a relatively uniform thickness of the lower layer in this limit, except near the intrusion front. The horizontal length scale of the transition region over which the film adjusts between the upstream and downstream uniform far-field solutions is largest for small viscosity ratios, small density differences and small dimensionless upper-layer fluxes.

A linear stability analysis of the travelling wave solutions revealed conditions under which such flows an prone to viscous fingering. The stability thresholds are qualitatively similar to those of the axisymmetric, horizontal flow analogue: instabilities occur for large viscosity ratios, small density differences, and large upstream fluxes. However, flows down an inclined plane are more susceptible to instability, with low thresholds of instability, which we attribute to higher hydrostatic pressure gradients owing to a streamwise component of gravity associated with the slope of the substrate.

Part II

Thin-film flows past porous membranes

Chapter 5

Mathematical modelling of haemodialysis and haemodiafiltration

5.1 Introduction

In this chapter, we turn to exploring the fluid mechanics and solute transport of haemodialysis (HD) and haemodiafiltration (HDF) at the scale of a single fibre of a typical dialyser. To date, non-CFD models of dialysis have not resolved the fluid flow within the dialyser, instead imposing ad-hoc assumptions on its uniformity. Additionally, these "box" models have not accounted for the geometry of fibres, which are more realistically represented by axisymmetric hollow cylindrical shells. In this chapter, we develop a mathematical framework in which we fully model the fluid flow, arrive at a consistent set of reduced equations that capture the key dynamics and recover existing results from the literature as special cases in different asymptotic limits. In particular, we extend the existing "box" models for dialysis including HD and HDF, with an emphasis on rigorous mathematical formulation and the ability to capture both diffusive and convective transport. In contrast to existing literature, which describes the whole dialyser in terms of a “box” model, in which fluid flux is assumed to be uniform, we model each fibre as an axisymmetric hollow cylinder, representative of typical dialysers and resolve spatial variations in the flow field. For completeness, we also provide an equivalent model for two-dimensional (flat-layer) fibres, most closely resembling existing "box" models commonly used in the literature and dialysis industry. We will justify the adequacy of the simple "box" model and outline the underlying assumptions that support their use. To reduce model complexity and gain analytical insight, we employ asymptotic techniques for low-permeability fibre membranes. The underlying fluid mechanics are formulated using lubrication theory as appropriate for the length and time scales involved, while transport across the semipermeable membrane is modelled using principles from linear non-equilibrium mass transfer dynamics. In particular, we capture solute transport within the blood and dialysate using advection-diffusion equations. We aim to formalize and extend existing models from the literature into a consistent mathematical framework

and develop new asymptotic formulae estimating the effectiveness of dialysis therapy for low-permeability membranes, including convective effects. Our work provides a unifying framework faithful to the underlying hydrodynamics of the system and gives credence to prior ad-hoc assumptions made in the literature. It also allows for higher-order corrections to be made to the leading-order results, as required. This work also serves as a foundation for future, more detailed predictive modelling efforts in dialysis research, including exploring dialysis treatment under non-steady flow, which would not be possible without resolving for the fluid flow as with other ad-hoc "box" models.

5.2 Anatomy of a dialyser

A dialyser consists of roughly ten thousand hollow fibres, as pictured in Figure 1.6. Blood flows in the interior of each fibre, while dialysate flows in the exterior, typically in the opposite direction to the blood flow to maximise diffusive solute transport. We provide estimates of parameter values describing the dialyser based on the manufacturer's technical and in-vitro performance data for the Braun Diacap® Pro 19H Dialyser, laboratory measurements and inferred estimates in table 5.1.

Quantities describing the dialyser geometry known from the manufacturer's technical and in-vitro performance data include the fibre internal radius r_b, fibre external radius r_m, fibre membrane thickness δ, and membrane surface area S. Quantities measured in the laboratory using a Braun Diacap® Pro 19H Dialyser include the dialyser length L occupied by blood and dialysate and the dialyser radius R.

We infer an estimate for the number N of fibres by comparing the manufacturer-provided membrane surface area, S, to the total internal surface area of the fibres, $2\pi r_b LN$, which gives $N = S/(2\pi r_b L)$.

The fibres are generally arranged in a hexagonal lattice, as shown in Figure 5.2. We assume that the fibres are packed sufficiently loosely that the outer hexagonal edge can be approximated by a circle of radius r_d, as depicted in figure 5.1. We approximate the outer radius r_d by relating the total area of all the compartments, $\pi r_d^2 N$, to the cross-sectional area of the dialyser, πR^2, which gives the effective outer dialysate radius $r_d = R/\sqrt{N}$.

5.3 Fluid flow

Consider the flow of two thin layers of viscous fluid in a hollow porous fibre, as depicted in the schematic of Figure 5.1. Blood flows in the interior of the hollow fibre in a domain of cross section $\mathscr{D}_b$ and outer boundary Γ_b, while dialysate flows in the exterior of the fibre in a domain of cross section $\mathscr{D}_d$ and outer boundary Γ_d. We denote quantities referring to the blood and dialysate by the subscripts b and d, respectively, and define the velocity of the two fluids by $\boldsymbol{u}_l$,

Quantity	Symbol	Value
Dialyser geometry		
Dialyser length occupied by blood and dialysate†	L	0.26 m
Dialyser radius†	R	0.0225 m
Dialyser cross-sectional area†	πR^2	$1.6\times10^{-3}\,\mathrm{m}^2$
Number of fibres‡	$N = V_b/(\pi r_b^2 L)$	14,691
Total blood volume*	V_b	120 ml
Fibre geometry		
Fibre internal radius*	r_b	100 μm
Fibre external radius*	r_m	137 μm
Fibre membrane thickness*	δ	37 μm
Effective outer dialysate radius‡	$r_d = R/\sqrt{N}$	186 μm
Blood cross-sectional area per fibre	$A_b = \pi {r_b}^2$	$3.14\times10^{-8}\,\mathrm{m}^2$
Dialysate cross-sectional area per fibre	$A_d = \pi(r_d^2 - r_m^2)$	$6.17\times10^{-8}\,\mathrm{m}^2$
Membrane properties		
Ultrafiltration coefficient*	K_{uf}	$97\,\mathrm{ml\,h^{-1}\,mmHg^{-1}}$
Mass transfer-area coefficient for urea*	K_{oA}	$1415\,\mathrm{ml\,min^{-1}}$
Total effective membrane hydraulic conductivity(5.26)	$\mathcal{K} = K_{uf}/(NL)$	$5.3\times10^{-14}\,\mathrm{m^3\,s\,kg^{-1}}$
Effective membrane diffusivity(5.106)	$D = K_{oA}/(NL)$	$6.2\times10^{-9}\,\mathrm{m^2\,s^{-1}}$
Flow rates		
Total dialysate flux through the dialyser*	Nq_{d0}	−500 ml/min
Total blood flux through the dialyser*	Nq_{b0}	300 ml/min
Dialysate flux per fibre‡	q_{d0}	−0.034 ml/min
Blood flux per fibre‡	q_{b0}	0.02 ml/min
Fluid properties		
Dialysate kinematic viscosity	ν_d	$10^{-6}\,\mathrm{m^2\,s^{-1}}$
Blood kinematic viscosity	ν_b	$4\times10^{-6}\,\mathrm{m^2\,s^{-1}}$
Dialysate density	ρ_d	$1.000\,\mathrm{g\,ml^{-1}}$
Blood density	ρ_b	$1.057\,\mathrm{g\,ml^{-1}}$

Table 5.1: Parameters describing the flow and solute transport of blood and dialysate through the dialyser.

∗ Manufacturer's technical and in-vitro performance data for the Braun Diacap® Pro 19H Dialyser.

† Measured in the laboratory using the Braun Diacap® Pro 19H Dialyser.

‡ Inferred based on the manufacturer's technical data and laboratory measurements.

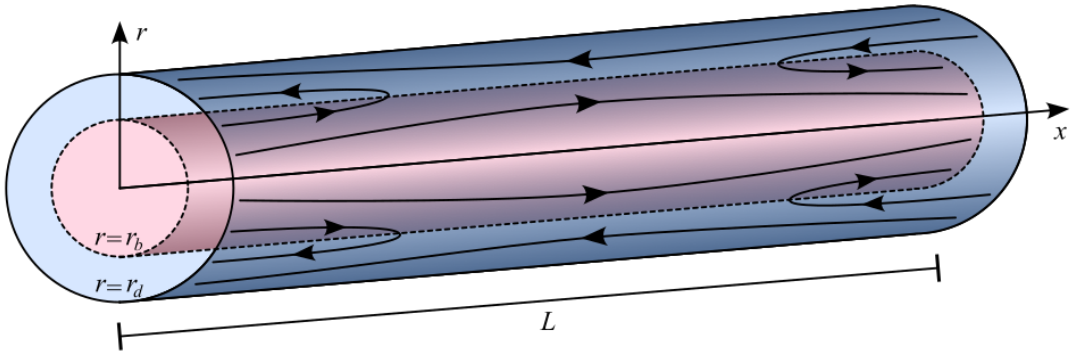

Figure 5.1: Schematic of a single hollow fibre, separating blood and dialysate, in the axisymmetric geometry. Blood flows from left to right in the interior ($r < r_b$, shaded pink) of the fibre membrane and dialysate flows from right to left in the exterior ($r_b < r < r_d$, shaded blue) of the fibre membrane.

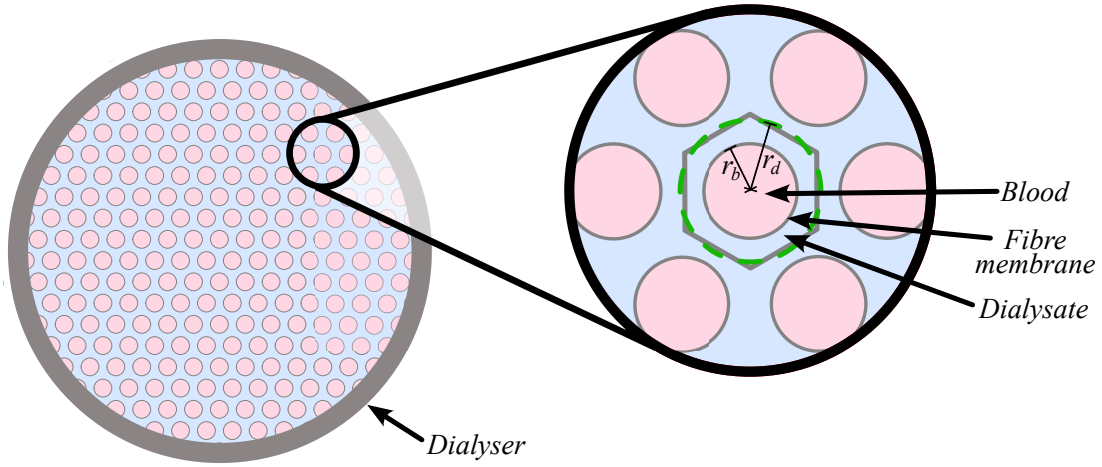

Figure 5.2: Schematic representation of the cross-section of a typical dialyser (left-hand panel), consisting of thousands of hollow fibres arranged in a hexagonal lattice, together with an inset (right-hand panel) depicting a single hollow fibre, the radius r_b of the fibre, and the effective radius r_d of the hexagonal region surrounding each fibre.

the pressure by p_l and the dynamic viscosity by μ_l, where $l = b$ or $l = d$. We define a coordinate system $\hat{\boldsymbol{x}} = (x, \boldsymbol{r})$ in which the distance along the fibre membrane is measured in x, while the coordinate vector $\boldsymbol{r}$ is orthogonal to the fibre membrane. We define ∇ as the gradient in $\boldsymbol{r}$ and express the fluid velocity as $\boldsymbol{u}_l = (u_l, \boldsymbol{v}_l)$, in terms of the axial velocity u_l, along the fibre, and the transmembrane velocity $\boldsymbol{v}_l$, normal to the fibre membrane. We also define $\boldsymbol{n}_l$ as the outward unit normal vector to $\mathscr{D}_l$.

The fibres in a typical dialyser are arranged in a hexagonal lattice and are of a circular-cross section so that $\mathscr{D}_b$ is a circle and $\mathscr{D}_d$ a hexagon. However, for loosely-packed fibres, it is sufficient to assume that $\mathscr{D}_d$ is circular as well. As such, we assume that the flow and solute transport within the blood and dialysate is axisymmetric. A convenient choice of coordinate system is, therefore, the cylindrical coordinate system in which the radial position vector $\boldsymbol{r}$ is spanned by the coordinates (r, θ) and the flow is independent of the azimuthal coordinate θ, so that $\boldsymbol{v}_l = v_l \boldsymbol{e}_r$. We denote the outer boundary Γ_l of the blood and dialysate by $r = r_l$ in the axisymmetric geometry. For completeness, we also refer to the two-dimensional coordinate system in which the fibre membrane is flat and $\boldsymbol{r}$ is spanned by Cartesian coordinates (y, z), given its use in the dialysis literature, where the flow is independent of z, so that $\boldsymbol{v}_l = v_l \boldsymbol{e}_y$. In the two-dimensional geometry, we denote the outer boundary Γ_l of the blood and dialysate by $y = h_l$ and refer to a typical thickness W in the z-direction.

5.3.1 Lubrication theory

Given the thin aspect ratio and the length and time scales of the flow, we assume the effects of inertia are negligible and that the assumptions of lubrication theory hold. We also assume that the viscosity of blood plasma and dialysate are equal, so that $\mu_b = \mu_d = \mu$. Therefore, to leading order, the flow within the blood and dialysate satisfies the axial momentum equation

$$0 = -\frac{\partial p_l}{\partial x} + \mu \nabla^2 u_l, \tag{5.1}$$

describing a balance of viscous forces. The transmembrane momentum balance yields

$$0 = -\nabla p_l, \tag{5.2}$$

so that the pressure is uniform across the cross section $\mathscr{D}_l$. As the fluid is incompressible, the velocity field satisfies the continuity equation

$$\frac{\partial u_l}{\partial x} + \nabla \cdot \boldsymbol{v}_l = 0. \tag{5.3}$$

For the purpose of examining the fluid flow, we assume that the membrane thickness is negligible and express boundary conditions either side of the membrane as those applied at Γ_b. However, we note that a precise derivation of bulk equations describing solute transport across

the fibre membrane requires a treatment in which the membrane thickness is nonzero, for which we refer the reader to §5.4.

For the blood, we assume that the fluid velocity is bounded within $\mathscr{D}_b$. Alternatively, in the two-dimensional geometry, we assume that the flow is symmetric about $y = 0$. We also assume that the blood and dialysate satisfy the no-slip condition at the membrane, so that

$$u_b = u_d = 0 \quad \text{on } \Gamma_b. \tag{5.4}$$

We also assume that the transmembrane velocity satisfies the membrane Darcy law

$$v_b = v_d = K(\Delta p - \Delta\Pi) \quad \text{on } \Gamma_b, \tag{5.5}$$

when in contact with the porous membrane. Here, $\Delta p = p_b - p_d$ refers to the fluid pressure jump, $\Delta\Pi = \Pi_b - \Pi_d$ refers to the osmotic pressure jump across the membrane, and K refers to the effective hydraulic conductivity through the membrane. For a detailed derivation of the integrated Darcy's law (5.5), we refer the reader to §5.4.2, where a version of this equation, (5.65), was derived in the axisymmetric geometry.

The remaining boundary conditions involve symmetry and no penetration through the outer boundary of the dialysate, so that

$$\nabla u_d \cdot \boldsymbol{n}_d = 0 \quad \text{and} \quad \boldsymbol{v}_d \cdot \boldsymbol{n}_d = 0 \quad \text{on } \Gamma_d, \tag{5.6}$$

Explicitly, at the outer boundary Γ_d, we have $\boldsymbol{n}_d = \boldsymbol{e}_r$ in the axisymmetric geometry and $\boldsymbol{n}_d = \boldsymbol{e}_y$ in the two-dimensional geometry.

Solving the axial momentum equation (5.1) for the axial velocity subject to the above boundary conditions gives

$$u_b = \begin{cases} \dfrac{1}{4\mu}\left(r^2 - r_b^2\right)\dfrac{\partial p_b}{\partial x} & \text{(axisymmetric)}, \\ \dfrac{1}{2\mu}\left(y^2 - h_b^2\right)\dfrac{\partial p_b}{\partial x} & \text{(two-dimensional)}, \end{cases} \tag{5.7}$$

within the blood and

$$u_d = \begin{cases} \dfrac{1}{4\mu}\left(r^2 - r_b^2 + 2r_d^2 \log\left(\dfrac{r_b}{r}\right)\right)\dfrac{\partial p_d}{\partial x} & \text{(axisymmetric)}, \\ \dfrac{1}{2\mu}(y - h_b)(y + h_b - 2h_d)\dfrac{\partial p_d}{\partial x} & \text{(two-dimensional)}, \end{cases} \tag{5.8}$$

within the dialysate.

Integrating the continuity equation (5.3) yields the transmembrane velocity

$$v_b = \begin{cases} -\dfrac{1}{16\mu} r \left(r^2 - 2r_b^2\right) \dfrac{\partial^2 p_b}{\partial x^2} & \text{(axisymmetric)}, \\ -\dfrac{1}{6\mu} y \left(y^2 - 3h_b^2\right) \dfrac{\partial^2 p_b}{\partial x^2} & \text{(two-dimensional)}, \end{cases} \tag{5.9a}$$

within the blood and

$$v_d = \begin{cases} \dfrac{1}{16\mu r} \left[\left(r_d^2 - r^2\right)\left(r^2 - 2r_b^2 + 3r_d^2\right) + 4r^2 r_d^2 \log\left(\dfrac{r}{r_b}\right) + 4r_d^4 \log\left(\dfrac{r_b}{r_d}\right)\right] \dfrac{\partial^2 p_d}{\partial x^2} \\ \dfrac{1}{6\mu}\left(h_d - y\right)\left(y^2 - 2h_d\left(y + h_d\right) + 6h_b h_d - 3h_b^2\right) \dfrac{\partial^2 p_d}{\partial x^2} \end{cases} \tag{5.9b}$$

within the dialysate, for axisymmetric and two-dimensional geometries, respectively.

We note that the pressure condition (5.5) has not been applied to determine the axial and transmembrane velocities. It will instead be used to determine a global condition on fluid flux, which we define by

$$q_l = \int_{\mathscr{D}_l} u_l \, \mathrm{d}A. \tag{5.10}$$

Explicitly, integrating the axial velocity yields the fluid flux

$$q_b = -\mathcal{R}_b^{-1} \frac{\partial p_b}{\partial x}, \tag{5.11a}$$

within the blood and

$$q_d = -\mathcal{R}_d^{-1} \frac{\partial p_d}{\partial x}, \tag{5.11b}$$

within the dialysate, where

$$\mathcal{R}_b = \begin{cases} \dfrac{8\mu}{\pi r_b^4} & \text{(axisymmetric)}, \\ \dfrac{3\mu}{W h_b^3} & \text{(two-dimensional)}, \end{cases} \tag{5.11c}$$

and

$$\mathcal{R}_d = \begin{cases} \dfrac{8\mu}{\pi}\left[4r_b^2 r_d^2 - r_b^4 - 3r_d^4 - 4r_d^4 \log\left(\dfrac{r_b}{r_d}\right)\right]^{-1} & \text{(axisymmetric)}, \\ \dfrac{3\mu}{W(h_d - h_b)^3} & \text{(two-dimensional)}, \end{cases} \tag{5.11d}$$

represent the hydraulic resistance per unit length (along the fibre) of the blood and dialysate channel, respectively.

We derive global mass conservation equations by integrating the continuity equation (5.3) across the cross-section $\mathscr{D}_l$ and applying the two-dimensional divergence theorem to get that the

divergence of flux,

$$\frac{\partial q_l}{\partial x} = -\int_{\partial \mathscr{D}_l} \boldsymbol{v}_l \cdot \boldsymbol{n}_l \, \mathrm{d}s, \tag{5.12}$$

depends on the mass transferred into the domain $\mathscr{D}_l$. Applying the pressure condition (5.5) expresses the divergence of flux within the blood,

$$\frac{\partial q_b}{\partial x} = -\int_{\Gamma_b} K(\Delta p - \Delta\Pi) \, \mathrm{d}s = -\mathcal{K}(\Delta p - \Delta\Pi), \tag{5.13}$$

in terms of the fluid and osmotic pressure jump across the membrane, and the total effective membrane hydraulic conductivity, given by

$$\mathcal{K} = \int_{\Gamma_b} K \, \mathrm{d}s = \begin{cases} 2\pi r_b K & \text{(axisymmetric)}, \\ \\ WK & \text{(two-dimensional)}. \end{cases} \tag{5.14}$$

To derive a similar equation for the divergence of flux within the dialysate, we additionally impose the no-penetration boundary condition (5.6) and find that

$$\frac{\partial q_d}{\partial x} = -\int_{\partial \mathscr{D}_d} \boldsymbol{v}_d \cdot \boldsymbol{n}_d \, \mathrm{d}s = -\int_{\Gamma_d} \boldsymbol{v}_d \cdot \boldsymbol{n}_d \, \mathrm{d}s + \int_{\Gamma_b} K(\Delta p - \Delta\Pi) \, \mathrm{d}s = \mathcal{K}(\Delta p - \Delta\Pi). \tag{5.15}$$

Therefore, the total flux is conserved – that is,

$$\frac{\partial q_b}{\partial x} + \frac{\partial q_d}{\partial x} = 0. \tag{5.16}$$

Integrating once in x gives that the total flux is uniform,

$$q_b + q_d = a, \tag{5.17}$$

where a is a function of time t only, which can be determined by applying appropriate boundary conditions at either end of the dialyser.

We eliminate pressure by differentiating the global mass conservation equation (5.13) and using the relationships (5.11a) and (5.11b) between flux and pressure to obtain the equation

$$\frac{\partial^2 q_b}{\partial x^2} = \mathcal{K}\left(\mathcal{R}_b q_b - \mathcal{R}_d q_d + \frac{\partial(\Delta\Pi)}{\partial x}\right), \tag{5.18a}$$

for the fluid flux within the blood and

$$\frac{\partial^2 q_d}{\partial x^2} = -\mathcal{K}\left(\mathcal{R}_b q_b - \mathcal{R}_d q_d + \frac{\partial(\Delta\Pi)}{\partial x}\right), \tag{5.18b}$$

within the dialysate.

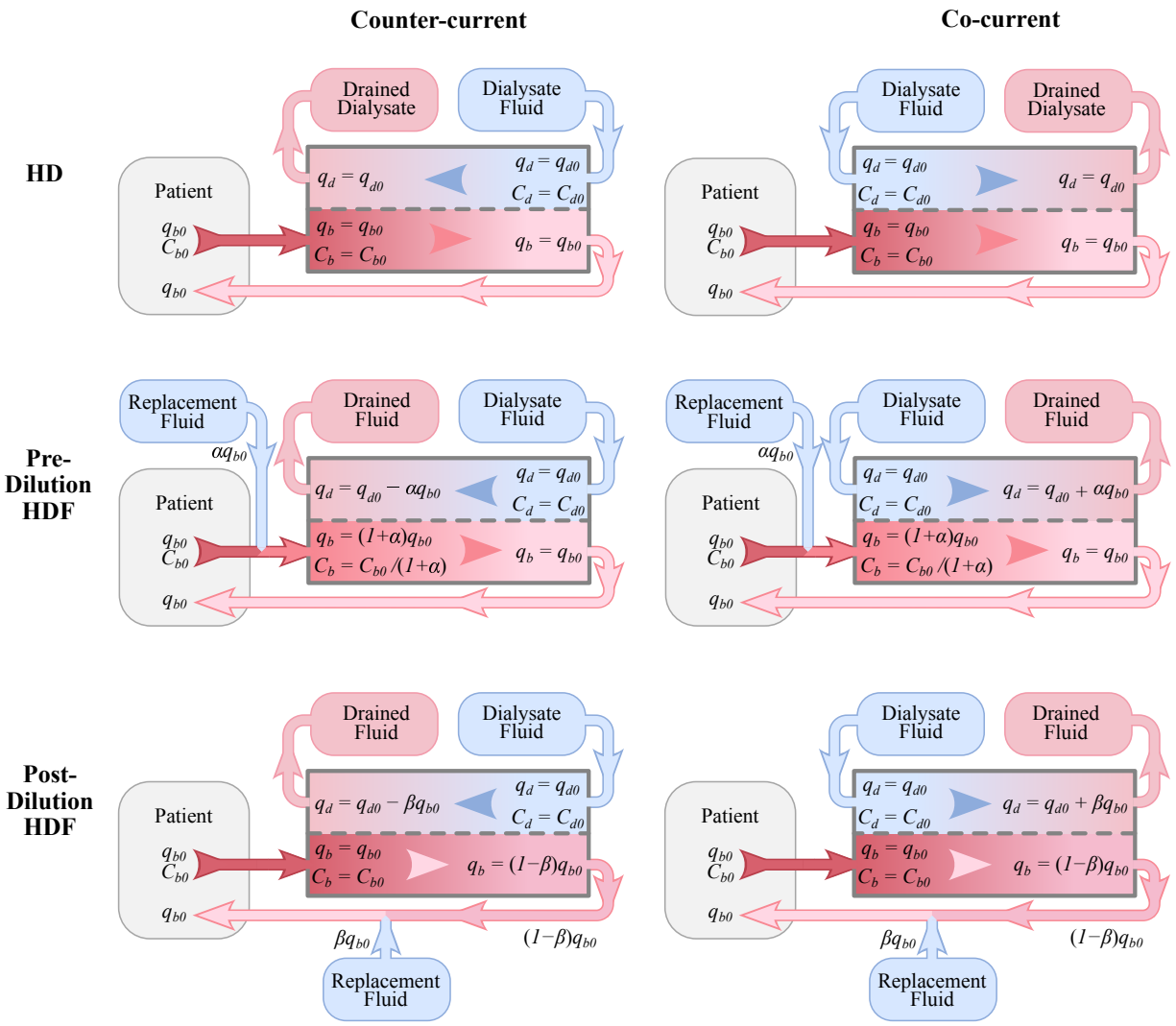

Figure 5.3: Schematics depicting the inlet and outlet flows and the inlet concentrations for blood and dialysate for HD ($\alpha = \beta = 0$), pre-dilution HDF ($\beta = 0$) and post-dilution HDF ($\alpha = 0$) under counter-current and co-current configurations.

5.3.2 Fluid flow in HDF

Boundary conditions reflecting mixed pre-dilution and post-dilution HDF are given by

$$q_b = (\alpha+1)q_{b0} \quad \text{and} \quad q_d = q_{d0} - q_{b0}(\alpha+\beta) \quad \text{at } x = 0, \tag{5.19a}$$

$$q_b = (1-\beta)q_{b0} \quad \text{and} \quad q_d = q_{d0} \quad \text{at } x = L, \tag{5.19b}$$

giving $a = (1-\beta)q_{b0} + q_{d0}$, for counter-current flow, and

$$q_b = (\alpha+1)q_{b0} \quad \text{and} \quad q_d = q_{d0} \quad \text{at } x = 0, \tag{5.19c}$$

$$q_b = (1-\beta)q_{b0} \quad \text{and} \quad q_d = q_{d0} + (\alpha+\beta)q_{b0} \quad \text{at } x = L, \tag{5.19d}$$

giving $a = (1+\alpha)q_{b0} + q_{d0}$, for co-current flow. As shown in Figure 5.3, the limit $\beta = 0$ corresponds to pre-dilution HDF and $\alpha = 0$ corresponds to post-dilution HDF. Note that the boundary conditions for counter-current and co-current flow are equivalent when $\alpha = \beta = 0$.

5.3.3 Fluid flux

Solving for the fluid flux gives

$$q_b = q_{b0}\frac{\cosh(\gamma(x/L-1/2))}{\cosh(\gamma/2)} + q_{b,\text{conv}} + q_{b,\text{pre}} + q_{b,\text{post}}, \tag{5.20a}$$

$$q_d = \begin{cases} (1-\beta)q_{b0} + q_{d0} - q_b & \text{(counter-current)}, \\ (1+\alpha)q_{b0} + q_{d0} - q_b & \text{(co-current)}, \end{cases} \tag{5.20b}$$

where

$$q_{b,\text{conv}} = \frac{q_{b0}+q_{d0}}{1+\mathcal{R}_b/\mathcal{R}_d}\left(1 - \frac{\sinh(\gamma x/L) + \sinh(\gamma(1-x/L))}{\sinh(\gamma)}\right) + \mathcal{K}\int_0^L G(x,\xi)\frac{\partial \Delta\Pi}{\partial \xi}\,\mathrm{d}\xi, \tag{5.20c}$$

is the convective contribution owing to flow across the membrane with the integral term reflecting flow owing to a jump in osmotic pressure,

$$q_{b,\text{pre}} = \begin{cases} \alpha q_{b0}\dfrac{\sinh(\gamma(1-x/L))}{\sinh(\gamma)} & \text{(counter-current)}, \\ \alpha q_{b0}\dfrac{1}{1+\mathcal{R}_b/\mathcal{R}_d}\left(\dfrac{\mathcal{R}_b}{\mathcal{R}_d}\dfrac{\sinh(\gamma(1-x/L))}{\sinh(\gamma)} - \dfrac{\sinh(\gamma x/L)}{\sinh(\gamma)} + 1\right) & \text{(co-current)}, \end{cases} \tag{5.20d}$$

is the contribution owing to pre-dilution HDF and

$$q_{b,\text{post}} = \begin{cases} \dfrac{\beta q_{b0}}{1+\mathcal{R}_b/\mathcal{R}_d}\left(\dfrac{\sinh(\gamma(1-x/L))}{\sinh(\gamma)} - \dfrac{\mathcal{R}_b\sinh(\gamma x/L)}{\mathcal{R}_d\sinh(\gamma)} - 1\right) & \text{(counter-current)}, \\ -\beta q_{b0}\dfrac{\sinh(\gamma x/L)}{\sinh(\gamma)} & \text{(co-current)}, \end{cases} \tag{5.20e}$$

is the contribution owing to post-dilution HDF. Here, $\gamma = L\sqrt{\mathcal{K}(\mathcal{R}_b+\mathcal{R}_d)}$ and the Green's function G is given by

$$G(x,\xi) = \begin{cases} \dfrac{L\sinh(\gamma(\xi/L-1))\sinh(\gamma x/L)}{\gamma\sinh(\gamma)} & \text{for } x < \xi, \\ \dfrac{L\sinh(\gamma\xi/L)\sinh(\gamma(x/L-1))}{\gamma\sinh(\gamma)} & \text{for } x > \xi. \end{cases} \tag{5.21}$$

In deriving the solution (5.20) for q_b, we applied the boundary conditions $q_b = q_{b0}$ at $x = 0, L$. We note that while q_{b0} is constant in typical medical settings, the prefactor a, appearing in

the second term on the right-hand side of (5.20), may vary in time if the dialysate is delivered time-dependently.

5.3.4 Membrane fluid flux

In coupling fluid flow to solute transport, it is instructive to express the total flux V_m of fluid through the membrane in terms of the fluid flux along the fibre q_b and q_d, the former of which features in the bulk solute transport equations of §5.4. Explicitly, the total membrane fluid flux per unit axial length is defined by

$$V_m = \int_{\Gamma_b} v_m \, \mathrm{d}s = \mathcal{K}(\Delta p - \Delta\Pi) = \begin{cases} 2\pi r_b v_m & \text{(axisymmetric)}, \\ W v_m & \text{(two-dimensional)}, \end{cases} \tag{5.22}$$

where v_m is the Darcy velocity through the membrane. Applying continuity of velocity at the membrane boundary Γ_b on the side of the blood relates the total membrane fluid flux per unit length to the transmembrane velocity at the membrane, as given by the first equality in the equation

$$V_m = \begin{cases} 2\pi r_b v_m = \dfrac{\pi r_b^4}{8} \dfrac{\partial^2 p_b}{\partial x^2} = -\dfrac{\partial q_b}{\partial x} & \text{(axisymmetric)}, \\ W v_m = \dfrac{W h_b^3}{3} \dfrac{\partial^2 p_b}{\partial x^2} = -\dfrac{\partial q_b}{\partial x} & \text{(two-dimensional)}. \end{cases} \tag{5.23}$$

To derive the remaining equalities in (5.23), we apply the expression (5.9) for the transmembrane velocity within the blood in terms of the pressure gradient and the expression (5.11) for the flux in terms of pressure gradient. Equation (5.23) explicitly relates the membrane fluid flux per unit length to the divergence of flux, thus coupling fluid flow to solute transport as required in §5.4.

5.3.5 Ultrafiltration

The permeability k of the fibre membrane and the total effective membrane hydraulic conductivity $\mathcal{K}$ are often expressed in the dialyser manufacturing industry in terms of the ultrafiltration coefficient K_{uf} – a parameter more commonly used in practice. The ultrafiltration coefficient quantifies how easily fluid passes through a dialyser membrane under a pressure gradient. In particular, it quantifies the ratio between the total filtration flux J_{uf} and the pressure difference across the membrane, and is a key parameter for characterizing the performance of a dialyser. Explicitly, the ultrafiltration form of Darcy's law reads

$$J_{uf} = K_{uf} \langle \Delta p - \Delta\Pi \rangle \tag{5.24}$$

where $\langle \cdot \rangle = L^{-1} \int_0^L \cdot \, \mathrm{d}x$ denotes the average along the length of the dialyser.

To determine the ultrafiltration coefficient K_{uf} in terms of the measures of membrane per-

meability described above, we relate the total dialyser filtration flux J_{uf} to the total membrane fluid flux V_m per unit length and per fibre, as

$$J_{uf} = NL\langle V_m \rangle, \tag{5.25}$$

where N is the number of fibres in the dialyser. Comparing the ultrafiltration form of the Darcy law (5.24) to the membrane Darcy law (5.22) relates the ultrafiltration coefficient K_{uf} to the total effective membrane hydraulic conductivity $\mathcal{K}$ via

$$K_{uf} = \mathcal{K}NL = \begin{cases} 2\pi r_b KNL & \text{(axisymmetric)}, \\ \\ WKNL & \text{(two-dimensional)}. \end{cases} \tag{5.26}$$

5.4 Solute transport

We denote the concentration of solute by C_l, i.e. the mass of solute per unit volume, where the subscript $l = b$ and $l = d$ reflects quantities evaluated within the blood and dialysate, respectively. The transport of solute within the blood and dialysate satisfy the advection-diffusion equations

$$\frac{\partial C_l}{\partial t} + \frac{\partial (u_l C_l)}{\partial x} + \nabla \cdot (\boldsymbol{v}_l C_l) = D_l \frac{\partial^2 C_l}{\partial x^2} + D_l \nabla^2 C_l, \tag{5.27}$$

reflecting both advection with the flow and diffusion with solute diffusivity D_l. While complete, the three-dimensional advection-diffusion equation is computationally expensive to solve. We, therefore, integrate this equation across the blood and dialysate to obtain a reduced set of bulk solute transport equations that capture the dominant transport mechanisms in §5.4.1. These bulk equations depend upon the bulk solute transport through the membrane, which we model in §5.4.2. We use the bulk solute flux through the membrane, determined in §5.4.2, to formulate the bulk solute transport equations explicitly in §5.4.3.

5.4.1 Bulk solute transport

Integrating the advection-diffusion equation (5.27) for the concentration across the cross-section $\mathscr{D}_l$ and noting that $\mathscr{D}_l$ is independent of x and t gives rise to

$$\frac{\partial}{\partial t}\int_{\mathscr{D}_l} C_l \,\mathrm{d}A + \frac{\partial}{\partial x}\int_{\mathscr{D}_l} u_l C_l \,\mathrm{d}A = D_l \frac{\partial^2}{\partial x^2}\int_{\mathscr{D}_l} C_l \,\mathrm{d}A - \int_{\mathscr{D}_l} \nabla \cdot \boldsymbol{j}_l \,\mathrm{d}A, \tag{5.28}$$

in terms of the local solute flux, with the contribution from radial convective transport excluded

$$\boldsymbol{j}_l = \boldsymbol{v}_l C_l - D_l \nabla C_l. \tag{5.29}$$

Applying the two-dimensional divergence theorem gives rise to

$$\frac{\partial}{\partial t}\int_{\mathscr{D}_l} C_l \,\mathrm{d}A + \frac{\partial}{\partial x}\int_{\mathscr{D}_l} u_l C_l \,\mathrm{d}A = D_l \frac{\partial^2}{\partial x^2}\int_{\mathscr{D}_l} C_l \,\mathrm{d}A - \int_{\partial\mathscr{D}_l} \boldsymbol{j}_l \cdot \boldsymbol{n}_l \,\mathrm{d}s, \tag{5.30}$$

where $\boldsymbol{n}_l$ is the unit outwards normal vector.

We now assume that C_l is uniform across $\mathscr{D}_l$ (Villarroel *et al.*, 1977), so that

$$A_l \frac{\partial C_l}{\partial t} + \frac{\partial (C_l q_l)}{\partial x} = D_l A_l \frac{\partial^2 C_l}{\partial x^2} - J_l, \tag{5.31}$$

in terms of the membrane solute flux

$$J_l = \int_{\partial\mathscr{D}_l} \boldsymbol{j}_l \cdot \boldsymbol{n}_l \,\mathrm{d}s, \tag{5.32}$$

the fluid flux

$$q_l = \int_{\mathscr{D}_l} u_l \,\mathrm{d}A = -\mathcal{R}_l^{-1} \frac{\partial p_l}{\partial x}, \tag{5.33}$$

and the surface area

$$A_l = \int_{\mathscr{D}_l} \mathrm{d}A. \tag{5.34}$$

This equation is identical to the one-dimensional theory of haemodialyser in the previous literature (Waniewski, 2006; Jaffrin *et al.*, 1981),

We now need to determine J_l and to do so, we need to solve for the concentration C_l in the membrane by integrating the three-dimensional conservation equation across the membrane.

5.4.2 Fluid and solute transport within the membrane

We now account for the finite thickness of the membrane; that is, the membrane is treated as a volumetric domain rather than an infinitesimal surface. The Darcy velocity $\boldsymbol{v}_m$ and the solute flux $\boldsymbol{j}_m$ are therefore defined as fields within the membrane domain, which occupies $x \in [x_b, x_m]$ in the two-dimensional geometry and $r \in [r_b, r_m]$ in the axisymmetric geometry, respectively. All quantities within the membrane are assumed to be independent of the axial coordinate, and hence the axial fluid flux and axial solute flux are zero. Here, we derive an expression for solute transport across the membrane that involves the transmembrane fluid flux and the solute concentrations on the blood and dialysate sides.

We model the membrane as a porous medium of local permeability k so that the velocity field is governed by Darcy's law

$$\boldsymbol{v}_m = -\frac{k}{\mu}\left(\nabla p - \nabla \Pi\right), \tag{5.35}$$

where

$$\Pi = \sigma RTC_m, \tag{5.36}$$

is the osmotic pressure within the membrane. Here, σ is the reflection coefficient (Waniewski, 2006), R is the gas constant and T is the temperature. The value of σ depends on the properties of the molecule and membrane. When $\sigma = 1$, all molecules are reflected from the membrane; when $\sigma = 0$, all molecules pass through the membrane. We may thus refer to $1-\sigma$ as the sieving coefficient. The quantity $\boldsymbol{v}_m$ refers to the Darcy velocity, or the volumetric flow rate per cross sectional area (including the solid and pores). As such, the interstitial velocity is, in general, larger, and given by $\boldsymbol{v}_m/\phi$, where ϕ is the porosity of the membrane. Darcy's law (5.35) is supplemented by the incompressibility condition

$$\nabla \cdot \boldsymbol{v}_m = 0. \tag{5.37}$$

The solute flux through the membrane is given by

$$\boldsymbol{j}_m = (1-\sigma)\boldsymbol{v}_m C_m - \phi D_m \nabla C_m, \tag{5.38}$$

In general, the solute satisfies the conservation equation

$$\phi \frac{\partial C_m}{\partial t} + \nabla \cdot \boldsymbol{j}_m = 0, \tag{5.39}$$

though it is common to assume that the flow through the membrane is in hydrodynamic equilibrium, so that

$$\nabla \cdot \boldsymbol{j}_m = 0. \tag{5.40}$$

When the membrane thickness δ is small, it is instructive to integrate the three-dimensional equations (5.37) (5.40) across the membrane, subject to the boundary conditions

$$C_m = C_b \quad \text{at} \quad \boldsymbol{r} = \boldsymbol{r}_b \quad \text{and} \quad C_m = C_d \quad \text{at} \quad \boldsymbol{r} = \boldsymbol{r}_m, \tag{5.41}$$

where $\boldsymbol{r} = \boldsymbol{r}_b$ and $\boldsymbol{r} = \boldsymbol{r}_m$ refers to the membrane boundary on the side of the blood and dialysate, respectively. We do so in the axisymmetric and two-dimensional geometries in the following sections.

Axisymmetric geometry

In the axisymmetric geometry, the Darcy velocity and solute flux are in the radial direction, so that

$$\boldsymbol{v}_m = v_m \boldsymbol{e}_r \quad \text{and} \quad \boldsymbol{j}_m = j_m \boldsymbol{e}_r \tag{5.42}$$

where

$$v_m = -\frac{k}{\mu}\left(\frac{\partial p}{\partial r} - \frac{\partial \Pi}{\partial r}\right) \quad \text{and} \quad j_m = (1-\sigma)v_m C_m - \phi D_m \frac{\partial C_m}{\partial r}. \tag{5.43}$$

The quasi-steady conservation equations (5.37) and (5.40) become

$$\frac{1}{r}\frac{\partial (r v_m)}{\partial r} = 0 \quad \text{and} \quad \frac{1}{r}\frac{\partial (r j_m)}{\partial r} = 0. \tag{5.44}$$

Integrating in r gives that the total flux of fluid and solute through the membrane per unit axial length,

$$V_m = 2\pi r v_m \quad \text{and} \quad J_m = 2\pi r j_m, \tag{5.45}$$

respectively, are uniform in $r \in [r_b, r_m]$.

We note that the total membrane solute flux J_m is equal to the total solute flux J_b from the blood into the membrane, since

$$J_b = \int_{\partial \mathscr{D}_b} \boldsymbol{j}_b \cdot \boldsymbol{n}_b \, \mathrm{d}s = \int_{\partial \mathscr{D}_b} \boldsymbol{j}_m \cdot \boldsymbol{n}_b \, \mathrm{d}s = \int_0^{2\pi} r j_m \, \mathrm{d}\theta = 2\pi r j_m = J_m, \tag{5.46}$$

and is equal in magnitude and opposite in sign to the total solute flux J_d from the dialysate into the membrane, since

$$J_d = \int_{\partial \mathscr{D}_d} \boldsymbol{j}_d \cdot \boldsymbol{n}_d \, \mathrm{d}s = \int_{\partial \mathscr{D}_d} \boldsymbol{j}_m \cdot \boldsymbol{n}_d \, \mathrm{d}s = -\int_0^{2\pi} r j_m \, \mathrm{d}\theta = -2\pi r j_m = -J_m. \tag{5.47}$$

Here, we have used that $r j_m$ is independent of r and that $\boldsymbol{n}_l$ is the outward normal to $\mathscr{D}_l$, so that $\boldsymbol{n}_b = \boldsymbol{e}_r$ and $\boldsymbol{n}_d = -\boldsymbol{e}_r$. We have also applied the solute flux continuity conditions

$$\boldsymbol{j}_b \cdot \boldsymbol{n}_b = \boldsymbol{j}_m \cdot \boldsymbol{n}_b = j_m \quad (\text{at } r = r_b) \quad \text{and} \quad \boldsymbol{j}_d \cdot \boldsymbol{n}_d = \boldsymbol{j}_m \cdot \boldsymbol{n}_d = -j_m \quad (\text{at } r = r_m). \tag{5.48}$$

Next, we determine an explicit expression for the total membrane solute flux J_m. To this end, we first solve for the solute concentration field C_m within the membrane. Multiplying both sides of the second equation in (5.43) by $2\pi r$ yields

$$J_m = (1-\sigma)\, V_m C_m - 2\pi \phi D_m \, r \frac{\partial C_m}{\partial r}. \tag{5.49}$$

Differentiating both sides with respect to r gives

$$0 = (1-\sigma)\, V_m \frac{\partial C_m}{\partial r} - \frac{\partial}{\partial r}\left(2\pi \phi D_m \, r \frac{\partial C_m}{\partial r}\right), \tag{5.50}$$

subject to boundary conditions obtained by reduction of (5.41).

$$C_m = C_b \quad \text{at} \quad r = r_b \quad \text{and} \quad C_m = C_d \quad \text{at} \quad r = r_m, \tag{5.51}$$

giving the solution

$$C_m = C_b - (C_b - C_d)\frac{1-(r/r_b)^{\lambda V_m/2\pi\delta}}{1-(r_m/r_b)^{\lambda V_m/2\pi\delta}}, \tag{5.52}$$

where

$$\lambda = \frac{(1-\sigma)\delta}{\phi D_m} \quad \text{and} \quad \delta = r_m - r_b. \tag{5.53}$$

The latter of these constants is the membrane thickness.

The local solute flux j_m, as defined by (5.43), and total solute flux J_m, as defined by (5.45), can now be evaluated explicitly as

$$j_m = \frac{D}{2\pi r}(C_b - C_d) + \frac{(1-\sigma)V_m}{2\pi r}\left[(1-F)C_b + FC_d\right], \tag{5.54}$$

and

$$J_m = D(C_b - C_d) + (1-\sigma)V_m\left[(1-F)C_b + FC_d\right], \tag{5.55}$$

or, alternatively,

$$J_m = D\Big((C_b - C_d) + Pe\left[(1-F)C_b + FC_d\right]\Big) \tag{5.56}$$

where

$$F = f((1-\sigma)V_m/D) \quad \text{and} \quad f(Pe) = \frac{1}{Pe} - \frac{1}{e^{Pe}-1} \tag{5.57}$$

in terms of the effective membrane diffusivity

$$D = \frac{2\pi\phi D_m}{\log(1+\delta/r_b)}. \tag{5.58}$$

The quantity $Pe = (1-\sigma)V_m/D$ is a dynamic Peclet number, which characterises the importance of advection relative to diffusion in the transport of solute across the membrane. The first term on the right-hand side of (5.55) reflects diffusive transport across the membrane, proportional to the difference in concentration either side of the membrane. The second term on the right-hand side of (5.55) reflects convective transport across the membrane, proportional to the total fluid flux V_m and the effective membrane concentration

$$\bar{C}_m = (1-F)C_b + FC_d. \tag{5.59}$$

In the limit $Pe \ll 1$, advective transport is much less significant than diffusive transport across the membrane and $F \to 1/2$. Therefore, the effective membrane concentration,

$$\bar{C}_m = \frac{1}{2}(C_b + C_d), \tag{5.60}$$

is the average of the blood and dialysate concentrations, reflecting that the membrane concentration is determined equally by the concentration either side of the membrane.

In the limit $Pe \gg 1$, we have $F \to 0$ when $V_m > 0$ and $F \to 1$ when $V_m < 0$ so that the

effective membrane concentration takes the value of the concentration from the upstream side of the membrane. Explicitly,

$$\bar{C}_m = \begin{cases} C_b & \text{if } V_m > 0 \\ C_d & \text{if } V_m < 0 \end{cases}, \tag{5.61}$$

reflecting that the membrane concentration is determined entirely by the concentration of the fluid advected with the flow.

In the limit $\delta \ll r_b$, we have $\log(r_m/r_b) \sim \delta/r_b$ and $Pe \sim \lambda v_m$, which reduces (5.54) to

$$j_m = \frac{\phi D_m}{\delta}(C_b - C_d) + (1-\sigma)v_m\left[(1-F)C_b + FC_d\right], \tag{5.62}$$

where $F = f(\lambda v_m)$ and now v_m is understood to be evaluated at $r = r_b$. Equation (5.62) is equivalent to the corresponding result (5.72) when the membrane if flat, which we derive in the two-dimensional geometry in §5.4.2.

We derive the effective Darcy-type boundary condition (5.5) for the transmembrane fluid velocity v_b and v_d either side of the membrane by integrating the equation (5.45) relating the transmembrane velocity v_m to the total fluid flux V_m. In particular, integrating the radial velocity v_m through the membrane yields

$$\int_{r_b}^{r_m} \frac{1}{2\pi r} V_m \, \mathrm{d}r = -\frac{k}{\mu}(p - \Pi)\Big|_{r_b}^{r_m}, \tag{5.63}$$

which reduces to

$$V_m = \frac{2\pi k}{\mu \log(r_m/r_b)}(\Delta p - \Delta\Pi), \tag{5.64}$$

where $\Delta p = p|_{r_b} - p|_{r_m}$ and $\Delta\Pi = \Pi|_{r_b} - \Pi|_{r_m}$. In the limit $\delta \ll r_b$, we have $\log(r_m/r_b) = \log(1 + \delta/r_b) \sim \delta/r_b$ and $V_m = 2\pi r_b v_b = 2\pi r_b v_d$, which yields the effective membrane Darcy law

$$v_b = v_d = K(\Delta p - \Delta\Pi), \tag{5.65}$$

where

$$K = \frac{k}{\mu\delta}. \tag{5.66}$$

The membrane Darcy law (5.65) is an integrated version of Darcy's law that has been used in §5.3 as a boundary condition for the radial velocity either side of the membrane.

Two-dimensional geometry

For completeness, we solve for the concentration, and thus for the solute flux within the membrane, in the two-dimensional geometry and compare with the equivalent results in the axisymmetric geometry. The Darcy velocity and solute flux are in the positive y-direction in the two-

dimensional geometry, so that

$$\boldsymbol{v}_m = v_m \boldsymbol{e}_y \quad \text{and} \quad \boldsymbol{j}_m = j_m \boldsymbol{e}_y \tag{5.67}$$

where

$$v_m = -\frac{k}{\mu}\left(\frac{\partial p}{\partial y} - \frac{\partial \Pi}{\partial y}\right) \quad \text{and} \quad j_m = (1-\sigma) v_m C_m - \phi D_m \frac{\partial C_m}{\partial y}. \tag{5.68}$$

The quasi-steady conservation equations (5.37) and (5.40) become

$$\frac{\partial v_m}{\partial y} = 0 \quad \text{and} \quad \frac{\partial j_m}{\partial y} = 0, \tag{5.69}$$

and so v_m and j_m are independent of y. The boundary conditions (5.41) reduce to

$$C_m = C_b \quad \text{at} \quad y = y_b \quad \text{and} \quad C_m = C_d \quad \text{at} \quad y = y_m, \tag{5.70}$$

Integrating in y yields the solution

$$C_m = C_b - (C_b - C_d)\frac{1 - \exp(\lambda v_m (y - y_b)/\delta)}{1 - \exp(\lambda v_m)} \tag{5.71}$$

where λ is defined in (5.53) and $\delta = y_m - y_b$. The local solute flux (5.68) can now be evaluated explicitly as (Waniewski, 2006; Villarroel *et al.*, 1977)

$$j_m = \frac{\phi D_m}{\delta}(C_b - C_d) + (1-\sigma) v_m \left[(1-F)C_b + F C_d\right], \tag{5.72}$$

where $F = f(Pe)$ and

$$Pe = \lambda v_m = \frac{(1-\sigma)\delta v_m}{\phi D_m} = \frac{(1-\sigma)\delta V_m}{W \phi D_m} = \frac{(1-\sigma) V_m}{D}, \tag{5.73}$$

in terms of the effective two-dimensional membrane diffusivity

$$D = \frac{\phi D_m W}{\delta}, \tag{5.74}$$

which agrees with the equivalent result in the axisymmetric geometry when the membrane is sufficiently thin. Here, W is the width (in the z-direction) of the membrane and $V_m = W v_m$ is the total fluid flux. Equation (5.72) has been derived previously in the literature, for example in Waniewski (2006). The total membrane solute flux J_m is given by

$$J_m = W j_m = D(C_b - C_d) + (1-\sigma) V_m \left[(1-F)C_b + F C_d\right]. \tag{5.75}$$

Similarly to equivalent results in the axisymmetric geometry, it can be shown that

$$J_m = J_b = -J_d. \tag{5.76}$$

One can derive the membrane Darcy law by following similar arguments to those used in deriving the axisymmetric equivalent (5.65). In particular, integrating the transmembrane velocity given by Darcy's law (5.68) across the membrane, and using that the transmembrane velocity v_m is independent of y as given by (5.69), directly yields the same membrane Darcy law as the axisymmetric equivalent (5.65).

5.4.3 Explicit bulk solute transport equation

Equations governing solute transport are coupled to the fluid flow through the equation (5.23) relating the total membrane fluid flux V_m to the gradient $\partial q_b/\partial x$ of the axial flux of blood. Equation (5.23) also feeds in to the definition of the membrane Peclet number Pe through (5.57), thus determining the effective membrane concentration (5.59) appearing as a term describing the total membrane solute flux J_m (5.55). The total membrane solute flux J_m is, therefore, fully determined in terms of the fluid flow and solute concentration either side of the membrane.

Using (5.46), (5.47) and (5.76), which relate the total solute flux within the blood and dialysate to that within the membrane, and the explicit expressions (5.55) and (5.75) for the total membrane solute flux in the axisymmetric and two-dimensional geometries, respectively, the depth-integrated concentration equations (5.31) reduce to

$$A_b\frac{\partial C_b}{\partial t} + \frac{\partial (C_b q_b)}{\partial x} = D_b A_b \frac{\partial^2 C_b}{\partial x^2} - J_m, \tag{5.77}$$

$$A_d\frac{\partial C_d}{\partial t} + \frac{\partial (C_d q_d)}{\partial x} = D_d A_d \frac{\partial^2 C_d}{\partial x^2} + J_m. \tag{5.78}$$

5.5 Summary of governing equations

For convenience, we summarise the key depth-integrated equations in this section. The fluid flow is governed by the mass conservation equations

$$\frac{\partial^2 q_b}{\partial x^2} = \mathcal{K}\left(\mathcal{R}_b q_b - \mathcal{R}_d q_d + \frac{\partial(\Delta\Pi)}{\partial x}\right), \tag{5.79a}$$

$$\frac{\partial^2 q_d}{\partial x^2} = -\mathcal{K}\left(\mathcal{R}_b q_b - \mathcal{R}_d q_d + \frac{\partial(\Delta\Pi)}{\partial x}\right), \tag{5.79b}$$

within the blood and dialysate, respectively, where

$$\mathcal{K} = \begin{cases} 2\pi r_b K = \dfrac{2\pi r_b k}{\mu\delta} & \text{(axisymmetric)}, \\ WK = \dfrac{Wk}{\mu\delta} & \text{(two-dimensional)}, \end{cases} \tag{5.79c}$$

$$\Delta\Pi = \Pi_b - \Pi_d = \sigma RT(C_b - C_d), \tag{5.79d}$$

$$\mathcal{R}_b = \begin{cases} \dfrac{8\mu}{\pi r_b^4}, \\ \dfrac{3\mu}{Wh_b^3}, \end{cases} \qquad \mathcal{R}_d = \begin{cases} \dfrac{8\mu}{\pi}\left[4r_b^2 r_d^2 - r_b^4 - 3r_d^4 - 4r_d^4 \log\left(\dfrac{r_b}{r_d}\right)\right]^{-1} & \text{(axisymmetric)}, \\ \dfrac{3\mu}{W(h_b - h_d)^3} & \text{(two-dimensional)}. \end{cases} \tag{5.79e}$$

The concentration within the blood and dialysate satisfies the bulk advection-diffusion equations

$$A_b \frac{\partial C_b}{\partial t} + \frac{\partial (C_b q_b)}{\partial x} = D_b A_b \frac{\partial^2 C_b}{\partial x^2} - J_m, \tag{5.80a}$$

$$A_d \frac{\partial C_d}{\partial t} + \frac{\partial (C_d q_d)}{\partial x} = D_d A_d \frac{\partial^2 C_d}{\partial x^2} + J_m. \tag{5.80b}$$

where

$$A_b = \begin{cases} \pi r_b^2, \\ Wh_b, \end{cases} \qquad A_d = \begin{cases} \pi r_d^2 - \pi(r_b + \delta)^2 & \text{(axisymmetric)}, \\ W(h_d - h_b - \delta) & \text{(two-dimensional)}, \end{cases} \tag{5.80c}$$

and the total membrane solute flux is given by

$$J_m = D(C_b - C_d) + (1 - \sigma) V_m \left[(1 - F)C_b + FC_d\right], \tag{5.80d}$$

in terms of

$$F = f((1 - \sigma)V_m / D) \quad \text{where} \quad f(Pe) = \frac{1}{Pe} - \frac{1}{e^{Pe} - 1}, \tag{5.80e}$$

and

$$D = \begin{cases} \dfrac{2\pi\phi D_m}{\log(1 + \delta/r_b)}, \\ \dfrac{\phi D_m W}{\delta}, \end{cases} \qquad V_m = \begin{cases} 2\pi r v_m = -\dfrac{\partial q_b}{\partial x} & \text{(axisymmetric)}, \\ W v_m = -\dfrac{\partial q_b}{\partial x} & \text{(two-dimensional)}. \end{cases} \tag{5.80f}$$

For the fluid flow, the boundary conditions are

$$q_b = q_{b0} \quad \text{and} \quad q_d = q_{d0} \quad \text{at } x = 0, L, \tag{5.81a}$$

for HD and (5.19) for HDF. For solute transport, the boundary conditions are

$$C_b = \frac{C_{b0}}{1+\alpha} \quad \text{at } x = 0 \quad \text{and} \quad C_d = C_{d0} \quad \text{at } x = \begin{cases} L & \text{(counter-current)}, \\ 0 & \text{(co-current)}, \end{cases} \tag{5.81b}$$

with the final boundary condition on C_d being evaluated at either the right or left endpoint depending on whether the flows of blood and dialysate are counter-current or co-current, respectively. Henceforth, we perform calculations in the axisymmetric geometry only.

5.6 Model Reduction

In this section, we outline the key assumptions made in reducing the full mathematical model for fluid flow and solute transport.

5.6.1 Osmotic pressure

We neglect the osmotic pressure terms in the fluid mass conservation equations (5.79a) and (5.79b) to simplify the model. This decouples the fluid flow equations (5.79a) and (5.79b) from the bulk solute transport equations (5.80a) and (5.80b) and significantly simplifies the analysis.

This assumption is justified when the molecular weight of the solute is small (i.e., the reflection coefficient σ is relatively small). From the fluid flow equations (5.79a)–(5.79b) and the definition of osmotic pressure in (5.79d), we find that the osmotic pressure term becomes negligible when

$$\frac{\sigma RT[C]}{[x][\mathcal{R}][q]} \ll 1, \tag{5.82}$$

where $[\cdot]$ denotes the typical value of a quantity: $[C]$ is the typical solute concentration, $[q]$ is the typical volumetric flux, and $[\mathcal{R}]$ represents the typical hydraulic resistance. Under this condition, the contribution of osmotic pressure is sufficiently small to be omitted from the fluid flow equations.

A rough order-of-magnitude calculation can be used to verify this assumption. We consider β_2-microglobulin, a representative middle-molecular-weight uremic toxin in dialysis. According to the Braun Diacap® Pro 19H dialyser manual, the reflection coefficient for this solute is approximately $\sigma = 0.3$. The typical blood concentration of β_2-microglobulin in chronic kidney disease patients is about 60 $\mathrm{mg\,L^{-1}}$ (Dung *et al.*, 2019). With a molecular weight of 11,800 Da, this corresponds to a concentration

$$[C] \approx \frac{60}{11{,}800}\ \mathrm{mol\,m^{-3}}.$$

Using the gas constant $R = 8.31\ \mathrm{J\,mol^{-1}\,K^{-1}}$, room temperature $T = 300$ K, characteristic length

scale $[x] = 0.26$ m, characteristic hydraulic resistance $[\mathcal{R}] = |\mathcal{R}_b| \approx 1 \times 10^{14}$ m^{-4}Pa s (with $\mu = \mu_b$), and a typical flux $[q] = 0.034$ ml/min, the left-hand side of inequality (5.82) evaluates to approximately $2.6 \times 10^{-4} \ll 1$. This confirms that the assumption is satisfied under physiologically relevant conditions, at least when a single representative toxin is considered. In practice, the full system involves the transport of multiple solutes, and the validity of this assumption in that more general setting would need to be assessed carefully.

5.6.2 Diffusive solute transport along the fibre

While retaining diffusive transport across the fibre membrane, we neglect diffusive transport along the fibre, given by the diffusive term $D_l A_l \partial^2 C_l / \partial x^2$ in (5.80a)-(5.80b), based on the relative magnitude of convective and diffusive transport in the x-direction.

To justify this, we nondimensionalize the bulk solute transport equations (5.80a)-(5.80b) and find that the advective term is of order $[C][q]/[x]$ and the diffusive term is of order $D_l A_l [C][x]^2$. Computing the Peclet number (advection divided by diffusion) for both the blood and the dialysate yields

$$\mathrm{Pe}_l = \frac{[q][x]}{D_l A_l}. \tag{5.83}$$

Using the typical values from Table 5.1, $[q] = 0.034$ ml/min, $[x] = 0.26$ m, $A_l \sim \mathcal{O}(10^{-8})$ m^2, and a diffusion coefficient $D_l \sim \mathcal{O}(10^{-10})$ m^2/s (Nanne *et al.*, 2010) yields a resulting Peclet number that satisfies $\mathrm{Pe}_l \sim \mathcal{O}(10^8) \gg 1$, indicating that convective transport dominates and diffusion is negligible, at least outside of any possible boundary layers.

The bulk solute transport equations (5.80a) and (5.80b) are second-order partial differential equations in the spatial coordinate x, which typically require two boundary conditions in x for well-posedness. One boundary condition is provided at the inlet, given by (5.81b), but specifying a physically meaningful second condition is nontrivial.

Given that $\mathrm{Pe}_l \gg 1$, the second boundary condition may lead to a boundary layer near the inlet or outlet. However, such a boundary layer does affect the dynamic of solute transport within the bulk, so we neglect it.

Neglecting the diffusion terms reduces the governing equations to first-order in x, requiring only one boundary condition at the inlet to ensure well-posedness.

5.6.3 Total effective membrane hydraulic conductivity $\mathcal{K}$

A dimensional analysis of fluid flow equations (5.79a) and (5.79b) suggests that if

$$\mathcal{K}[\mathcal{R}][x]^2 \ll 1, \tag{5.84}$$

then the total effective membrane hydraulic conductivity $\mathcal{K}$ is relatively small and can be neglected. This allows the application of asymptotic techniques to arrive at explicit estimates of

dialysis effectiveness.

Substituting the typical values from Table 5.1, $[x] = 0.26$ m, $\mathcal{K} = 5.3 \times 10^{-14}$ m^3 s kg^{-1}, and choosing $[\mathcal{R}] = |\mathcal{R}_b| \approx 1 \times 10^{14}$ m^{-4} Pa s (using $\mu = \mu_b$), we obtain:

$$\mathcal{K}[\mathcal{R}][x]^2 = \mathcal{K}|\mathcal{R}_b|L^2 \approx 0.36. \tag{5.85}$$

As this value is reasonably small, we assume that the total effective membrane hydraulic conductivity $\mathcal{K}$ is relatively small in our model and employ asymptotic methods based on this assumption to analyse and solve the governing equations. Henceforth, we use the shorthand notation $O(\mathcal{K})$ to mean $O(\mathcal{K}[\mathcal{R}][x]^2)$ in the context of the full nondimensionalization, and $\mathcal{K} \ll 1$ to mean (5.84).

5.7 Steady-state clearance

The efficiency of a HD treatment protocol is measured in terms of the clearance, which is defined as volume of plasma completely cleared of the solute per unit time,

$$\mathscr{K} = q_{b0}(C_{b0} - C_{bL})/C_{b0} \tag{5.86}$$

where $C_{bL} = C_b\big|_{x=L}$. For convenience, we also define the relative clearance

$$\mathscr{K}_r = \mathscr{K}/\mathscr{K}_{\max} = (C_{b0} - C_{bL})/(C_{b0} - C_{d0}), \tag{5.87}$$

where $\mathscr{K}_{\max} = q_{b0}(C_{b0} - C_{d0})/C_{b0}$ is the theoretical maximum clearance a dialyser can achieve by diffusion. The relative clearance $\mathscr{K}_r$ describes the proportion of toxins cleared during treatment relative to the maximum clearance. The limiting case in which the relative clearance $\mathscr{K}_r = 1$ (or 0) is one in which the treatment is fully efficient (inefficient).

Likewise, the clearance of HDF is

$$\mathscr{K} = q_{b0}\left[C_{b0} - C_{bL}(1-\beta)\right]/C_{b0}, \tag{5.88}$$

and the relative clearance is

$$\mathscr{K}_r = \left[C_{b0} - C_{bL}(1-\beta)\right]/(C_{b0} - C_{d0})\,. \tag{5.89}$$

We calculate the clearance under the assumption that the flow is in steady state and that diffusion along the fibre is negligible in comparison to diffusion across the fibre, so that the bulk solute transport equations (5.80a) and (5.80b) reduce to

$$\frac{\partial(C_b q_b)}{\partial x} = -J_m, \tag{5.90}$$

$$\frac{\partial(C_d q_d)}{\partial x} = J_m, \tag{5.91}$$

where

$$J_m = D(C_b - C_d) + (1-\sigma)V_m\left[(1-F)C_b + FC_d\right]. \tag{5.92}$$

5.7.1 Small-$\mathcal{K}$ asymptotics of HD

In this section, we aim to determine the relative clearance of HD as an expansion,

$$\mathcal{K}_r = \mathcal{K}_{r,0} + \mathcal{K}\mathcal{K}_{r,1} + O(\mathcal{K}^2), \tag{5.93}$$

in $\mathcal{K}$. To do so, we expand the fluid flux

$$q_l = q_{l,0} + \mathcal{K}q_{l,1} + O(\mathcal{K}^2) \tag{5.94}$$

and concentration

$$C_l = C_{l,0} + \mathcal{K}C_{l,1} + O(\mathcal{K}^2), \tag{5.95}$$

where $l = b, d$ and solve the resulting governing equations order by order.

Expanding the solution (5.20) with $\alpha = \beta = 0$ for the fluid flux in $\mathcal{K}$ yields the coefficients

$$q_{b,0} = q_{b0}, \quad q_{d,0} = q_{d0}, \quad q_{b,1} = \frac{1}{2}x(L-x)\left[a\mathcal{R}_d - q_{b0}(\mathcal{R}_b + \mathcal{R}_d)\right] \quad \text{and} \quad q_{d,1} = -q_{b,1}. \tag{5.96}$$

Expanding the transmembrane velocity,

$$V_m = -\mathcal{K}q'_{b,1} + O(\mathcal{K}^2), \tag{5.97}$$

where the prime represent derivative with respect to x. We find that V_m is zero at leading order, reflecting that there is no flow advecting the solute across the membrane in the regime in which the membrane permeability is zero ($\mathcal{K} = 0$). In this regime, the only transport mechanism is diffusion of solute across the membrane. The next-order term, proportional to $\mathcal{K}$, reflects flow through the membrane, and hence advective solute transport across the membrane. The proportion function,

$$F = \frac{1}{2} + \mathcal{K}\frac{1-\sigma}{12D}q'_{b,1} + O(\mathcal{K}^2), \tag{5.98}$$

is equal to a half at leading order, corresponding to a the regime in which the effective membrane concentration is the average of the blood and dialysate concentrations as in (5.60). In this regime, we have $Pe \ll 1$ and advective transport is negligible in comparison to diffusive transport across the membrane. The next-order correction term, proportional to $\mathcal{K}$, reflects the effects of advection across the membrane.

Combining the above expansions gives the following expansion for the total membrane so-

lute flux,

$$J_m = J_{m,0} + \mathcal{K} J_{m,1} + O(\mathcal{K}^2), \tag{5.99}$$

where

$$J_{m,0} = D\left(C_{b,0} - C_{d,0}\right) \quad \text{and} \quad J_{m,1} = D\left(C_{b,1} - C_{d,1}\right) - \frac{1}{2}(1-\sigma)\left(C_{b,0} + C_{d,0}\right) q'_{b,1}. \tag{5.100}$$

The leading-order total membrane solute flux reflects solute transport through diffusion alone, with a contribution from convective transport appearing at $O(\mathcal{K})$.

Diffusive solute transport and the Michaels equation

At leading order in $\mathcal{K}$, the governing solute transport equations (5.90)–(5.92) reduce to

$$q_{b0} C'_{b,0} = -D\left(C_{b,0} - C_{d,0}\right) \quad \text{and} \quad q_{d0} C'_{d,0} = D\left(C_{b,0} - C_{d,0}\right). \tag{5.101}$$

These leading-order governing equations reflect the steady-state transport of solute through diffusion across the membrane alone Michaels (1966). The solution can be found explicitly,

$$C_{b,0} = C_{d0} + (C_{b0} - C_{d0}) \frac{q_{b0} + q_{d0}\mathcal{E}^{(L-x)/L}}{q_{b0} + q_{d0}\mathcal{E}} \quad \text{and} \quad C_{d,0} = C_{d0} + (C_{b0} - C_{d0}) \frac{q_{b0} - q_{b0}\mathcal{E}^{(L-x)/L}}{q_{b0} + q_{d0}\mathcal{E}}, \tag{5.102}$$

for counter-current flows and

$$C_{b,0} = C_{d0} + (C_{b0} - C_{d0}) \frac{q_{b0} + q_{d0}\mathcal{E}^{-x/L}}{q_{b0} + q_{d0}} \quad \text{and} \quad C_{d,0} = C_{d0} + (C_{b0} - C_{b0}) \frac{q_{b0} - q_{b0}\mathcal{E}^{-x/L}}{q_{b0} + q_{d0}}, \tag{5.103}$$

for co-current flows. from which we find the leading-order relative clearance

$$\mathcal{K}_{r,0} = \begin{cases} \dfrac{q_{d0}\mathcal{E} - q_{d0}}{q_{d0}\mathcal{E} + q_{b0}} = 1 - \dfrac{q_{d0} + q_{b0}}{q_{d0}\mathcal{E} + q_{b0}} & \text{(counter-current)}, \\ \dfrac{q_{d0} - q_{d0}\mathcal{E}^{-1}}{q_{b0} + q_{d0}} = 1 - \dfrac{q_{b0} + q_{d0}\mathcal{E}^{-1}}{q_{b0} + q_{d0}} & \text{(co-current)}, \end{cases} \tag{5.104a}$$

where

$$\mathcal{E} = \exp\left(DL\left(q_{b0}^{-1} + q_{d0}^{-1}\right)\right) = \exp\left(K_{oA}\left(\hat{q}_{b0}^{-1} + \hat{q}_{d0}^{-1}\right)\right), \tag{5.104b}$$

K_{oA} is defined in §5.7.1, and $\hat{q}_{b0} = N q_{b0}$ and $\hat{q}_{d0} = N q_{d0}$ is the total flux of blood and dialysate, respectively, across the whole dialyser. Equation (5.104) is known as the Michaels equation for clearance, derived under the assumption that solute is transported across the membrane through diffusion alone Michaels (1966). The Michaels equation provides excellent agreement with experimental results for small molecules such as urea and sodium chloride in steady flow.

The mass transfer-area coefficient

The dialyser industry and dialysis literature use the mass transfer-area coefficient, K_{oA}, to characterise clearance. The mass transfer-area coefficient K_{oA} is a measure of how efficiently a solute of low molecular weight, such as urea, passes through a dialyser membrane via diffusion. The higher the value of K_{oA}, the more efficient the dialyser is at clearing the solute. The mass transfer-area coefficient K_{oA} is defined through the relationship

$$NL\langle J_{m,0}\rangle = K_{oA}\langle C_{b,0} - C_{d,0}\rangle, \tag{5.105}$$

between the leading-order total solute flux $NL\langle J_{m,0}\rangle$ through the membrane across the whole dialyser to the average difference in solute concentration either side of the membrane in the regime in which solute is transported across the membrane by diffusion only. Here, $\langle\cdot\rangle = L^{-1}\int_0^L \cdot\,\mathrm{d}x$ denotes the average along the length of the dialyser. Using the expression (5.100) for the leading-order membrane solute flux $J_{m,0}$ in the definition (5.105) of the mass transfer-area coefficient K_{oA} and rearranging gives

$$K_{oA} = NLD. \tag{5.106}$$

Weak convective solute transport

At next order, the governing solute transport equations (5.90)–(5.92) become

$$q_{b0}C'_{b,1} + (q_{b,1}C_{b,0})' = -D(C_{b,1} - C_{d,1}) + \frac{1}{2}(1-\sigma)\left(C_{b,0} + C_{d,0}\right)q'_{b,1}, \tag{5.107}$$

$$q_{d0}C'_{d,1} + (q_{d,1}C_{d,0})' = D(C_{b,1} - C_{d,1}) - \frac{1}{2}(1-\sigma)\left(C_{b,0} + C_{d,0}\right)q'_{b,1}, \tag{5.108}$$

from which the $O(\mathcal{K})$ contribution to the relative clearance can be found analytically as

$$\mathscr{K}_{r,1} = \begin{cases} L^2\left(q_{b0}+q_{d0}\right)\left(q_{b0}\mathcal{R}_b - q_{d0}\mathcal{R}_d\right)\dfrac{1}{\left(q_{b0}+\mathcal{E}q_{d0}\right)^2}\left(\dfrac{q_{d0}/q_{b0}-1}{12}\mathcal{E}\log\mathcal{E} + \sigma C\right) \\ L^2\left(q_{b0}\mathcal{R}_b - q_{d0}\mathcal{R}_d\right)\dfrac{1}{\mathcal{E}\left(q_{b0}+q_{d0}\right)}\left(\dfrac{q_{d0}/q_{b0}-1}{12}\log\mathcal{E} + \sigma C\right) \end{cases} \tag{5.109}$$

for counter- and co-current flows respectively, where

$$C = \begin{cases} \dfrac{\left(C_{b0} + \mathcal{E}C_{d0}q_{d0}/q_{b0}\right)\left(2 - 2\mathcal{E} + \log\mathcal{E} + \mathcal{E}\log\mathcal{E}\right)}{2(C_{b0}-C_{d0})\log^2\mathcal{E}} & \text{(counter-current)}, \\ \dfrac{\left(C_{b0} + C_{d0}q_{d0}/q_{b0}\right)\left(2 - 2\mathcal{E} + \log\mathcal{E} + \mathcal{E}\log\mathcal{E}\right)}{2(C_{b0}-C_{d0})\log^2\mathcal{E}} & \text{(co-current)}, \end{cases} \tag{5.110}$$

These formulae generalise and are consistent with previous results, in particular, the notion that clearance is linear in the ultrafiltration coefficient (Green *et al.*, 1976; Waniewski, 2006;

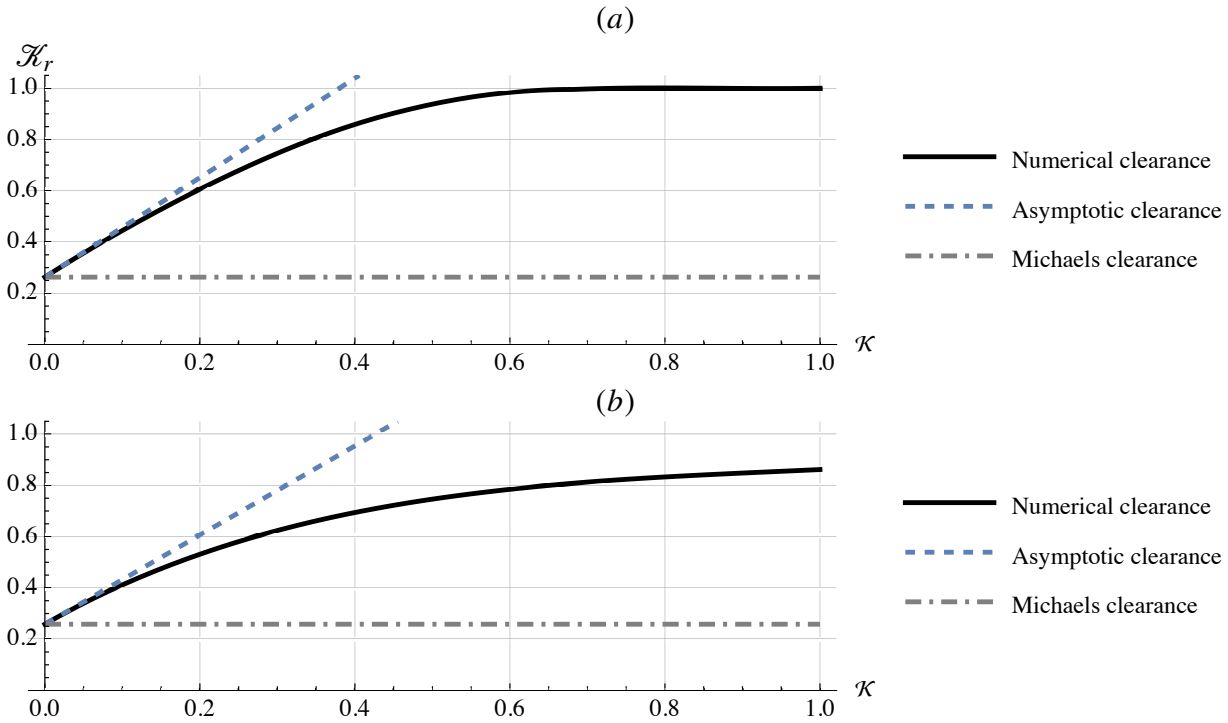

Figure 5.4: A comparison of numerical (solid), asymptotic (dashed, using (5.93),(5.104) and (5.109)) and Michaels (dash-dotted, using (5.104)) results for the relative clearance for (a) counter-current and (b) co-current flows. Parameter values used (without units): $\mu = 1$, $\sigma = 0.9$, $D = 1$, $r_b = 0.4$, $r_d = 1$, $q_{b0} = 3$, $|q_{d0}| = 5$, $L = 1$, $C_{b0} = 1$, $C_{d0} = 0$, and $\alpha = \beta = 0$.

Waniewski *et al.*, 1991).

The asymptotic solution (5.93) for the relative clearance up to $O(\mathcal{K})$, using (5.104) and (5.109), is compared against the Michaels clearance (5.104), up to $O(\mathcal{K}^0)$ and full numerical results for the relative clearance in Figure 5.4. The agreement between asymptotic and full numerical results highlights the linear nature of the clearance for small values of $\mathcal{K}$, for which the asymptotic approximations are valid. The Michaels clearance (5.104), though accurate for $\mathcal{K} = 0$ corresponding to solutes of small molecular weight, fails to reflect this linear change.

5.7.2 Small-$\mathcal{K}$ asymptotics for HDF

In the case of HDF, the transmembrane velocity $V_m \sim O(1)$, in contrast to $V_m \sim O(\mathcal{K})$ for conventional HD. This difference arises because an order-one fluid flux is advected from blood to dialysate, as dictated by the boundary conditions (5.19). Applying the same expansions (5.93)–(5.95), we find that at leading order in $\mathcal{K}$, the governing fluid flow equations (5.79a)–(5.79b) simplify to

$$q''_{b,0} = 0, \quad \text{and} \quad q''_{d,0} = 0, \tag{5.111}$$

and the solution can be found explicitly as

$$q_{b,0} = -\frac{(\alpha+\beta)q_{b0}}{L}x + (1+\alpha)q_{b0}, \quad \text{and} \quad q_{d,0} = \begin{cases} \dfrac{(\alpha+\beta)q_{b0}}{L}x + q_{d0} - (1+\alpha)q_{b0} \\ \dfrac{(\alpha+\beta)q_{b0}}{L}x + q_{d0} \end{cases} \tag{5.112}$$

for counter- and co-current flows, respectively. The transmembrane velocity, also known as the ultrafiltration flux, can be found as

$$V_{m,0} = -q'_{b,0} = q'_{d,0} = \frac{(\alpha+\beta)q_{b0}}{L}. \tag{5.113}$$

The governing solute transport equations (5.90)–(5.92) reduce to

$$q_{b0}C'_{b,0} - V_{m,0}C_{b,0} = -(1-\sigma)V_{m,0}\left[(1-\mathcal{F})C_{b,0} + \mathcal{F}C_{d,0}\right], \tag{5.114}$$

$$q_{d0}C'_{d,0} + V_{m,0}C_{d,0} = (1-\sigma)V_{m,0}\left[(1-\mathcal{F})C_{b,0} + \mathcal{F}C_{d,0}\right], \tag{5.115}$$

where we define

$$\mathcal{F} = F - \frac{D}{(1-\sigma)V_{m,0}} = -\frac{1}{e^{Pe_0}-1} \quad \text{and} \quad Pe_0 = \frac{(1-\sigma)V_{m,0}}{D}. \tag{5.116}$$

The solution for the concentration can be obtained analytically when $\sigma = 0$ (small molecules)

$$C_{b,0} - C_{d,0} = G_1 q_{b,0}^{-\mathcal{F}} |q_{d,0}|^{\mathcal{F}-1}, \tag{5.117}$$

$$q_{b,0}C_{b,0} + q_{d,0}C_{d,0} = G_2, \tag{5.118}$$

where G_1, G_2 are two constants and their values can be calculated by applying the boundary conditions, in agreement with the results of (Akcahuseyin *et al.*, 1990) for pre-dilution HDF, although an explicit formula for clearance has not been provided there.

We find the leading-order clearance to be

$$\mathscr{K}_{r,0} = \begin{cases} \dfrac{C_{b0} - C_{d0}(1-\beta)}{C_{b0} - C_{d0}} - \dfrac{[C_{b0} - C_{d0}(1+\alpha)]\,(Q+\beta-1)}{(C_{b0}-C_{d0})\left[Q^{1-\mathcal{F}}(1+\alpha)^{1-\mathcal{F}}(1-\beta)^{\mathcal{F}-1}(Q+\alpha+\beta)^{\mathcal{F}} - 1 - \alpha\right]}, \\ \dfrac{C_{b0}}{C_{b0}-C_{d0}} - \dfrac{1}{(C_{b0}-C_{d0})(1+Q+\alpha)}\Big\{(C_{b0}+C_{d0}Q)\,(1-\beta) \\ \qquad\qquad + [C_{b0} - C_{d0}(1+\alpha)]\,Q^{1-\mathcal{F}}(1+\alpha)^{\mathcal{F}-1}(1-\beta)^{1-\mathcal{F}}(Q+\alpha+\beta)^{\mathcal{F}}\Big\}, \end{cases} \tag{5.119}$$

for counter-current and co-current cases, respectively, where $Q = |q_{d0}/q_{b0}|$. The advantages of the asymptotic result (5.119) for the clearance are two-fold. First, it is an explicit formula, avoiding the need to compute solutions to differential equations to obtain the clearance in real-

life experiments. Second, it generalises prior results in that it accounts for both pre- and post-dilution HDF as well as a non-zero inlet dialysate concentration C_{d0}. The latter is useful for real-life applications in which dialysate is reused. The framework developed here also explains the assumptions used in prior work, such as (Akcahuseyin *et al.*, 1990), through rigorous asymptotic arguments. For example, we explain the uniformity of the ultrafiltration flux (5.113) using a reduction of systems of equations by means of asymptotic arguments.

Remarks

Assuming no toxins in the dialysate at inlet, ($C_{d0} = 0$), the clearance reduces to

$$\mathscr{K}_{r,0} = \begin{cases} 1 - \dfrac{Q+\beta-1}{Q^{1-\mathcal{F}}(1+\alpha)^{1-\mathcal{F}}(1-\beta)^{\mathcal{F}-1}(Q+\alpha+\beta)^{\mathcal{F}}-1-\alpha} & \text{(counter-current)}, \\ 1 - \dfrac{1-\beta+Q^{1-\mathcal{F}}(1+\alpha)^{\mathcal{F}-1}(1-\beta)^{1-\mathcal{F}}(Q+\alpha+\beta)^{\mathcal{F}}}{1+Q+\alpha} & \text{(co-current)}. \end{cases} \tag{5.120}$$

The expression can be further reduce to

$$\mathscr{K}_{r,0} = \begin{cases} 1 - \dfrac{(1-Q)Q^{\mathcal{F}}(1+\alpha)^{\mathcal{F}-1}}{Q^{\mathcal{F}}(1+\alpha)^{\mathcal{F}}-Q(Q+\alpha)^{\mathcal{F}}} & \text{(counter-current)}, \\ \dfrac{Q+\alpha-Q^{1-\mathcal{F}}(1+\alpha)^{\mathcal{F}-1}(Q+\alpha)^{\mathcal{F}}}{1+Q+\alpha} & \text{(co-current)}, \end{cases} \tag{5.121}$$

for pre-dilution only ($\beta = 0$), in agreement with (Akcahuseyin *et al.*, 1990), and

$$\mathscr{K}_{r,0} = \begin{cases} 1 - \dfrac{Q^{\mathcal{F}}(Q+\beta-1)}{Q(1-\beta)^{\mathcal{F}-1}(Q+\beta)^{\mathcal{F}}-Q^{\mathcal{F}}} & \text{(counter-current)}, \\ \dfrac{Q+\beta-Q^{1-\mathcal{F}}(1-\beta)^{1-\mathcal{F}}(Q+\beta)^{\mathcal{F}}}{1+Q} & \text{(co-current)}, \end{cases} \tag{5.122}$$

for post-dilution only ($\alpha = 0$).

It can be shown that the clearance (5.119) for HDF reduces to the Michaels equation (5.104) as both $\alpha \to 0$ and $\beta \to 0$.

In the limit as $Q \to 0$, the clearance (5.119) simplifies to

$$\mathscr{K}_{r,0} = \frac{C_{b0}(\alpha+\beta)}{(C_{b0}-C_{d0})(1+\alpha)}, \tag{5.123}$$

which corresponds to *pure haemofiltration*, where solute removal is achieved solely by convection.

In contrast, as $Q \to \infty$, the clearance (5.119) approaches

$$\mathscr{K}_{r,0} = \frac{C_{b0}-C_{d0}(1-\beta)}{C_{b0}-C_{d0}} - \frac{C_{b0}-C_{d0}(1+\alpha)}{C_{b0}-C_{d0}}(1+\alpha)^{\mathcal{F}-1}(1-\beta)^{1-\mathcal{F}}, \tag{5.124}$$

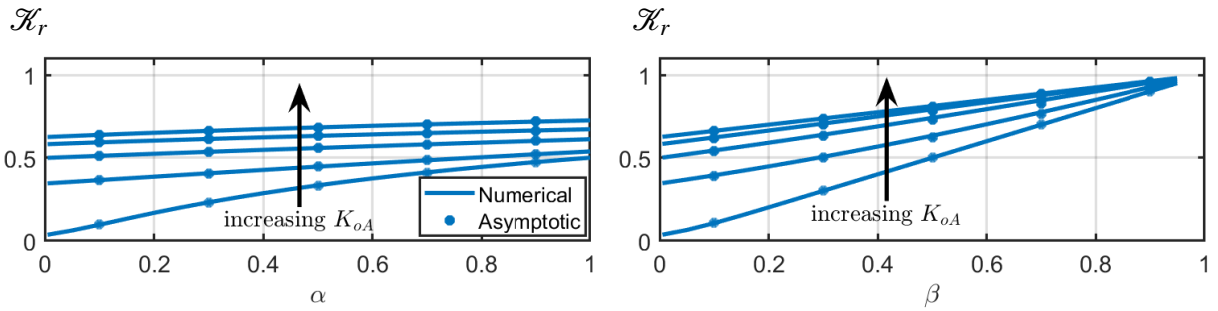

(a) Co-current, pre-dilution.

(b) Co-current, post-dilution.

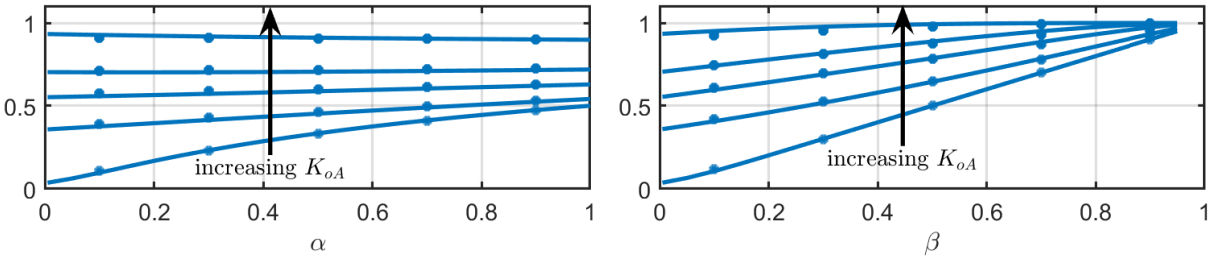

(c) Counter-current, pre-dilution.

(d) Counter-current, post-dilution.

Figure 5.5: Relative clearance in various forms of HDF for varying values of K_{oA}, comparing numerical results (solid curves) with asymptotic predictions (dots). Parameter values are given in Table 5.1, with $C_{d0} = 0$, $q_{b0} = 300\,\text{ml/min}$, $|q_{d0}| = 500\,\text{ml/min}$, and $K_{oA} = 10, 150, 300, 500, 1415$ ml/min.

which represents the *idealized upper limit* of HDF, assuming an infinite flux of dialysate.

These asymptotic formulae provide a convenient means to classify dialyser performance in pre-and post-dilution HDF. In particular, they shed light on what proportion of fluid to add and subtract in pre- and post-dilution HDF in order to achieve a desired clearance. The asymptotic formulae are also much more versatile in usage for performing parameter sweeps, in comparison to full computational fluid dynamic simulations, common in the field. We discuss potential usage examples in the following section.

5.8 Results and discussion

Figure 5.5 shows the relative clearance as a function of either the pre-dilution filtration fraction, α, or the post-dilution filtration fraction, β, for various values of K_{oA} for HDF in the form of pre-dilution only and post-dilution only. Conventional HD corrosponds to $\alpha = 0$ in the case of pre-dilution only and $\beta = 0$ in the case of post-dilution only. In Figures 5.5(a) and 5.5(b), the dialysate flows in the same direction as the blood ($q_{d0}/q_{b0} > 0$), whereas Figure 5.5(c) and Figure 5.5(d) shows the counter-current case, where dialysate and blood flow in opposite directions ($q_{d0}/q_{b0} < 0$). We find that the low-permeability asymptotic result agrees well with the corresponding numerical simulations.

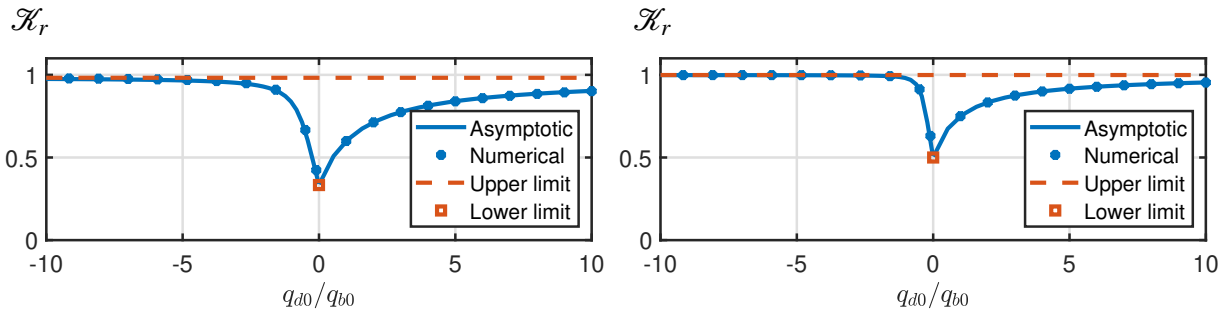

(a) Pre-dilution HDF.

(b) Post-dilution HDF.

Figure 5.6: Relative clearance for pre- and post-dilution HDF for low–molecular-weight molecules (K_{oA} = 1415 ml/min) as a function of the flux ratio q_{d0}/q_{b0}, comparing numerical results (dots) with asymptotic predictions (solid curves), and the idealized upper limit (dashed-dotted curves). Parameter values are given in Table 5.1, with $C_{d0} = 0$, $\alpha = 0.5$, $\beta = 0$ for pre-dilution and $\alpha = 0$, $\beta = 0.5$ for post-dilution.

The parameter K_{oA} is determined by the molecular weight (or size) of the toxin. For the dialyser used in our model (Braun Diacap® Pro 19H), the smallest toxin considered is urea, represented by the value K_{oA} = 1415 ml/min, corresponding to the uppermost curve in each plot in Figure 5.5. The lowest curves correspond to K_{oA} = 10 ml/min, representing large-molecular-weight toxins that are poorly removed by HD due to their very low diffusion coefficients, hence the low clearance reported in Figure 5.5 for this value of K_{oA}.

Overall, the relative clearance generally increases with increasing α or β for all values of K_{oA}. An exception occurs in the counter-current pre-dilution only case in Figure 5.5(c); as K_{oA} increases, the relative clearance changes from increasing with α to decreasing with α. This highlights that pre-dilution HDF works less well for clearing low molecular weights (high K_{oA}). Additionally, we confirm empirical findings that HDF, whether pre- or post-dilution, is more effective for large, poorly diffusive toxins (low K_{oA}) than for small, highly diffusive toxins (high K_{oA}) (Canaud *et al.*, 2025).

Figure 5.6 shows the relative clearance as a function of the flux ratio q_{d0}/q_{b0} for both pre-dilution only and post-dilution only HDF. Co- and counter-current flows corrospond to the regions in which $q_{d0}/q_{b0} > 0$ and $q_{d0}/q_{b0} < 0$, respectively. The low-permeability asymptotic result matches the corresponding numerical simulations well. The special case $q_{d0}/q_{b0} = 0$ corresponds to haemofiltration, for which the relative clearance agrees with the asymptotic result (5.123) for pure haemofiltration. We observe that the relative clearance increases as $|q_{d0}/q_{b0}|$ increases away from zero. Furthermore, for both $q_{d0}/q_{b0} < 0$ and $q_{d0}/q_{b0} > 0$, the relative clearance approaches an upper limit as $|q_{d0}/q_{b0}| \gg 1$, which agrees well with the asymptotic result (5.124) for the idealized upper limit of HDF. It can be seen from Figure 5.5 and 5.6 that counter-current flows are more effective, leading to greater clearances, which has also been observed experimentally and used more widely in the dialysis technology industry Davenport *et al.* (2008); Kim *et al.* (2013); Baldwin *et al.* (2016).

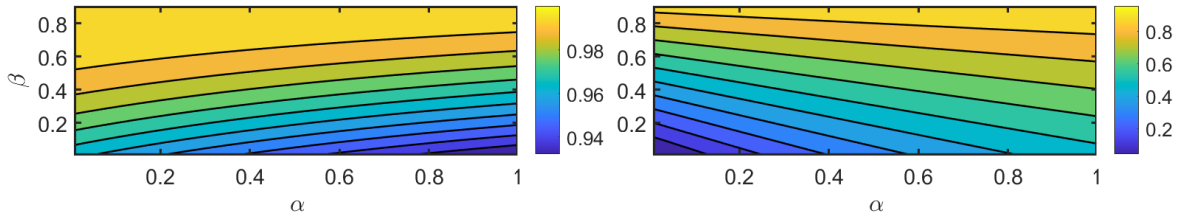

(a) Low-molecular-weight molecules.

(b) High-molecular-weight molecules.

Figure 5.7: Idealised upper limits of HDF clearance for low–molecular-weight molecules (K_{oA} = 1000 ml/min) and high–molecular-weight molecules (K_{oA} = 10 ml/min). Parameter values are listed in Table 5.1 and $C_{d0} = 0$.

As can be seen from the far-left and far-right-hand parts of both panels of Figure 5.6, much information can be extracted about the clearance in terms of the $|q_{d0}/q_{b0}| \gg 1$ limit alone. We use the asymptotic result (5.124) for the idealized upper limit for the clearance in the limit $|q_{d0}/q_{b0}| \gg 1$ for both counter- and co-current flows to explore the (α,β)-parameter space in figure 5.7 for various values of K_{oA}. In particular, we find that an increase in the post-dilution dialysate fraction β consistently enhances the limit for both low- and high–molecular-weight molecules. In contrast, an increase in the pre-dilution dialysate fraction α improves clearance for high–molecular-weight molecules but reduces clearance for low–molecular-weight molecules. The latter is consistent with the empirical observation that HDF is generally more effective for mid-to-high molecular weights only. We note that parameter sweeps of the like of Figure 5.7, of significantly lower computational cost than full CFD, have the potential to inform dialysis treatment design for better patient outcomes and more sustainable costs. An example could be the simple two-stage protocol in which the pre-dilution dialysate fraction α is altered from a relatively large value in the initial stage of a treatment, to clear molecules of high molecular weight first, followed by the second stage of treatment in which the pre-dilution dialysate fraction α is lowered, perhaps even to zero, to clear out toxins of low molecular weight, which are easiest to clear.

5.9 Conclusions

In this chapter, we have developed a mathematical framework to model the fundamental physical processes involved in HD and HDF. By considering both cylindrical and flat-layer geometries, and employing asymptotic simplifications, we derived tractable models that describe the essential aspects of fluid flow, solute transport, and membrane filtration. Notably, we have obtained analytical expressions for solute clearance with and without the effects of convection, which are central to evaluating dialysis performance.

Our framework recovers prior results obtained in the dialysis literature as special cases and

rigorously explains the ad-hoc assumptions made there. The framework presented here is intentionally modular and extendable. It provides a solid mathematical foundation upon which more complex and physiologically realistic features can be incorporated in future work. For example, potential extensions include:

1. **Higher-order corrections for the clearance.**
2. **Time-dependent flow rates:** The blood and dialysate fluxes need not be constant. Incorporating time-dependent flow allows for the modelling of modern dialysis machines that use dynamic pumping strategies.
3. **Membrane blocking effects:** Under steady flow conditions, particles may accumulate inside the membrane pores, which can hinder the transport of toxins.

Chapter 6

Conclusions

In this thesis, we have investigated a range of problems involving thin-film flows with deformable and porous interfaces, spanning both fundamental fluid-mechanical instabilities and applications in biomedical transport.

Chapters 2–4 examined the dynamics and stability of viscous gravity currents in systems where two immiscible fluids interact through deformable interfaces, with the upper layer in contact with the atmosphere. These configurations, though idealized, are representative of many natural and industrial processes and, perhaps unexpectedly, are prone to a novel viscous fingering instability.

In Chapter 2, we developed a theoretical framework for viscous gravity currents spreading over lubricated substrates. Using similarity solutions in both axisymmetric and planar geometries, we demonstrated how the viscosity ratio, density contrast, and source fluxes affect the evolution of the two layers, their thicknesses and velocity fields. An asymptotic analysis near the intrusion front characterises a stress singularity, arising from the use of lubrication theory.

Chapter 3 extended this framework by analysing the stability of these flows to non-axisymmetric disturbances, revealing that such flows are prone to a new class of viscous fingering instabilities. Such instabilities are perhaps most closely related to classical Saffman–Taylor instabilities, emerging solely from hydrodynamic interactions between two viscous fluids. We showed numerically that the instability requires a sufficiently large viscosity ratio (i.e., the intruding fluid needs to be of sufficiently low viscosity relative to the retreating fluid), is suppressed by density contrasts, and exhibits wavelength selection even without the effects of surface tension. The source fluxes were also found to play a central role in determining the onset of instability.

In Chapter 4, we explored the same system on an inclined substrate. Despite the added downslope gravitational forcing, the onset and mechanism of instability mirrored the horizontal case, confirming that the phenomenon is intrinsic to viscosity and density contrasts rather than geometric configuration.

Finally, in Chapter 5, we shifted focus to biomedical transport, exploring the thin-film flow of blood and dialysate within haemodialysers. Here, the two fluids are separated by a porous,

semipermeable membrane to aid in the removal of toxins from the blood. We built a unifying modelling framework faithful to the underlying fluid mechanics, which gives rise to existing classical results in various asymptotic limits. This work provides not only rigorous justification for earlier empirical assumptions but also a flexible mathematical foundation for future improvements in dialyser design and innovation in treatment modalities.

In summary, this thesis advances our understanding of thin-film flows across different contexts, from the fundamental fluid mechanics of flows susceptible to a previously unrecognised class of instabilities, to the fluid mechanics of dialysis. The former deepens our theoretical understanding of how interfacial flows become unstable and evolve, while the latter translates fluid-mechanical modelling into practical tools for assessing and improving dialysis treatment efficiency.

Appendix A

Asymptotic expansions near the intrusion front

We examine the behaviour of the flow near the intrusion front by deriving an asymptotic solution in the axisymmetric geometry and note that the derivation in the two-dimensional geometry is similar, leading to an identical solution. In particular, we expand the thicknesses of the two layers as

$$F \sim A_1\delta^{\frac{1}{2}} + A_2\delta + A_3\delta^{\frac{3}{2}} + \cdots, \tag{A.1}$$

$$f \sim a_0 + a_1\delta^{\frac{1}{2}} + a_2\delta + a_3\delta^{\frac{3}{2}} + \cdots, \tag{A.2}$$

in the coordinate $\delta = (1-\xi/\xi_N) \ll 1$. Although we aim to derive asymptotic solutions valid up to $O(\delta)$, we include the $O(\delta^{3/2})$ contributions as they feature in the derivations before ultimately dropping out in a final solvability condition.

At leading order, specifically $O\big(\delta^{-3/2}\big)$, the governing equation (2.34) for the lower layer yields the relationship

$$(\mathcal{D}+1)a_1 + A_1 = 0, \tag{A.3}$$

between the coefficients A_1 and a_1. Physically, this condition indicates that the lower-layer pressure gradient, $F' + (1+\mathcal{D})f'$, is non-singular at the nose.

The leading-order contribution to the governing equation (2.33) for the upper layer is of $O\big(\delta^{-1/2}\big)$ and gives rise to the relationship

$$(\mathcal{D}+1)a_2 + A_2 + \frac{A_1^2\mathcal{D}}{a_0(\mathcal{D}+1)} - \frac{\xi_N^2}{3a_0^2} = 0. \tag{A.4}$$

At next order, we notice that the governing equations for the two layers yield relationships that depend on a_3 and A_3 through the combination $(\mathcal{D}+1)a_3 + A_3$. Specifically, the $O\big(\delta^{-1/2}\big)$

contribution to (2.34) and the $O(1)$ contribution to (2.33) yield

$$(\mathcal{D}+1)a_3 + A_3 + \gamma_1 = 0, \tag{A.5}$$

$$(\mathcal{D}+1)a_3 + A_3 + \gamma_2 = 0, \tag{A.6}$$

respectively, where γ_1 and γ_2 are algebraic expressions in terms of a_0, a_2, A_1, A_2 and ξ_N. Explicitly,

$$\gamma_1 = -\frac{A_1^3\mathcal{D}}{a_0^2(\mathcal{D}+1)^2} - \frac{A_2A_1(2-3\mathcal{D})}{2a_0(\mathcal{D}+1)} + \frac{A_1\xi_N^2}{3a_0^3(\mathcal{D}+1)} - \frac{a_2A_1}{a_0}, \tag{A.7}$$

and

$$\gamma_2 = \frac{2A_1^3\mathcal{D}(\mathcal{D}\mathcal{M}+\mathcal{M}-3)}{9a_0^2(\mathcal{D}+1)^2} + \frac{8A_2A_1\mathcal{D}}{3a_0(\mathcal{D}+1)} + \frac{2a_2A_2(\mathcal{D}+1)}{3A_1} - \frac{2A_2\xi_N^2}{9a_0^2A_1} + \frac{2A_2^2}{3A_1}. \tag{A.8}$$

The combination $(\mathcal{D}+1)a_3 + A_3$ can be eliminated by subtracting (A.5) from (A.6), which gives

$$\gamma_1 = \gamma_2. \tag{A.9}$$

Solving (A.4) and (A.9) for a_2 and A_2 yields

$$a_2 = \frac{\xi_N^2}{3a_0^2(\mathcal{D}+1)} + \frac{A_1^2(4\mathcal{M}-9)}{9a_0(\mathcal{D}+1)} - \frac{A_1^2}{3a_0(\mathcal{D}+1)^2}, \tag{A.10}$$

$$A_2 = \frac{4A_1^2}{3a_0}\left(\frac{1}{\mathcal{D}+1} - \frac{\mathcal{M}}{3}\right). \tag{A.11}$$

This fully determines the asymptotic solution up to $O(\delta)$ in terms of a_0, A_1 and ξ_N. The values of these parameters are determined by matching to the outer solution and applying the two source flux boundary conditions and the far field condition.

We note that this calculation could also be performed in a more general travelling-wave framework, resulting in a similar asymptotic calculation.

Appendix B

Large $\mathcal{D}$ asymptotics

We examine the $\mathcal{D} \gg 1$ limit by expanding

$$F = F_0 + \mathcal{D}^{-1} F_1 + O\big(\mathcal{D}^{-2}\big), \quad f = f_0 + \mathcal{D}^{-1} f_1 + O\big(\mathcal{D}^{-2}\big), \tag{B.1}$$

$$\phi_u = \phi_{u0} + \mathcal{D}^{-1} \phi_{u1} + O\big(\mathcal{D}^{-2}\big), \quad \phi_l = \phi_{l0} + \mathcal{D}^{-1} \phi_{l1} + O\big(\mathcal{D}^{-2}\big). \tag{B.2}$$

At $O(\mathcal{D})$, the upper- and lower-layer fluxes vanish so that

$$0 = -\frac{3}{2} f_0^2 F_0 f_0' \quad \text{and} \quad 0 = -f_0^3 f_0', \tag{B.3a,b}$$

from which we deduce that f_0' vanishes. Matching to the single-layer region ahead of the intrusion front and applying the far-field boundary condition determines the constant of integration, which gives $f_0 = 1$.

At $O(\mathcal{D}^0)$, we find that the leading-order fluxes reduce to

$$\phi_{u0} = -\frac{3}{2} F_0 f_1' - \frac{1}{2}\left(2F_0^2 \mathcal{M} + 6F_0 + 3\right) F_0 F_0', \quad \phi_{l0} = -f_1' - \frac{3}{2} F_0 F_0' - F_0', \tag{B.4a,b}$$

and the mass conservation equations reduce to

$$\frac{1}{2}\xi F_0' = \frac{1}{\xi^n}\left(\xi^n \phi_{u0}\right)', \quad 0 = \frac{1}{\xi^n}\left(\xi^n \phi_{l0}\right)', \tag{B.5a,b}$$

where $n = 0$ in the two-dimensional geometry and $n = 1$ in the axisymmetric geometry. Integrating the second of these directly and applying the source flux boundary condition, we obtain the lower-layer flux explicitly as $\phi_{l0} = Q_l/\xi^n$. Eliminating f_1', we find that the upper-layer flux can be written in terms of F_0 and its derivative alone. Explicitly,

$$\phi_{u0} = -\frac{1}{4}\left(\left(4\mathcal{M} F_0 + 3\right) F_0 F_0' - 6 Q_l \xi^{-n}\right) F_0 \tag{B.6}$$

While equations (B.5a) and (B.6) have no closed-form analytic solution, they form a complete

set of equations, which can be integrated numerically. These asymptotic solutions, valid for $\mathcal{D} \gg 1$, are shown in figure 2.6 in comparison to full numerical solutions for a range of values of $\mathcal{D}$.

Appendix C

Small Q_u asymptotics

We examine the $Q_u \ll 1$ limit by expanding

$$F = Q_u F_1 + O(Q_u^2), \quad f = f_0 + Q_u f_1 + O(Q_u^2), \tag{C.1}$$

$$\phi_u = Q_u \phi_{u1} + O(Q_u^2), \quad \phi_l = \phi_{l0} + Q_u \phi_{l1} + O(Q_u^2). \tag{C.2}$$

We find that the lower layer is independent of the flow of the upper layer at leading order. Specifically, at $O(Q_u^0)$, we find that the governing equations for the lower layer reduce to

$$\phi_{l0} = -(\mathcal{D}+1) f_0^3 f_0' \quad \text{and} \quad \frac{1}{2}\xi f_0' = \frac{1}{\xi^n}(\xi^n \phi_{l0})', \tag{C.3a,b}$$

where $n = 0$ in the two-dimensional geometry and $n = 1$ in the axisymmetric geometry. These form a complete set of equations, which are independent of the upper layer and are identical to the equations describing the flow ahead of the intrusion front. These are supplemented by the source flux boundary condition and the far-field boundary condition.

At $O(Q_u)$, we find that the governing equations for the upper layer reduce to

$$\phi_{u1} = -\frac{3}{2}(\mathcal{D}+1) f_0^2 F_1 f_0' \quad \text{and} \quad \frac{1}{2}\xi F_1' = \frac{1}{\xi^n}(\xi^n \phi_{u1})'. \tag{C.4a,b}$$

These simplify to a single equation

$$\frac{F_1'}{F_1} = -\frac{3(\mathcal{D}+1) f_0 \left(f_0 \left(\xi^n f_0' \right)' + 2\xi^n \left(f_0' \right)^2 \right)}{\xi^n \left(3(\mathcal{D}+1) f_0^2 f_0' + \xi \right)}, \tag{C.5}$$

which involves a singular point at the intrusion front. The position of the intrusion front can, therefore, be determined by finding the value of ξ for which the denominator vanishes. Specifically, $\xi = \xi_N$ is the solution to $3(\mathcal{D}+1) f_0^2 f_0' + \xi = 0$, or, equivalently, $\xi = 3\phi_{l0}/f_0$. The position of the intrusion front is shown to converge to this asymptotic limit as $Q_u \to 0$ in figure 2.11.

Appendix D

Asymptotic expansions near the intrusion front

Similar to the base flows of §2, we find that the thicknesses of the two layers can be expanded as

$$\begin{aligned} F(\xi,\vartheta,\tau) &\sim A_1(\vartheta,\tau)\delta^{\frac{1}{2}} + A_2(\vartheta,\tau)\delta + A_3(\vartheta,\tau)\delta^{\frac{3}{2}}..., \\ f(\xi,\vartheta,\tau) &\sim a_0(\vartheta,\tau) + a_1(\vartheta,\tau)\delta^{\frac{1}{2}} + a_2(\vartheta,\tau)\delta + a_3(\vartheta,\tau)\delta^{\frac{3}{2}}.... \end{aligned} \tag{D.1}$$

near the intrusion front where $\delta = (1-\xi/\xi_N) \ll 1$.

For the governing equation (3.19) describing the lower layer, the leading-order contribution is of $O(\delta^{-3/2})$ and yields the relationship

$$(\mathcal{D}+1)a_1 + A_1 = 0 \tag{D.2}$$

between A_1 and a_1. The leading-order contribution of the governing equation (3.18) for the upper layer is of $O(\delta^{-1/2})$ and gives rise to

$$(\mathcal{D}+1)a_2 + A_2 + \frac{A_1^2\mathcal{D}}{a_0(\mathcal{D}+1)} - \frac{\xi_N^2}{3a_0^2} - \frac{2\xi_N}{3a_0^2}\frac{\partial\xi_N}{\partial\tau} + O\left(\frac{\partial}{\partial\vartheta}\times\frac{\partial}{\partial\vartheta}\right) = 0, \tag{D.3}$$

where $O\left(\frac{\partial}{\partial\vartheta}\times\frac{\partial}{\partial\vartheta}\right)$ represent terms that contain products of two azimuthal derivatives, which are zero for the base solution and negligible for small-amplitude perturbations. This equation is identical to the equivalent equation for the base flow apart from the addition of the term containing a derivative with respect to τ and the (negligible) higher order terms.

Going to the next order, the $O\left(\delta^{-1/2}\right)$ contribution to (3.19) and the $O(1)$ contribution to

(3.18) yield

$$(\mathcal{D}+1)a_3 + A_3 + \gamma_1 + O\left(\frac{\partial}{\partial\vartheta}\times\frac{\partial}{\partial\vartheta}\right) = 0, \tag{D.4}$$

$$(\mathcal{D}+1)a_3 + A_3 + \gamma_2 + O\left(\frac{\partial}{\partial\vartheta}\times\frac{\partial}{\partial\vartheta}\right) = 0, \tag{D.5}$$

respectively, where

$$\gamma_1 = -\frac{A_1^3\mathcal{D}}{a_0^2(\mathcal{D}+1)^2} - \frac{A_2A_1(2-3\mathcal{D})}{2a_0(\mathcal{D}+1)} + \frac{A_1\xi_N^2}{3a_0^3(\mathcal{D}+1)} - \frac{a_2A_1}{a_0} + \frac{2A_1\xi_N}{3a_0^3(1+\mathcal{D})}\frac{\partial\xi_N}{\partial\tau}, \tag{D.6}$$

and

$$\gamma_2 = \frac{2A_1^3\mathcal{D}(\mathcal{D}\mathcal{M}+\mathcal{M}-3)}{9a_0^2(\mathcal{D}+1)^2} + \frac{8A_2A_1\mathcal{D}}{3a_0(\mathcal{D}+1)} + \frac{2a_2A_2(\mathcal{D}+1)}{3A_1} - \frac{2A_2\xi_N^2}{9a_0^2A_1} + \frac{2A_2^2}{3A_1} - \frac{4A_2\xi_N}{9a_0^2A_1}\frac{\partial\xi_N}{\partial\tau}. \tag{D.7}$$

Similarly to before, these coefficients generalise those describing the base flow through the addition of terms involving derivatives with respect to τ and the higher order terms. We note that (D.4) and (D.5) depend on A_3 and a_3 through the combination $(D+1)a_3 + A_3$, which can be eliminated by subtracting (D.4) from (D.5), which gives

$$\gamma_1 = \gamma_2. \tag{D.8}$$

Finally, solving (D.3) and (D.8) for A_2 and a_2 yields

$$A_2 = -\frac{4A_1^2}{9a_0}\left(\mathcal{M} - \frac{3}{\mathcal{D}+1}\right), \tag{D.9}$$

$$a_2 = \frac{1}{9(\mathcal{D}+1)a_0^2}\left[3\xi_N\left(\xi_N + 2\frac{\partial\xi_N}{\partial\tau}\right) + A_1^2a_0\left(4\mathcal{M} - 9 - \frac{3}{\mathcal{D}+1}\right)\right], \tag{D.10}$$

specifying a_2 and A_2 in terms of a_0, A_1, and ξ_N.

Appendix E

Perturbed fluxes

Explict expressions for perturbations to the fluxes are given by (3.39)–(3.42), where

$$\alpha_{u1} = -\frac{3}{\xi_{N0}} F_0 \left[f_0 \left((\mathcal{D}+1) f_0' + F_0' \right) + F_0 \left(f_0' + F_0' \right) \right], \tag{E.1}$$

$$\alpha_{u2} = -\frac{3}{2\xi_{N0}} \left[f_0^2 \left((\mathcal{D}+1) f_0' + F_0' \right) + 2\mathcal{M} F_0^2 \left(f_0' + F_0' \right) + 4 f_0 F_0 \left(f_0' + F_0' \right) \right], \tag{E.2}$$

$$\alpha_{u3} = -\frac{1}{2\xi_{N0}} F_0 \left[3(\mathcal{D}+1) f_0^2 + 6 f_0 F_0 + 2\mathcal{M} F_0^2 \right], \tag{E.3}$$

$$\alpha_{u4} = -\frac{1}{2\xi_{N0}} F_0 \left[6 f_0 F_0 + 3 f_0^2 + 2\mathcal{M} F_0^2 \right], \tag{E.4}$$

$$\alpha_{u5} = \frac{1}{2\xi_{N0}^2} F_0 \left[3 f_0^2 \left((\mathcal{D}+1) f_0' + F_0' \right) + 2\mathcal{M} F_0^2 \left(f_0' + F_0' \right) + 6 f_0 F_0 \left(f_0' + F_0' \right) \right], \tag{E.5}$$

$$\alpha_{l1} = -\frac{3}{\xi_{N0}} f_0 \left[\left((\mathcal{D}+1) f_0 + F_0 \right) f_0' + \left(f_0 + F_0 \right) F_0' \right], \tag{E.6}$$

$$\alpha_{l2} = -\frac{3}{2\xi_{N0}} f_0^2 \left(f_0' + F_0' \right), \tag{E.7}$$

$$\alpha_{l3} = -\frac{1}{2\xi_{N0}} f_0^2 \left(2(\mathcal{D}+1) f_0 + 3F_0 \right), \tag{E.8}$$

$$\alpha_{14} = -\frac{1}{2\xi_{N0}} f_0^2 \left(2 f_0 + 3F_0 \right), \tag{E.9}$$

$$\alpha_{l5} = \frac{1}{2\xi_{N0}^2} f_0^2 \left[2 f_0 \left((\mathcal{D}+1) f_0' + F_0' \right) + 3F_0 \left(f_0' + F_0' \right) \right]. \tag{E.10}$$

Bibliography

AKCAHUSEYIN, E., VINCENT, H.H., VAN ITTERSUM, F.J., VAN DUYL, W.A. & SCHALEKAMP, M.A.D.H. 1990 A mathematical model of continuous arterio-venous hemodiafiltration (CAVHD). *Computer Methods and Programs in Biomedicine* **31** (3), 215–224.

AL-HOUSSEINY, T. T., TSAI, P. A. & STONE, H. A. 2012 Control of interfacial instabilities using flow geometry. *Nat. Phys.* **8**, 747–750.

ALGWAUISH, GHANIM & NAIRE, SHAILESH 2023 The thermo-viscous fingering instability of a cooling spreading liquid dome. *Phys. Fluids* **35** (11), 112109.

ALLEY, R. B., BLANKENSHIP, D. D., BENTLEY, C. R. & ROONEY, S. T. 1987 Till beneath ice stream B. 3. Till deformation: evidence and implications. *J. Geophys. Res.* **92**, 8921–8929.

B. BRAUN n.d. Diacap® pro [product image]. Retrieved 27 August 2025 from B. Braun website: `https://catalogs.bbraun.com/en-01/p/PRID00009756/diacap-pro-dialyzer`.

BALDWIN, IAN, BALDWIN, MARIE, FEALY, NIGEL, NERI, MAURO, GARZOTTO, FRANCESCO, KIM, JEONG C., GIULIANI, ANNA, BASSO, FLAVIO, NALESSO, FEDERICO, BRENDOLAN, ALESSANDRA & RONCO, CLAUDIO 2016 Con-current versus counter-current dialysate flow during cvvhd. a comparative study for creatinine and urea removal. *Blood purification* **41** (1-3), 171–176.

BALL, T. V. & HUPPERT, H. E. 2019 Similarity solutions and viscous gravity current adjustment times. *J. Fluid Mech.* **874**, 285–298.

BALMFORTH, N. J. & CRASTER, R. V. 2000 Dynamics of cooling domes of viscoplastic fluid. *J. Fluid Mech.* **422**, 225–248.

BALMFORTH, N. J., CRASTER, R. V. & TONIOLO, C. 2003 Interfacial instability in non-Newtonian fluid layers. *Phys. Fluids.* **15** (11), 3370–3384.

BATCHELOR, C.L. & DOWDESWELL, J.A. 2015 Ice-sheet grounding-zone wedges (gzws) on high-latitude continental margins. *Mar. Ecol.* **363**, 65–92.

BELLO, A.K., OKPECHI, I.G., OSMAN, M.A. & ET AL. 2022 Epidemiology of haemodialysis outcomes. *Nat Rev Nephrol* **18**, 378–395.

BEN-JACOB, ESHEL 1997 From snowflake formation to growth of bacterial colonies ii: Cooperative formation of complex colonial patterns. *Contemporary Physics* **38** (3), 205–241.

BEN-JACOB, E., SCHMUELI, H., SHOCHET, O. & TENENBAUM, A. 1992 Adaptive self- organisation during growth of bacterial colonies. *Physica A* **187**, 378–424.

BISCHOFBERGER, IRMGARD, RAMACHANDRAN, RADHA & NAGEL, SIDNEY R. 2014 Fingering versus stability in the limit of zero interfacial tension. *Nature Communications* **5**, 5265.

CANAUD, B., STRIPPOLI, G. & DAVENPORT, A. 2025 High-volume hemodiafiltration versus high-flux hemodialysis: A narrative review for the clinician. *J Clin Med* **14** (8), 2614.

CANCILLA, N., GURRERI, L., MAROTTA, G., CIOFALO, M., CIPOLLINA, A., TAMBURINI, A. & MICALE, G. 2022 A porous media cfd model for the simulation of hemodialysis in hollow fiber membrane modules. *Journal of membrane science* **646**, 120219.

CHANG, YEN-LIN & LEE, CHAU-JEN 1988 Solute transport characteristics in hemodiafiltration. *Journal of Membrane Science* **39** (2), 99–111.

CHAUDHRY, DAOUD, CHAUDHRY, ABDULLAH, PERACHA, JAVERIA & SHARIF, ADNAN 2022 Survival for waitlisted kidney failure patients receiving transplantation versus remaining on waiting list: systematic review and meta-analysis. *BMJ* **376**, arXiv: https://www.bmj.com/content/376/bmj-2021-068769.full.pdf.

CHIRAKARNJANAKORN, S. & ET AL. 2017 Cardiovascular impact in patients undergoing maintenance hemodialysis: Clinical management considerations. *Int J Cardiol* **232**, 12–23.

CHRISTY, IAN & HINTON, EDWARD M. 2023 Two-layer gravity currents of generalized Newtonian fluids. *Proc. R. Soc. A* **479** (2279).

CINAR, Y., RIAZ, A. & TCHELEPI, H. A. 2009 Experimental study of CO2 injection into saline formations. *Soc. Petrol. Engrs J.* **14**, 589–594.

DAUCK, TIM-FREDERIK 2020 Viscous fingering instabilities and gravity currents. PhD thesis, University of Cambridge.

DAUCK, TIM-FREDERIK, BOX, FINN, GELL, LAURA, NEUFELD, JEROME A. & LISTER, JOHN R. 2019 Shock formation in two-layer equal-density viscous gravity currents. *J. Fluid Mech.* **863**, 730–756.

DAUGIRDAS, J.T., BLAKE, P.G. & ING, T.S. 2012 *Handbook of Dialysis*. *Lippincott Williams & Wilkins Handbook Series* 5th ed. Wolters Kluwer Health.

DAVENPORT, A., WILL, E.J. & DAVISON, A.M. 2008 Effect of the direction of dialysate flow on the efficiency of continuous arteriovenous haemodialysis. *Blood Purification* **8** (6), 329–336, arXiv: https://karger.com/bpu/article-pdf/8/6/329/2295449/000169987.pdf.

DIAS, E. O. & MIRANDA, J. A. 2010 Control of radial fingering patterns: a weakly nonlinear approach. *Phys. Rev. E* **81**, 016312.

DING, WEIPING, LI, WEILI, SUN, SIJIE, ZHOU, XIAOMING, HARDY, PETER A., AHMAD, SUHAIL & GAO, DAYONG 2015 Three-dimensional simulation of mass transfer in artificial kidneys. *Artificial organs* **39** (6), E79–E89.

DONATO, DANILO, DE FIERRO, ADRIANA BOSCHETTI, ZWEIGART, CARINA, KOLB, MICHAEL, ELOOT, SUNNY, STORR, MARKUS, KRAUSE, BERND, LEYPOLDT, KEN & SEGERS, PATRICK 2017 Optimization of dialyzer design to maximize solute removal with a two-dimensional transport model. *Journal of Membrane Science* **541**, 519–528.

DUNG, NH, KIEN, NT, HAI, NTT & ET AL. 2019 Measuring serum beta2-microglobulin to predict long-term mortality in hemodialysis patients using low-flux dialyzer reuse. *Ther Clin Risk Manag.* **15**, 839–846.

FAST, P., KONDIC, L., SHELLEY, M. J. & PALFFY-MUHORAY, P. 2001 Pattern formation in non-Newtonian Hele-Shaw flow. *Phys. Fluids* **13**, 1191–1212.

FINK, J.H. & GRIFFITHS, R.W. 1990 Radial spreading of viscous-gravity currents with solidifying crust. *J. Fluid Mech.* **221**, 485–509.

FINK, J.H. & GRIFFITHS, R.W. 1998 Morphology, eruption rates and rheology of lava domes: insights from laboratory models. *J. Geophys. Res.* **103**, 527–545.

FOREMAN, KYLE J. & ET AL. 2018 Forecasting life expectancy, years of life lost, and all-cause and cause-specific mortality for 250 causes of death: reference and alternative scenarios for 2016–40 for 195 countries and territories. *The Lancet* **392** (10159), 2052–2090.

FOWLER, A. C. & JOHNSON, C. 1995 Hydraulic run-away – a mechanism for thermally regulated surges of ice sheets. *J. Glaciol.* **41** (139), 554–561.

FRANCIS, A, HARHAY, MN, ONG, ACM & ET AL. 2024 Chronic kidney disease and the global public health agenda: an international consensus. *Nat Rev Nephrol* **20** (7), 473–485.

GREEN, D. M., ANTWILER, G. D., MONCRIEF, J. W., DECHERD, J. F. & POPOVICH, R. P. 1976 Measurement of the transmittance coefficient spectrum of cuprophan and rp69 membranes: applications to middle molecule removal via ultrafiltration. *Transactions of the American Society for Artificial Internal Organs* **22**, 627–636.

GRIFFITHS, R. W. 2000 The dynamics of lava flows. *Annual Review of Fluid Mechanics* **32** (1), 477–518.

GRUNDY, R.E. & MCLAUGHLIN, R. 1982 Eigenvalues of the Barenblatt-Pattle similarity solution in nonlinear diffusion. *Proc. Roy. Soc. London Ser. A* **383**, 89–100.

GYLLENBERG, A. A. & SAYAG, R. 2022 Lubricated axisymmetric gravity currents of power-law fluids. *J. Fluid Mech.* **949**, A40.

HEWITT, DUNCAN R. & BALMFORTH, NEIL J. 2013 Thixotropic gravity currents. *J. Fluid Mech.* **727**, 56–82.

HEWITT, I. J. 2013 Seasonal changes in ice sheet motion due to melt water lubrication. *Earth Planet. Sci. Lett.* **371-372**, 16–25.

HIMMELFARB, JONATHAN, VANHOLDER, RAYMOND, MEHROTRA, RAJNISH & TONELLI, MARCELLO 2020 The current and future landscape of dialysis. *Nat. Rev. Nephrol.* **16** (10), 573–585.

HINDMARSH, R. C. A. 2004 Thermoviscous stability of ice-sheet flows. *J. Fluid Mech.* **502**, 17–40.

HINDMARSH, R. C. A. 2006 Stress gradient damping of thermoviscous ice flow instabilities. *J. Geophys. Res.* **111** (B12409).

HINDMARSH, R. C. A. 2009 Consistent generation of ice-streams via thermo-viscous instabilities modulated by membrane stresses. *Geophys. Res. Lett.* **36** (L06502).

HINTON, EDWARD M. 2022 Inferring rheology from free-surface observations. *J. Fluid Mech.* **937**, R4, arXiv: 2202.02893.

HINTON, EDWARD M. & HOGG, ANDREW J. 2022 Flow of a yield-stress fluid past a topographical feature. *J. Non-Newton. Fluid Mech.* **299**, 104696.

HOMSY, G. M. 1987 Viscous fingering in porous media. *Annu. Rev. Fluid Mech.* **19**, 271–311.

HOULT, D. P. 1972 Oil spreading on the sea. *Annu. Rev. Fluid Mech.* **4**, 341–368.

HULL, D. 1999 *Fractology*. Cambridge University Press.

HUPPERT, H. E. 1982*a* Flow and instability of a viscous current down a slope. *Nature* **300**, 427–429.

HUPPERT, H. E. 1982*b* The propagation of two-dimensional and axisymmetric viscous gravity currents over a rigid horizontal surface. *J. Fluid Mech.* **121**, 43–58.

HUPPERT, H. E. 2006 Gravity currents: a personal perspective. *J. Fluid Mech.* **554**, 299–322.

JAFFRIN, M, GUPTA, B & MALBRANCQ, J 1981 A one-dimensional model of simultaneous hemodialysis and ultrafiltration with highly permeable membranes. *Journal of biomechanical engineering* **103** (4), 261–266.

JAGER, KITTY J., KOVESDY, CSABA, LANGHAM, ROBYN, ROSENBERG, MARK, JHA, VIVEKANAND & ZOCCALI, CARMINE 2019 A single number for advocacy and communication—worldwide more than 850 million individuals have kidney diseases. *Kidney Int.* **96** (5), 1048–1050.

JUEL, A. 2012 Flattened fingers. *Nat. Phys.* **8**, 706–707.

KHAIRALLAH, S. A., ANDERSON, A. T., RUBENCHIK, A. & KING, W. E. 2016 Laser powder-bed fusion additive manufacturing: Physics of complex melt flow and formation mechanisms of pores, spatter, and denudation zones. *Acta Materialia.* **108**, 36–45.

KIM, JEONG CHUL, CRUZ, DINNA, GARZOTTO, FRANCESCO, KAUSHIK, MANISH, TEIXERIA, CATARINA, BALDWIN, MARIE, BALDWIN, IAN, NALESSO, FEDERICO, KIM, JI HYUN, KANG, EUNGTAEK, KIM, HEE CHAN & RONCO, CLAUDIO 2013 Effects of dialysate flow configurations in continuous renal replacement therapy on solute removal: Computational modeling. *Blood Purification* **35** (1-3), 106–111, arXiv: https://karger.com/bpu/article-pdf/35/1-3/106/2288707/000346093.pdf.

KONDIC, L., SHELLEY, M. J. & PALFFY-MUHORAY, P. 1998 Non-Newtonian Hele-Shaw flow and the Saffman-Taylor instability. *Phys. Rev. Lett.* **80**, 1433–1436.

KOVESDY, CSABA P. 2022 Epidemiology of chronic kidney disease: an update 2022. *Kidney Int. Suppl.* **12** (1), 7.

KOWAL, K.N. & WORSTER, M.G. 2020 The formation of grounding zone wedges: Theory and experiments. *J. Fluid Mech.* **898**, A12.

KOWAL, K. N. 2021 Viscous banding instabilities: non-porous viscous fingering. *J. Fluid Mech.* **926**, A4.

KOWAL, K. N., DAVIS, S. H. & VOORHEES, P. W. 2018 Thermocapillary instabilities in a horizontal liquid layer under partial basal slip. *J. Fluid Mech.* **855**, 839–859.

KOWAL, K. N. & WORSTER, M.G. 2019*a* Stability of lubricated viscous gravity currents. Part 1. Internal and frontal analyses and stabilisation by horizontal shear. *J. Fluid Mech.* **871**, 970–1006.

KOWAL, K. N. & WORSTER, M.G. 2019*b* Stability of lubricated viscous gravity currents. Part 2. Global analysis and stabilisation by buoyancy forces. *J. Fluid Mech.* **871**, 1007–1027.

KOWAL, K. N. & WORSTER, M. G. 2015 Lubricated viscous gravity currents. *J. Fluid Mech.* **766**, 626–655.

KOWAL, K. N. & WORSTER, S. S. PEGLER M. G. 2016 Dynamics of laterally confined marine ice sheets. *J. Fluid Mech.* **790**.

KUHLMANN, MARTIN K. 2023 12 - hemofiltration and hemodiafiltration. In *Handbook of Dialysis Therapy (Sixth Edition)*, Sixth edition edn. (ed. R. Nissenson Allen, N. Fine Richard, Mehrotra Rajnish & Zaritsky Joshua), pp. 135–140. New Delhi: Elsevier.

KUMAR, P., ZURI, S., KOGAN, D., GOTTLIEB, M. & SAYAG, R. 2021 Lubricated gravity currents of power-law fluids. *J. Fluid Mech.* **916**, A33.

KYRKE-SMITH, T. M., KATZ, R. F. & FOWLER, A. C. 2014 Subglacial hydrology and the formation of ice streams. *Proc. R. Soc. A.* **470**, 20130494.

LANG, THOMAS, ZAWADA, ADAM M., THEIS, LUKAS, BRAUN, JENNIFER, OTTILLINGER, BERTRAM, KOPPERSCHMIDT, PASCAL, GAGEL, ALFRED, KOTANKO, PETER, STAUSS-GRABO, MANUELA, KENNEDY, JAMES P. & CANAUD, BERNARD 2023 Hemodiafiltration: Technical and medical insights. *Bioengineering* **10** (2).

LEUNG, L. T. & KOWAL, K. N. 2022*a* Lubricated viscous gravity currents of power-law fluids. Part 1. Self-similar flow regimes. *J. Fluid Mech.* **940**, A26.

LEUNG, L. T. & KOWAL, K. N. 2022*b* Lubricated viscous gravity currents of power-law fluids. Part 2. Stability analysis. *J. Fluid Mech.* **940**, A27.

LI, S., LOWENGRUB, J. S., FONTANA, J. & PALFFY-MUHORAY, P. 2009 Control of viscous fingering patterns in a radial Hele-Shaw cell. *Phys. Rev. Lett.* **102**, 174501.

LISTER, J. R. & KERR, R. C. 1989 The propagation of two-dimensional and axisymmetric viscous gravity currents at a fluid interface. *J. Fluid Mech.* **203**, 215–249.

LIYANAGE, THAMINDA, NINOMIYA, TOSHIHARU, JHA, VIVEKANAND, NEAL, BRUCE, PATRICE, HALLE MARIE, OKPECHI, IKECHI, ZHAO, MING HUI, LV, JICHENG, GARG, AMIT X., KNIGHT, JOHN, RODGERS, ANTHONY, GALLAGHER, MARTIN, KOTWAL, SRADHA, CASS, ALAN & PERKOVIC, VLADO 2015 Worldwide access to treatment for end-stage kidney disease: a systematic review. *The Lancet* **385** (9981), 1975–1982.

LUO, RUI, CHEN, YUN & LEE, SUNGYON 2018 Particle-induced viscous fingering: Review and outlook. *Phys. Rev. Fluids* **3**, 110502.

MADHAVAN, MEERA, RITCHIE, ADAM J., ABOAGYE, JEREMY, JENKIN, DANIEL, PROVSTGAAD-MORYS, SAMUEL, TARBET, IONA, WOODS, DANIELLE, DAVIES, SOPHIE, BAKER, MEGAN, PLATT, ABIGAIL, FLAXMAN, AMY, SMITH, HOLLY, BELIJ-RAMMERSTORFER, SANDRA, WILKINS, DEIDRE, KELLY, ELIZABETH J., VILLAFANA, TONYA, GREEN, JUSTIN A., POULTON, IAN, LAMBE, TERESA, HILL, ADRIAN V.S., EWER, KATIE J. & DOUGLAS, ALEXANDER D. 2022 Tolerability and immunogenicity of an intranasally-administered adenovirus-vectored COVID-19 vaccine: An open-label partially-randomised ascending dose phase I trial. *eBioMedicine* **85**, 104298.

MASIUK, TINA, KADAKIA, PARUL & WANG, ZHENYU 2016 Development of a physiologically relevant dripping analytical method using simulated nasal mucus for nasal spray formulation analysis. *Journal of Pharmaceutical Analysis* **6** (5), 283–291.

MATAS, ARTHUR J., MONTGOMERY, ROBERT A. & SCHOLD, JESSE D. 2023 The organ shortage continues to be a crisis for patients with end-stage kidney disease. *JAMA Surgery* **158** (8), 787–788.

MATHUNJWA, J. S. & HOGG, A. J. 2006*a* Self-similar gravity currents in porous media: Linear stability of the Barenblatt-Pattle solution revisited. *Eur. J. Mech. B-Fluids* **25**, 360–378.

MATHUNJWA, J. S. & HOGG, A. J. 2006*b* Stability of gravity currents generated by finite-volume releases. *J. Fluid Mech.* **562**, 261–278.

MICHAELS, ALAN S. 1966 Operating parameters and performance criteria for hemodialyzers and other membrane-separation devices. *Transactions – American Society for Artificial Internal Organs* **12** (1), 387–392.

MORROW, L. C., MORONEY, T. J. & MCCUE, S. W. 2019 Numerical investigation of controlling interfacial instabilities in non-standard Hele-Shaw configurations. *J. Fluid Mech.* **877**, 1063–1097.

MUKHERJEE, T., ZUBACK, J. S., DE, A. & DEBROY, T. 2016 Printability of alloys for additive manufacturing. *Sci. Rep.* **6**, 19717.

MULLINS, W. W. & SEKERKA, R. F. 1964 Stability of a planar interface during solidification of a dilute binary alloy. *J. Appl. Phys.* **35** (2), 444–451.

NAGHAVI, MOHSEN & ET AL. 2017 Global, regional, and national age-sex specifc mortality for 264 causes of death, 1980-2016: A systematic analysis for the Global Burden of Disease Study 2016. *The Lancet* **390** (10100), 1151–1210.

NANNE, EDGAR E., AUCOIN, CHRISTIAN P. & LEONARD, EDWARD F. 2010 Shear rate and hematocrit effects on the apparent diffusivity of urea in suspensions of bovine erythrocytes. *ASAIO Journal* **56** (3), 151–156.

NASE, J., DERKS, D. & LINDNER, A. 2011 Dynamic evolution of fingering patterns in a lifted Hele-Shaw cell. *Phys. Fluids* **23**, 123101.

NATIONAL CENTER FOR BIOTECHNOLOGY INFORMATION (US) 2018 In brief: How does dialysis work? `https://www.ncbi.nlm.nih.gov/books/NBK492981/`, accessed 2025-08-31.

NAYLOR, KYLA L., KIM, S. JOSEPH, MCARTHUR, ERIC, GARG, AMIT X., MCCALLUM, MEGAN K. & KNOLL, GREGORY A. 2019 Mortality in incident maintenance dialysis patients versus incident solid organ cancer patients: A population-based cohort. *American Journal of Kidney Diseases* **73** (6), 765–776.

ORON, A., DAVIS, S. H. & BANKOFF, S. G. 1997 Long-scale evolution of thin liquid films. *Rev. Mod. Phys.* **69** (3), 931–980.

ORR, F. M. & TABER, J. J. 1984 Use of carbon dioxide in enhanced oil recovery. *Science* **224**, 563–569.

ORR, TIM R., ZOELLER, MICHAEL H., LLEWELLIN, EDWARD W. & PATRICK, MATTHEW R. 2023 Eruption of stagnant lava from an inactive perched lava lake. *Journal of Volcanology and Geothermal Research* **442**, 107912.

OSUGA, TOSHIAKI, OBATA, TAKAYUKI, IKEHIRA, HIROO, TANADA, SHUJI, SASAKI, YASUHITO & NAITO, HIDEMUNE 1998 Dialysate pressure isobars in a hollow-fiber dialyzer determined from magnetic resonance imaging and numerical simulation of dialysate flow. *Artificial Organs* **22** (10), 907–909.

PATRICK, M. R. & ORR, T. R. 2012 Rootless shield and perched lava pond collapses at kīlauea volcano, hawai'i. *Bulletin of Volcanology* **74** (1), 67–78.

PAYNE, A. J. & DONGELMANS, P. 1997 Self-organization in the thermo-mechanical flow of ice-sheets. *J. Geophys. Res.* **102** (B6), 12,219–12,233.

PEGLER, S. S., KOWAL, K. N., HASENCLEVER, L. Q. & WORSTER, M. G. 2013 Lateral controls on grounding line dynamics. *J. Fluid Mech.* **722**.

PEGLER, S. S. & WORSTER, M. G. 2012 Dynamics of a viscous layer flowing radially over an inviscid ocean. *J. Fluid Mech.* **696**, 152–174.

PERKINS, T. K., JOHNSTON, O. C. & HOFFMAN, R. N. 1965 Mechanics of viscous fingering in miscible systems. *Soc. Pet. Eng. J.* **5** (04), 301–317.

PIHLER-PUZOVIC, D., ILLIEN, P., HEIL, M. & JUEL, A. 2012 Suppression of complex fingerlike patterns at the interface between air and a viscous fluid by elastic membranes. *Phys. Rev. Lett.* **108**, 074502.

PIHLER-PUZOVIC, D., PERILLAT, R., RUSSELL, M., JUEL, A. & HEIL, M. 2013 Modelling the suppression of viscous fingering in elastic-walled Hele-Shaw cells. *J. Fluids Mech.* **731**, 161.

PITTARD, JOANNE D. 2017 Safety Monitors in Hemodialysis. In *Handbook of Dialysis Therapy: Fifth Edition*, 2nd edn., chap. 3, pp. 162–190. Elsevier.

REYNOLDS, OSBORNE 1886 On the Theory of Lubrication and Its Application to Mr. Beauchamp Tower's Experiments, Including an Experimental Determination of the Viscosity of Olive Oil. *Philosophical Transactions of the Royal Society of London Series I* **177**, 157–234.

ROBISON, R. A. V., HUPPERT, H. E. & WORSTER, M. G. 2010 Dynamics of viscous grounding lines. *J. Fluid Mech.* **648**, 363–380.

SAFFMAN, P. G. & TAYLOR, G. 1958 The penetration of a fluid into a porous medium or Hele-Shaw cell containing a more viscous liquid. *Proc. R. Soc. Lond. A* **245**, 312–329.

SAKAI, K. 2000 Dialysis membranes for blood purification. *Front. Bioeng.* **10** (2), 117–129.

SAMES, W. J., LIST, F. A., PANNALA, S., DEHOFF, R. R. & BABU, S. S. 2016 The metallurgy and processing science of metal additive manufacturing. *International Materials Reviews* **61** (5), 315–360, arXiv: http://dx.doi.org/10.1080/09506608.2015.1116649.

SARGENT, JA & GOTCH, FA 1996 Principles and biophysics of dialysis. In *Replacement of Renal Function by Dialysis*, 4th edn. (ed. C. Jacobs, C. M. Kjellstrand, K. M. Koch & J. F. Winchester), pp. 34–102. Dordrecht: Kluwer Academic Publishers.

SAYAG, R. & TZIPERMAN, E. 2008 Spontaneous generation of pure ice streams via flow instability: Role of longitudinal shear stresses and subglacial till. *J. Geophys. Res.* **113** (B05411).

SAYAG, R. & TZIPERMAN, E. 2009 Spatiotemporal dynamics of ice streams due to a triple-valued sliding law. *J. Fluid Mech.* **640**, 483–505.

SCHOOF, C. & HEWITT, I. J. 2013 Ice-sheet dynamics. *Annu. Rev. Fluid Mech.* **45**, 217–239.

SHAH, KASTURI S., PEGLER, SAMUEL S. & MINCHEW, BRENT M. 2021 Two-layer fluid flows on inclined surfaces. *J. Fluid Mech.* **917**, A54.

SIMPSON, J. E. 1982 Gravity currents in the laboratory, atmosphere, and ocean. *Ann. Rev. Fluid Mech.* **14**, 213–234.

SMITH, S. H. 1969 On initial value problems for the flow in a thin sheet of viscous liquid. *Journal of Applied Mathematics and Physics (ZAMP)* **20** (4), 556–560.

SNYDER, DON & TAIT, STEPHEN 1995 Replenishment of magma chambers: comparison of fluid-mechanic experiments with field relations. *Contrib. to Mineral. Petrol.* **122** (3), 230–240.

SNYDER, D. & TAIT, S. 1998 A flow-front instability in viscous gravity currents. *J. Fluid Mech.* **369**, 1–21.

TAKAGI, DAISUKE & HUPPERT, HERBERT E. 2010 Flow and instability of thin films on a cylinder and sphere. *J. Fluid Mech.* **647**, 221–238.

TAYLOR, G. I. 1963 Cavitation of a viscous fluid in narrow passages. *J. Fluid Mech.* **16**, 595–619.

TAYLOR-WEST, J. J., BALMFORTH, N. J. & HOGG, A. J. 2024 Lava delta formation: mathematical modelling and laboratory experiments. *J. Geoph. Res. Solid Earth* .

THOMPSON, S. & ET AL. 2015 Alberta kidney disease network. cause of death in patients with reduced kidney function. *J Am Soc Nephrol* **26** (10), 2504–11.

TONELLI, M & ET AL. 2010 Systematic review: Kidney transplantation compared with dialysis in clinically relevant outcomes. *American Journal of Transplantation* **11** (10), 2093 – 2109.

TROIAN, S. M., HERBOLZHEIMER, E., SAFRAN, S. A. & JOANN, J. F. 1989 Fingering instabilities of driven spreading films. *Europhys. Lett.* **10** (1), 25–30.

VAQUERO-STAINER, C., HEIL, M., JUEL, A. & PIHLER-PUZOVIĆ, D. 2019 Self-similar and disordered front propagation in a radial hele-shaw channel with time-varying cell depth. *Phys. Rev. Fluids* **4**, 064002.

VILLARROEL, F, KLEIN, E & HOLLAND, F. 1977 Solute flux in hemodialysis and hemofiltration membranes. *Trans Am Soc Artif Intern Organs* **23**, 225–233.

WANIEWSKI, JACEK 2006 Mathematical modeling of fluid and solute transport in hemodialysis and peritoneal dialysis. *Journal of Membrane Science* **274** (1-2), 24–37.

WANIEWSKI, JACEK, LUCJANEK, PIOTR & WERYRISKI, ANDRZEJ 1994 Impact of ultrafiltration on back-diffusion in hemodialyzer. *Artificial organs* **18** (12), 933–941.

WANIEWSKI, J., WERYNSKI, A., AHRENHOLZ, P., LUCJANEK, P., JUDYCKI, W. & ESTHER, G. 1991 Theoretical basis and experimental verification of the impact of ultrafiltration on dialyzer clearance. *Artificial Organs* **15** (2), 70–77.

WOODS, A. W. & MASON, R. 2000 The dynamics of two-layer gravity-driven flows in permeable rock. *J. Fluid Mech.* **421**, 83–114.

XIAO, ZHIYONG & KOMATSU, GORO 2013 Impact craters with ejecta flows and central pits on Mercury. *Planetary and Space Science* **82-83**, 62–78.

YAN, Z & KOWAL, K N 2024 A controllable sliding law for thin-film flows over slippery fluid-saturated substrates: theory and experiments. *J. Fluid Mech.* **982**, A14.

YANG, H. & KOWAL, K. N. 2025 Non-porous viscous fingering of a thin film of fluid spreading over a lubricated substrate. *J. Fluid Mech.* **1013**, A32.

YANG, H, MOTTRAM, N J & KOWAL, K N 2024 Dynamics of a thin film of fluid spreading over a lubricated substrate. *J. Fluid Mech.* **1001**, A47.

YIH, C. S. 1967 Instability due to viscosity stratification. *J. Fluid Mech.* **27**, 337–352.

YING, CHAO, SHI, CHENGWU, WU, NI, ZHANG, JINCHENG & WANG, MAO 2015 A two-layer structured PbI2 thin film for efficient planar perovskite solar cells. *Nanoscale* **7** (28), 12092–12095.

ZHENG, ZHONG, KIM, HYOUNGSOO & STONE, HOWARD A. 2015 Controlling viscous fingering using time-dependent strategies. *Phys. Rev. Lett.* **115**, 174501.